sid.inpe.br/mtc-m19/2012/11.22.12.22 -TDI

DEPLOYMENT AND MAINTENANCE OF A SATELLITE FORMATION FLIGHT AROUND L4 AND L5 LAGRANGIAN POINTS IN THE EARTH-MOON SYSTEM BASED ON LOW COST STRATEGIES

Francisco Javier Tipan Salazar

Doctorate Thesis at Post Graduation Couse in Applied Computing, advised by Drs. Elbert Einstein Macau, and Othon Cabo Winter, approved in December 04, 2012.

URL of the original document:
<http://urlib.net/8JMKD3MGP7W/3D43GKS>

INPE
São José dos Campos
2012

PUBLISHED BY:

Instituto Nacional de Pesquisas Espaciais - INPE
Gabinete do Diretor (GB)
Serviço de Informação e Documentação (SID)
Caixa Postal 515 - CEP 12.245-970
São José dos Campos - SP - Brasil
Tel.:(012) 3208-6923/6921
Fax: (012) 3208-6919
E-mail: pubtc@sid.inpe.br

BOARD OF PUBLISHING AND PRESERVATION OF INPE INTELLECTUAL PRODUCTION (RE/DIR-204):
Chairperson:
Marciana Leite Ribeiro - Serviço de Informação e Documentação (SID)
Members:
Dr. Antonio Fernando Bertachini de Almeida Prado - Coordenação Engenharia e Tecnologia Espacial (ETE)
Dr^{a} Inez Staciarini Batista - Coordenação Ciências Espaciais e Atmosféricas (CEA)
Dr. Gerald Jean Francis Banon - Coordenação Observação da Terra (OBT)
Dr. Germano de Souza Kienbaum - Centro de Tecnologias Especiais (CTE)
Dr. Manoel Alonso Gan - Centro de Previsão de Tempo e Estudos Climáticos (CPT)
Dr^{a} Maria do Carmo de Andrade Nono - Conselho de Pós-Graduação
Dr. Plínio Carlos Alvalá - Centro de Ciência do Sistema Terrestre (CST)

DIGITAL LIBRARY:
Dr. Gerald Jean Francis Banon - Coordenação de Observação da Terra (OBT)
DOCUMENT REVIEW:
Marciana Leite Ribeiro - Serviço de Informação e Documentação (SID)
Yolanda Ribeiro da Silva Souza - Serviço de Informação e Documentação (SID)
ELECTRONIC EDITING:
Maria Tereza Smith de Brito - Serviço de Informação e Documentação (SID)

sid.inpe.br/mtc-m19/2012/11.22.12.22 -TDI

DEPLOYMENT AND MAINTENANCE OF A SATELLITE FORMATION FLIGHT AROUND L4 AND L5 LAGRANGIAN POINTS IN THE EARTH-MOON SYSTEM BASED ON LOW COST STRATEGIES

Francisco Javier Tipan Salazar

Doctorate Thesis at Post Graduation Couse in Applied Computing, advised by Drs. Elbert Einstein Macau, and Othon Cabo Winter, approved in December 04, 2012.

URL of the original document:
<http://urlib.net/8JMKD3MGP7W/3D43GKS>

INPE
São José dos Campos
2012

Cataloging in Publication Data

Sa31d

Salazar, Francisco Javier Tipan.

Deployment and maintenance of a satellite formation flight around l4 and l5 Lagrangian points in the earth-moon system based on low cost strategies / Francisco Javier Tipan Salazar. – São José dos Campos : INPE, 2012.

xxviii + 141 p. ; (sid.inpe.br/mtc-m19/2012/11.22.12.22 -TDI)

Thesis (Doctorade in Applied Computing) – Instituto Nacional de Pesquisas Espaciais, São José dos Campos, 2012.

Advisers : Drs. Elbert Einstein Macau, e Othon Cabo Winter.

1. three bodies. 2. lagrangian points. 3. low cost. 4. formation fligth. I.Título.

CDU 004:521.135

Copyright © 2012 do MCT/INPE. Nenhuma parte desta publicação pode ser reproduzida, armazenada em um sistema de recuperação, ou transmitida sob qualquer forma ou por qualquer meio, eletrônico, mecânico, fotográfico, reprográfico, de microfilmagem ou outros, sem a permissão escrita do INPE, com exceção de qualquer material fornecido especificamente com o propósito de ser entrado e executado num sistema computacional, para o uso exclusivo do leitor da obra.

Copyright © 2012 by MCT/INPE. No part of this publication may be reproduced, stored in a retrieval system, or transmitted in any form or by any means, electronic, mechanical, photocopying, recording, microfilming, or otherwise, without written permission from INPE, with the exception of any material supplied specifically for the purpose of being entered and executed on a computer system, for exclusive use of the reader of the work.

Aprovado (a) pela Banca Examinadora em cumprimento ao requisito exigido para obtenção do Título de *Doutor(a)* em

Computação Aplicada

Dr. Solon Venâncio de Carvalho

Presidente / INPE / SJCampos - SP

Dr. Elbert Einstein Nehrer Macau

Orientador(a) / INPE / São José dos Campos - SP

Dr. Othon Cabo Winter

Othon Cabo Winter

Orientador(a) / UNESP/GUARA / Guaratinguetá - SP

Dr. Joaquim José Barroso de Castro

J.J. Barroso

Membro da Banca / INPE / SJCampos - SP

Dr. Rodolpho Vilhena de Moraes

Convidado(a) / UNIFESP / São José dos Campos - SP

Dr. Ernesto Vieira Neto

Convidado(a) / UNESP/GUARA / Guaratinguetá - SP

Dr. Pablo Miguel Cincotta

Convidado(a) / CONICET / La Plata - AR

Este trabalho foi aprovado por:

( ) maioria simples

(X) ***unanimidade***

Aluno (a): ***Francisco Javier Tipan Salazar***

São José dos Campos, 04 de Dezembro de 2012

“Thousands of years ago the first man discovered how to make fire. He was probably burned at the stake he had taught his brothers to light, but he left them a gift they had not conceived of, and he lifted darkness off the earth”.

Ayn Rand
in *“The Fountainhead”*, 1949

In memory of my mother Rosa Mercedes Salazar

ACKNOWLEDGEMENTS

First of all, I'd like to thank to my advisors Dr. Elbert Einstein Nehrer Macau and Dr. Othon Cabo Winter, who gave me motivation, inspiration and encouragement during my graduate program. They also introduced me to many new topics and new ideas for research in Orbital Dynamics. They gave me a big share of their time at the National Institute for Space Research - INPE or at the São Paulo State University - UNESP. Thanks also go to the other members of my graduate committee, Dr. Solon Venâncio de Carvalho, Dr. Joaquim Barroso de Castro, Dr. Rodolpho Vilhena de Moraes, Dr. Ernesto Vieira Neto and Dr. Pablo Miguel Cincotta for their corrections and comments to this thesis.

Thanks also go to Prof. Josep Masdemont and Prof. Gerard Gómez of the Polytechnic University of Catalonia - Spain, who supervised my international research stage in Barcelona and contributed greatly in the success of this work. Their ideas, generosity and suggestions not only let me to write the last chapter of this thesis but they played a key role in the quality of this dissertation. I owe a great debt of gratitude to them.

I'd also like to thank to the National Institute for Space Research - INPE and to the Fundação de Amparo à Pesquisa do Estado de São Paulo - FAPESP, for the financial investment of sponsoring my four years of Ph.D. in São Paulo and Barcelona.

I also want to mention here friends at the National Institute for Space Research - INPE who had a positive influence on my project. In alphabetical order, I want to make a special thanks to Aline Soterroni, Caroline da Silva, Érica de Souza, Helaine Furtado, Laurita do Santos, Noemi Araújo, Renata Rocha, Rita Ricarte, Rodolfo Almeida, Rosângela Follman, Valentin Bageston and Wantuir de Freitas for their invaluable friendship and help during those four years. They have, in their own individual ways, left an indelible mark on my life.

Thanks also go to my colleagues and former professors at the National Institute for Space Research - INPE for introducing me to the field of astrodynamics and giving me encouragement to finish my Ph.D. In particular, Dr. Antonio Bertachini de Almeida Prado and Dr. Marcelo Lopes Oliveira e Souza.

Finally, I'd like to thank my parents José and Mercedes, my brother José and my sisters María and Gabriela for their love, support and unwavering belief in me, even when there have been many reasons not to believe. My ability to complete this work

owes much to them.

IMPLEMENTAÇÃO E MANUTENÇÃO DE SATÉLITES EM VOO DE FORMAÇÃO AO REDOR DOS PONTOS LAGRANGIANOS L4 E L5 COM BASE EM ESTRATÉGIAS DE BAIXO EMPUXO

RESUMO

Este trabalho está focado em métodos de transferência a partir de uma órbita circular ao redor da Terra até órbitas periódicas ao redor dos pontos Lagrangianos L_4 e L_5 no sistema Terra - Lua, com aplicações para colocar vários satélites em vôo de formação. Os pontos Lagrangianos L_4 e L_5 estão localizados a 60 graus acima e embaixo da linha que conecta a Terra com a Lua e formam com estes dois corpos um triângulo equilátero. Estes pontos Lagrangianos são estáveis pela relação de massa entre a Terra e a Lua. Devido à sua distância, radiações eletromagnéticas que proveem da Terra e chegam até eles são substancialmente atenuadas. Dessa maneira, estes pontos Lagrangianos representam posições extraordinárias para colocar observatórios astronômicos. Inspirados nos recentes resultados em manobras assistidas por gravidade, os métodos de transferência implementados neste trabalho usam o campo gravitacional da Lua para atingir os pontos Lagrangianos. Nós aplicamos três diferentes técnicas para intersectar a esfera de influência da Lua: Transferências de Mínima Energia, Trajetórias G e Órbitas Caóticas, e mostramos que existem novas trajetórias alternativas para chegar até nosso objetivo. Nós encontramos vantagens em relação à Transferência de Hohmann tais como gasto menor de combustível e a possibilidade de usar o mesmo lançador para enviar os satélites até os pontos L_4 e L_5. O trabalho também apresenta um estudo das geometrias ao redor das órbitas periódicas centradas em L_4 com boas propriedades para vôos em formação. Nós consideramos a possibilidade da existência de regiões com aceleração radial relativa zero com respeito à trajetória nominal. As simulações numéricas mostram que para evitar grandes variações das distâncias mutuas entre os satélites, a formação tem que estar localizada não ao longo da direção de aceleração radial relativa nula senão ao longo da direção de aceleração radial relativa mínima. Este trabalho está feito utilizando o modelo Circular Restrito de Três Corpos, considerando só o movimento no plano da órbita dos sistema Terra-Lua.

ABSTRACT

This thesis focuses on transfer methods from a circular parking orbit around the Earth to periodic orbits around the Lagrangian points L_4 and L_5 in the Earth-Moon system, with applications to place multiple satellites in formation flying. Lagrangian points L_4 and L_5 lie at 60 degrees ahead of and behind Moon in its orbit with respect to the Earth and form an equilateral triangle with the base of the line defined by those two bodies. These Lagrangian points are stable for the Earth-Moon mass ratio. Because of their distance, electromagnetic radiations from the Earth arrive on them substantially attenuated. As so, these Lagrangian points represent remarkable positions to host astronomical observatories. Inspired by the recent results in gravity assist maneuvers, the transfer methods implemented in this work use the gravitational field of the Moon to reach the Lagrangian points. We apply three different techniques to intersect the lunar sphere of influence: Minimum Energy Transfers, Trajectories G and Chaotic Orbits, and prove that there exist new alternative trajectories to reach our target. We find advantages over the Hohmann transfer such as less fuel spent and the possibility using only one rocket launcher to deliver spacecrafts to L_4 and L_5. The thesis also presents a study of geometries around periodic orbits centered at L_4 with good properties for formation flying. We consider the possible existence of regions of zero relative radial acceleration with respect to the nominal trajectory. Numerical simulations show that to avoid large variations of the mutual distances between the spacecrafts, the formation flying must be arranged not along the direction of zero relative radial acceleration but along the direction of minimum relative radial acceleration. This work is done in the force model defined by the Circular Restricted Three Body Problem, considering only the motion on the plane of the orbit of the Earth-Moon system.

LIST OF FIGURES

Pág.

1.1 Illustration of Satellite Formation Flying.
From: (JET PROPULSION LABORATORY, 2012). 1
1.2 Illustration of LISA spacecraft.
From: (NASA, 2012) 2
1.3 Illustration of satellites Landsat 7 with EO-1 in formation flying.
From: (NASA, 2011) 3
1.4 Illustration of a mission around Lagrangian point L_4 in the Earth-Moon system.
From: (WIKIPEDIA, 2012) 4
1.5 Illustration of missions around Lagrangian points L_1 and L_2 in the Sun-Earth system.
From (MATHEMATICAL ASSOCIATION OF AMERICA, 2004) 5
1.6 Lagrange equilibrium points geometry for the Earth-Moon system in the synodic frame.
From: (ARAÚJO, 2011) 6
1.7 Illustration of a Hohmann Transfer Orbit. 8
1.8 Illustration of a swing-by maneuver with the Moon guiding a spacecraft to L_4. 9
1.9 Illustration of the sphere of influence concept in the Earth-Moon system. 10
1.10 Lagrangian equilibrium points and a typical orbit of the G Family in the synodic frame. (From: (MELO et al., 2007) 12
1.11 Chaotic Trajectory in the Earth-Moon system in the synodic frame. . . . 13
1.12 Illustration of the controlled chaotic trajectory reaching Lagrange equilibrium point L_4 for the Earth-Moon system. 14
1.13 Illustration of a leader-follower type of a two-spacecraft formation. 15
1.14 Illustration of a general type of spacecraft formation where the chief satellite is placed in a periodic orbit around L_4. 15
1.15 Illustration of three cases of variations of the mutual distance between the spacecrafts in a formation flying. 16

2.1 Illustration of Circular Restricted Three Body Problem: Earth-Moon-particle. 20
2.2 Zero-velocity curves for the Earth-Moon system. The values of C are (a) $C = 3.50$ and (b) $C = 3.18$. The shaded areas denote the exclude regions. 25

2.3 Critical Zero-Velocity curves about Earth and Moon touching the Lagrangian equilibrium points. . . . 26
2.4 Long and Short Period Orbits about L_4 for the Earth and the Moon system. The principal axes of the elliptic trajectories are oriented according to the angle α 30
2.5 Illustration of a satellite formation flying about L_4. The vectors $X_h(t)$ and $X(t)$ are the corresponding trajectories of the chief and deputy satellites, respectively. Vector $\Delta X(t)$ represents the relative position and velocity of the deputy satellite with respect to the chief satellite at instant t. 32
2.6 Orbit $\phi(t, X_0)$ passes through X_0 at time $t = 0$ and intersects the x-axis at the point X_f at time $t = T$. Periodic solution $\phi(t, X^*)$ satisfies the condition $\phi(t, X^*) = X^*$. 33

3.1 Illustration of the spacecraft's trajectory intersecting the perpendicular axes x'', y''. 36
3.2 Illustration of the stabilizing impulsive thrust applied to enter the elliptic orbit around L_4 when the spacecraft intersects (a) the semi-major axis and (b) the semi-minor axis. 37
3.3 Illustration of the minimum energy transfer orbit to periodic orbits around (a) L_4 and (b) L_5. 39
3.4 Illustration of the sphere of influence concept in the Earth-Moon system. The radius R_S of the lunar sphere of influence is about 1/6 the distance from Earth to the Moon. 42
3.5 Illustration of the geocentric departure orbit. 43
3.6 Illustration of the selenocentric arrival orbit. 44
3.7 The Swing-by Maneuver with the Moon. 46
3.8 Velocity vectors involved in a swing-by maneuver with the Moon. 48
3.9 Vector diagram describing the vectorial sum $\boldsymbol{v_1} = \boldsymbol{v_2} + \boldsymbol{v_M}$. 49
3.10 Geometric relation between angles δ, β, and ψ. 50
3.11 Illustration of a minimum energy transfer orbit of semi-major axis of $a_m = (r_0 + d)/2$ to cross the lunar sphere of influence. 51
3.12 The spacecraft and Moon move through an angle f_1 and $\omega_M \Delta t$, respectively, between injection and arrival at the lunar sphere of influence. 52
3.13 Lagrangian equilibrium points and typical orbits of the G Family in the synodic coordinate system: (a) $(x_0, 0, \dot{x}_0, \dot{y}_0) = (0.741686, 0, 0, 0.53176)$, (a) $(x_0, 0, \dot{x}_0, \dot{y}_0) = (0.299999, 0, 0, 0.195941)$ and (c) (a) $(x_0, 0, \dot{x}_0, \dot{y}_0) = (0.399997, 0, 0, -2.271238)$.
From: (MELO et al., 2007) 54

3.14 Illustration of the quantities involved in the insertion of a spacecraft into a periodic orbit of G Family. Orbit seen in the synodic frame (not to scale). 55
3.15 Swing-by orbits: (a) Passing by the Moon's trailing side to reach L_4 ($180^\circ < \Phi \leq 360^\circ$) (b) Passing by the Moon's leading side to reach L_5 ($0^\circ < \Phi \leq 180^\circ$). 57
3.16 Spiral trajectory to transfer a spacecraft between two circular Earth orbits of radius r_0 and r_f using a constant tangential thrust. 60
3.17 Trajectory of the spacecraft in the chaotic region for the Earth-Moon system (time of flight: 25 years). 61
3.18 (a) Poincaré section of the CRTBP at $C = 3.17948$ for the Earth-Moon system, (b) Chaotic region in the middle of periodic orbits represented by robust islands. 62
3.19 Poincaré section with negative $\dot{y}$ of the chaotic trajectory of the spacecraft shown in Fig. 3.17. 63
3.20 Poincaré recurrences: the orbit returns to set $\mathcal{A}$ many times. 63
3.21 Algorithm to find efficiently recurrences. 64
3.22 Illustration of a recurrent loop between iterates i and $i + s$. Stable W^s and unstable W^u manifolds intersect each other at a point p. 65
3.23 Iterates i and $i + s$ intersect each other at a point p such that the pre-orbit and orbit of p approach the pre-orbit and orbit of iterate i and $i+s$, respectively. 66
3.24 A small perturbation Δu_1 is made in the pre-orbit of iterate i such that the new orbit approaches the orbit of iterate $i + s$ and finally a second small perturbation Δu_2 must be made to get back to the original orbit. . 67
3.25 Swing-by maneuver to reach Lagrange equilibrium points L_4 or L_5 for the Earth-Moon system. 68

4.1 Chief and deputy satellites in a formation in a periodic orbit around L_4. 72
4.2 Illustration of Zero relative radial acceleration lines along a periodic solution 73
4.3 Illustration of a sphere of radius s for each point of the periodic solution $X_h(t)$ 73
4.4 Illustration of the dot product between the relative position and relative acceleration vectors for each point of the periodic solution $X_h(t)$. The angle $\theta^*(t)$ defines the direction of the relative position vector $\boldsymbol{r}(t)$ that belongs to ZRRAL at time t. 74
4.5 Illustration of a spacecraft following an artificial trajectory $\boldsymbol{r_a}(t)$ along a periodic trajectory $X_h(t)$ around L_4. 75

5.1 Elliptic Orbits centered at L_4 of (a) 92 and (b) 28 days period. These two orbits have been chosen to implement the transfer orbits methods described in Chapter 3. 78
5.2 Hohmann transfer orbit to reach the long (first column) and short (second column) period orbits in the synodic system. 81
5.3 Trajectories corresponding to Fig. 5.2 intersecting the semi-minor axis of the elliptic orbits. At that moment it is applied the stabilizing impulsive thrust to place the spacecraft around the equilibrium points. 82
5.4 Trajectories corresponding to Fig. 5.2 in the Earth-centered inertial system $\hat{\boldsymbol{n}}_1, \hat{\boldsymbol{n}}_2$. 83
5.5 Swing-By maneuver to reach the long period orbit around L_4 in the synodic system. The apocentre of the geocentric departure orbit and the angle at which it intersects the lunar sphere of influence are: (a) $d = d_{EM} - R_S/2$, $\lambda_0 = 10.8°$, (b) $d = d_{EM} - R_S/2$, $\lambda_0 = 40.6°$, (c) $d = d_{EM}$, $\lambda_0 = 30.4°$, (d) $d = d_{EM} + R_S/2$, $\lambda_0 = 10.5°$, and (e) $d = d_{EM} + R_S/2$, $\lambda_0 = 16.0°$. 91
5.6 Swing-By maneuver to reach the long period orbit around L_5 in the synodic system. The apocentre of the geocentric departure orbit and the angle at which it intersects the lunar sphere of influence are: (a) $d = d_{EM}$, $\lambda_0 = 7.7°$, (b) $d = d_{EM}$, $\lambda_0 = 27.4°$, (c) $d = d_{EM}$, $\lambda_0 = 45.7°$, (d) $d = d_{EM} + R_S/2$, $\lambda_0 = 9.8°$. 92
5.7 Trajectories corresponding to Fig. 5.5 intersecting the semi-minor axis of the elliptic orbit. At that moment it is applied the stabilizing impulsive thrust to place the spacecraft around the equilibrium points. 93
5.8 Trajectories corresponding to Fig. 5.6 intersecting the semi-minor axis of the elliptic orbit. At that moment it is applied the stabilizing impulsive thrust to place the spacecraft around the equilibrium points. 94
5.9 Trajectories corresponding to Fig. 5.5 in the Earth-centered inertial system $\hat{\boldsymbol{n}}_1, \hat{\boldsymbol{n}}_2$. 95
5.10 Trajectories corresponding to Fig. 5.6 in the Earth-centered inertial system $\hat{\boldsymbol{n}}_1, \hat{\boldsymbol{n}}_2$. 96
5.11 Spacecrafts' transfer trajectories, energy variations relative to the Earth as a function of the time and velocities in the geocentric and synodic coordinates systems also as a function of the time for L_4 mission (left column) and for L_5 mission (right column). 97
5.12 Trajectories corresponding to Fig. 5.11 intersecting the semi-major axis of the elliptic orbit. At that moment it is applied the stabilizing impulsive thrust to place the spacecraft around (a) L_4 and (b) L_5. 98

5.13 The same initial path of the previously G-trajectory (that appears here in geocentric reference coordinate system) can be used to place a spacecraft into periodic orbits around L_4 or L_5. As so, if an appropriate low thrust is applied in the apogee of this G-trajectory, the spacecraft ends up of in L_4 or in L_5. Both situations are depicted here. Observe in the last row of Fig. 5.11, also in geocentric system, the large difference between the spacecrafts' velocities after the swing-by. 99
5.14 (a) Chaotic trajectory and (b) Controlled chaotic trajectory to the Moon starting from a circular parking orbit $59,669$ km above the Earth's center (time required for transfer: 311 days). 101
5.15 Final trajectory arriving at Lagrangian points L_4 (left column) and L_5 (right column). The time required for L_4 and L_5 transfer is 342 and 370 days, respectively. 102
5.16 Discriminant of the sub-matrix F associated to the points $X_h(t)$ along the (a) long and (b) short period orbits shown in Fig. 5.1 104
5.17 Scalar product between the relative acceleration $\boldsymbol{a}\,(t,\theta)$ and vector $\boldsymbol{s}\,(\theta)$ as a function of angle θ at three different points $X_h\,(t)$ along the long (first row) and short (second row) period orbits shown in Fig. 5.1 104
5.18 Scalar product between the relative acceleration $\boldsymbol{a}\,(t,\theta)$ and vector $\boldsymbol{s}\,(\theta)$ as a function of angle θ at three different points $X_h\,(t)$ along the long (first row) and short (second row) period orbits shown in Fig. 5.1 105
5.19 Angle θ for each point $X_h\,(t)$ where the relative radial acceleration has a maximum and minimum value along the long (first row) and short (second row) period orbits shown in Fig. 5.1 106
5.20 (a) Long and (b) short period orbits around L_4. 107
5.21 Discriminant of the sub-matrix F associated to the points along the (a) long and (b) short period orbits shown in Fig. 5.20 107
5.22 Scalar product between the relative acceleration $\mathbf{a}\,(t,\theta)$ and vector $\mathbf{s}\,(\theta)$ as a function of angle θ at three different points $X_h\,(t)$ along the long (first row) and short (second row) period orbits shown in Fig. 5.20 108
5.23 Angle θ for each point $X_h\,(t)$ where the relative radial acceleration has a maximum value for the (a) long and (b) short period orbits shown in Fig. 5.20 108
5.24 Angle θ for each point $X_h\,(t)$ where the relative radial acceleration has a minimum or zero value for the long (first row) and short (second row) period orbits shown in Fig. 5.20 109
5.25 (a) Long and (b) short period families around L_4. 110

5.26 Discriminant of the sub-matrix F associated to the points along the (a) long and (b) short period families shown in Fig. 5.25 111
5.27 Angle θ for each point $X_h(t)$ where the relative radial acceleration has a maximum value for the (a) long and (b) short period families shown in Fig. 5.25 111
5.28 Angle θ for each point $X_h(t)$ where the relative radial acceleration has a minimum or zero value for the long (first row) and short (second row) period families shown in Fig. 5.25 112
5.29 Components x (right column) and y (left column) of relative position $\boldsymbol{r_a}$ (first row), relative velocity $\dot{\boldsymbol{r}}_{\boldsymbol{a}}$ (second row) and relative acceleration $\ddot{\boldsymbol{r}}_{\boldsymbol{a}}$ (third row) of the artificial trajectory that follows the direction such that the relative radial acceleration component is minimum with respect to the long period orbit shown in Fig. 5.20 113
5.30 Components x (right column) and y (left column) of relative position $\boldsymbol{r_a}$ (first row), relative velocity $\dot{\boldsymbol{r}}_{\boldsymbol{a}}$ (second row) and relative acceleration $\ddot{\boldsymbol{r}}_{\boldsymbol{a}}$ (third row) of the artificial trajectory that follows the direction such that the relative radial acceleration component is minimum or zero with respect to the long period orbit shown in Fig. 5.20 114
5.31 Radial Acceleration of the artificial trajectory that follows the direction such that the relative radial acceleration component is minimum or zero with respect to the long period orbit shown in Fig. 5.20 115
5.32 Family of periodic orbits shown in Fig. 5.25, where Orbit 1 denotes the smallest one and Orbit 8 denotes the largest one 115
5.33 Cost of maintaining a spacecraft during 1 year with respect to the long (a) and short (b) period family shown in Fig. 5.25 fixing the angle θ and considering a radius of 1 km 118
5.34 Formation flying of three satellites such that their positions and distances with respect to periodic orbit are fixed and form an equilateral triangle . 118
5.35 Cost of maintaining during 1 year a Formation flying of three satellites considering configurations (a), (b) and (c) around the long and short period orbits shown in Fig. 5.1 119
5.36 Cost of maintaining during 1 year a Formation flying of three satellites considering configurations (a), (b) and (c) around the long and short period orbits shown in Fig. 5.20 120
5.37 Illustration of the relative position of a spacecraft around a periodic orbit of L_4 121

5.38 Maximum separation (in km) during 2 years for different values of $r\left(0\right)$ and $\theta\left(0\right)$ computed in nine points $X_h\left(0\right)$ along the long period orbit shown in Figure 5.1 122
5.39 Maximum separation (in km) during 2 years for different values of $r\left(0\right)$ and $\theta\left(0\right)$ computed in nine points $X_h\left(0\right)$ along the short period orbit shown in Figure 5.1 123
5.40 Maximum separation (in km) during 2 years for $0° \leq \theta\left(0\right) \leq 360°$ and $r\left(0\right) = 1, 2$ km along the long period orbit shown in Fig. 5.1 124
5.41 Maximum separation (in km) during 2 years for $0° \leq \theta\left(0\right) \leq 360°$ and $r\left(0\right) = 1, 2$ km along the short period orbit shown in Fig. 5.1 124
5.42 Distance function $d\left(X_h\left(t\right), X_i\left(t\right)\right)$, between the trajectories of $\boldsymbol{r_1}$, $\boldsymbol{r_2}$, $\boldsymbol{r_3}$, $\boldsymbol{r_4}$ (first row), and $\boldsymbol{q_1}$, $\boldsymbol{q_2}$, $\boldsymbol{q_3}$, $\boldsymbol{q_4}$ (second row), and the long and short period orbits shown in Figure 5.1 125
5.43 Maximum separation (in km) during two years for $0° \leq \theta\left(0\right) \leq 360°$ and $r\left(0\right) = 1, 2$ km along the long period orbit shown in Figure 5.20 125
5.44 Maximum separation (in km) during two years for $0° \leq \theta\left(0\right) \leq 360°$ and $r\left(0\right) = 1, 2$ km along the short period orbit shown in Figure 5.20 126
5.45 Distance function $d\left(X_h\left(t\right), X_i\left(t\right)\right)$, between the trajectories of $\boldsymbol{r_1}$, $\boldsymbol{r_2}$, $\boldsymbol{r_3}$, $\boldsymbol{r_4}$ (first row), and $\boldsymbol{q_1}$, $\boldsymbol{q_2}$, $\boldsymbol{q_3}$, $\boldsymbol{q_4}$ (second row), and the long and short period orbits shown in Figure 5.20 126
5.46 Difference between the angles θ_1 and θ_2 for trajectories starting at 1 km and 2 km from $X_h\left(0\right)$ 127
5.47 Difference between the angles θ_1 and θ_2 at each instant t starting at 1 km and 2 km from $X_h\left(0\right)$ associated to the initial conditions of the long (a) and short (b) period orbits shown in Fig. 5.1 127
5.48 Difference between the angles θ_1 and θ_2 at each instant t starting at 1 km and 2 km from $X_h\left(0\right)$ associated to the initial conditions of the long (a) and short (b) period orbits shown in Fig. 5.20 128
5.49 Illustration of a constellation of satellites remaining aligned along the periodic orbits around L_4 128

LIST OF TABLES

Pág.

2.1 Coordinates of the Lagrangian Equilibrium points on the Earth-Moon plane . . . 24
2.2 Critical values of C and the corresponding Lagrangian points that are reachable in the Earth-Moon system . . . 26

3.1 Performance expected for PMHT to be used in the ASTER spacecraft From: (MACAU et al., 2011) . . . 59

5.1 Lengths a and b of the semi-major and minor axes, respectively, and coordinates in the system x'', y'' of the velocity vectors $\boldsymbol{v_a}$ and $\boldsymbol{v_b}$ at points $(a, 0)$ and $(0, b)$ of the elliptic orbits shown in Fig. 5.1 . . . 78
5.2 Apocentre d, phase angle at departure γ_0, change in velocity Δv_1, stabilizing impulsive thrust Δv_2, total cost Δv_T and time of flight Δt for placing a spacecraft into the long and short period orbits around L_4 . . . 79
5.3 Apocentre d, phase angle at departure γ_0, change in velocity Δv_1, stabilizing impulsive thrust Δv_2, total cost Δv_T and time of flight Δt for placing a spacecraft into the long and short period orbits around L_5 . . . 80
5.4 Initial position and velocity coordinates for placing a spacecraft into the long and short period orbits around L_4 (referred to the non-dimensional rotating frame system) corresponding to departure geometries described in Table 5.2 . . . 80
5.5 Initial position and velocity coordinates for placing a spacecraft into the long and short period orbits around L_5 (referred to the non-dimensional rotating frame system) corresponding to departure geometries described in Table 5.3 . . . 80
5.6 Values of the apocentre d and interval for λ_0 that contains the trajectories that intersect either the long or short period orbits shown in Fig. 5.1 . . . 84
5.7 Apocentre d, angle λ_0, phase angle at departure γ_0, parameters that described the geometry of the swing-by, and change in velocity and energy experimented by the spacecraft after the swing-by maneuver is completed, of each trajectory for placing a spacecraft into the long and short period orbits around L_4 . . . 85

5.8 Apocentre d, angle λ_0, phase angle at departure γ_0, parameters that described the geometry of the swing-by, and change in velocity and energy experimented by the spacecraft after the swing-by maneuver is completed, of each trajectory for placing a spacecraft into the long and short period orbits around L_5 86
5.9 Impulsive thrust Δv_1, impulsive stabilizing thrust Δv_2, total cost Δv_T and time of flight Δt of each trajectory for placing a spacecraft into the long and short period orbits around L_4 87
5.10 Impulsive thrust Δv_1, impulsive stabilizing thrust Δv_2, total cost Δv_T and time of flight Δt of each trajectory for placing a spacecraft into the long and short period orbits around L_5 88
5.11 Initial position and velocity coordinates for placing a spacecraft into the long and short period orbits around L_4 (referred to the non-dimensional rotating frame system) corresponding to departure geometries described in Table 5.9 89
5.12 Initial position and velocity coordinates for placing a spacecraft into the long and short period orbits around L_5 (referred to the non-dimensional rotating frame system) corresponding to departure geometries described in Table 5.10 90
5.13 Term ϑ, impulsive thrust Δv_1, stabilizing impulsive thrust Δv_2, total cost Δv_T, time of flight Δt and angle Φ of each trajectory for placing a spacecraft into the long and short period orbits around L_4 93
5.14 Term ϑ, impulsive thrust Δv_1, stabilizing impulsive thrust Δv_2, total cost Δv_T, time of flight Δt and angle Φ of each trajectory for placing a spacecraft into the long and short period orbits around L_5 94
5.15 Initial position and velocity coordinates for placing a spacecraft into the long and short period orbits around L_4 (referred to the non-dimensional rotating frame system) corresponding to departure geometries described in Table 5.13 95
5.16 Initial position and velocity coordinates for placing a spacecraft into the long and short period orbits around L_5 (referred to the non-dimensional rotating frame system) corresponding to departure geometries described in Table 5.14 96
5.17 Parameters of a low-thrust transfer between two circular Earth orbits of radius $r_0 = 6,771$ km and $r_1 = 59,669$ km, and using electric propulsion with continuous constant acceleration ($F = 160$ mN, $I_sp = 1600$ s) 100
5.18 Perturbations Δu_i required for removing the three recurrent loops found between the iterates z_i and z_{i+s} in the chaotic orbit (3.71) 100

5.19 Required boost Δu_N, correction term ς and time of flight Δt_2 since the change in velocity is applied until to reach the periodic orbits around L_4 101
5.20 Required boost Δu_N, correction term ς and time of flight Δt_2 since the change in velocity is applied until to reach the periodic orbits around L_5 102
5.21 Stabilizing impulsive thrust Δv_2, total cost Δv_T and transfer time $\Delta t = \Delta t_1 + \Delta_2$ since the first impulse is applied until to reach the elliptic orbits around L_4 103
5.22 Stabilizing impulsive thrust Δv_2, total cost Δv_T and transfer time $\Delta t = \Delta t_1 + \Delta_2$ since the first impulse is applied until to reach the elliptic orbits around L_5 103
5.23 Cost of maintaining a spacecraft during 1 year considering a radius of 1 km with respect to periodic orbits shown in Fig. 5.1 and the direction in which the relative radial acceleration component is maximum and minimum 109
5.24 Cost of maintaining a spacecraft during 1 year considering a radius of 2 km with respect to periodic orbits shown in Fig. 5.1 and the direction in which the relative radial acceleration component is maximum and minimum 109
5.25 Cost of maintaining a spacecraft during 1 year considering a radius of 1 km and 2 km with respect to periodic orbits shown in Fig. 5.20 and the direction in which the relative radial acceleration component is maximum 110
5.26 Cost of maintaining a spacecraft during 1 year considering a radius of 1 km with respect to periodic orbits shown in Fig. 5.20 and the direction in which the relative radial acceleration component is minimum or zero . 112
5.27 Cost of maintaining a spacecraft during 1 year considering a radius of 2 km with respect to periodic orbits shown in Fig. 5.20 and the direction in which the relative radial acceleration component is minimum or zero . 113
5.28 Cost of maintaining for 1 year a spacecraft with respect to long period family shown in Fig. 5.32 and the direction in which the relative radial acceleration component is maximum, minimum and zero 116
5.29 Cost of maintaining for one year a spacecraft with respect to short period family shown in Fig. 5.32 and the direction in which the relative radial acceleration component is maximum, minimum and zero 117

A.1 Astrodynamic constants 141

CONTENTS

Pág.

1 INTRODUCTION 1

1.1 Objectives 5

1.2 Transfer Orbits Methods 6

1.2.1 Hohmann Transfer Orbit 7

1.2.2 Swing-By Maneuver 9

1.2.3 G Trajectories 11

1.2.4 Chaos Control 11

1.3 Natural Configurations and Controlled Motions Suitable for Formation Flying 14

2 DYNAMICS IN THE CIRCULAR RESTRICTED THREE BODY PROBLEM 19

2.1 Formulation of the Circular Restricted Three Body Problem and Equations of Motion 19

2.2 The Jacobi integral 23

2.3 Lagrangian Equilibrium Points 23

2.4 Zero-Velocity Curves 25

2.5 The Stability of the Lagrangian Equilibrium Points 27

2.6 Equations of Local Dynamics of Satellite Formation Flying 30

2.7 Newton's Method to find Periodic Orbits 32

3 TRANSFER ORBITS 35

3.1 Stabilizing Impulsive Thrust 35

3.2 Modified Hohmann Transfer Orbit 37

3.3 Using the gravitational field of the Moon 40

3.3.1 The Mathematical Description of the Swing-By 42

3.3.1.1 The Geocentric Departure Orbit 43

3.3.1.2 The Selenocentric Arrival Orbit 44

3.3.1.3 Swing-By Maneuver 46

3.3.2 Initial Conditions 50

3.4 G Trajectories for L_4 and L_5 53

3.5 Using Chaos for transference to L4 and L5 Earth-Moon System 58

3.5.1 Entering the Connected Chaotic Component that leads to the Moon . 58

3.5.2 Chaos in the CRTBP 61
3.5.3 Removing Recurrences 64
3.5.4 Reaching L_4 and L_5 68

4 THE ZERO, MINIMUM AND MAXIMUM RELATIVE RADIAL ACCELERATION FOR FORMATION FLYING 71
4.1 The Zero Relative Radial Accelerations Lines 71
4.2 Residual Acceleration and Cost to Maintain a Spacecraft in a Formation 74

5 ANALYSIS AND RESULTS 77
5.1 Long and Short Period Orbits 77
5.2 Modified Hohmann Transfer 78
5.3 Swing-By Maneuver 79
5.4 G Trajectories 84
5.5 Targeting Chaotic Orbits to the equilibrium points L_4 and L_5 through recurrence 91
5.6 The Zero Relative Acceleration Lines in a Long and Short Period Family 98
5.7 Cost to Maintain a Spacecraft on the regions of Zero, Minimum and Maximum Relative Radial Accelerations 106
5.8 Cost to Maintain a Spacecraft on a Fixed Configuration 113
5.9 Dynamical Behaviour of Different Kinds of Solutions 117

6 CONCLUSIONS 129

REFERENCES 133

APPENDIX: ASTRODYNAMIC CONSTANTS 141

1 INTRODUCTION

The concept of Satellite Formation Flying (SFF) means to have two or more satellites in orbit such that their relative positions remain constant or obeying a certain dynamical configuration along the trajectory (SHOLOMITSKY et al., 1977), (BATTRICK, 2000), (BRISTOW et al., 2000), (BURNS et al., 2000), (TICKER; AZZOLINI, 2000), (FRIDLUND, 2000). This concept, illustrated in Fig. 1.1, involves the control over the coordinated movement of a group of satellites, with the goal of maintaining a specific geometric space configuration between the elements of the cluster (SABOL et al., 2001), allowing that a group of low cost small satellites, arranged in a space formation flying, operate like a large 'virtual satellite' which will have many benefits over single satellites including simpler designs, faster build times, cheaper and unprecedented high resolution (KAPILA et al., 2000). There exist missions, such as the Laser Interferometer Space Antenna (LISA), whose objective is to observe astrophysical and cosmological sources of gravitational waves of low frequencies, goal that could be possible using three identical spacecraft flying in a triangular constellation, with equal arms of 5 million kilometers each (PETERSIEM et al., 2000) as shown in Fig. 1.2

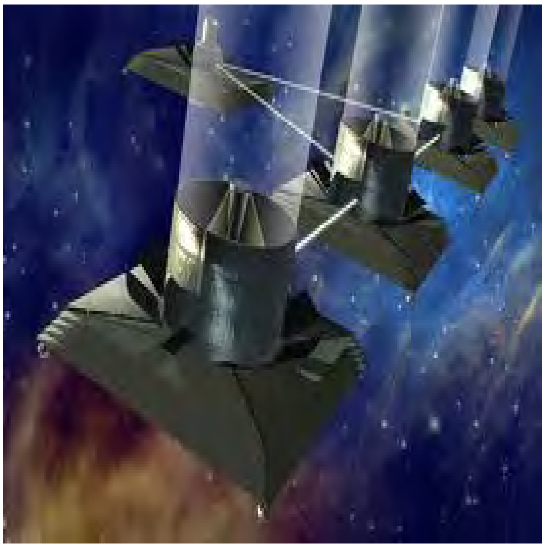

Figure 1.1 - Illustration of Satellite Formation Flying.
From: (JET PROPULSION LABORATORY, 2012).

A configuration of SFF can typically be positioned and maintained in two dynamically distinct scenarios: in a planetary orbit or in outer space (ALFRIEND et al., 2002).

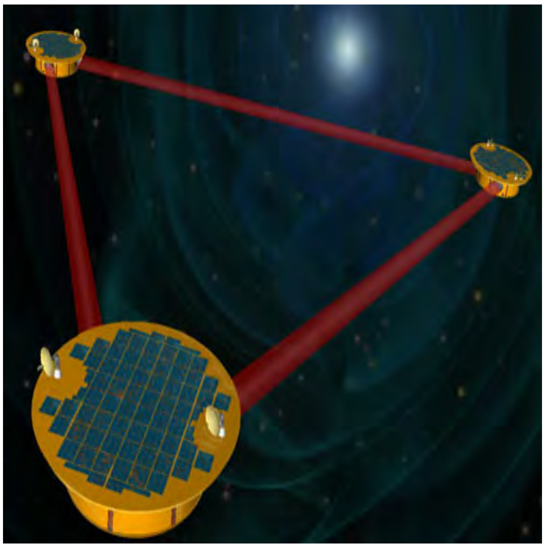

Figure 1.2 - Illustration of LISA spacecraft.
From: (NASA, 2012)

In the planetary orbit scenario the fundamental model is the problem involving two light bodies (satellites), close to each other, that describe initially circular orbits of slightly different radii around a heavy central body (for example, Earth). Because the gravitational attraction between the two satellites is practically null, this scenario can be considered like a superposition of two problems of two bodies. An example of this kind of formation flying is the pair of satellites Landsat 7 with EO-1, mission designed to enable the development of future Earth imaging observatories that will have a significant increase in performance while also having reduced cost and mass (YOUNG, 2012) as shown in Fig. 1.3.

In the outer space scenario, involving SFF, the interest of astronomical missions have been to position SFF around the Lagrangian points L_1 and L_2 (FAQUHAR, 1970), (HENON, 1973), (BREAKWELL; BROWN, 1979), (HOWELL, 1984), (GÓMEZ et al., 1987) or L_4 and L_5. Of particular interest is the stability of the five Lagrangian points. In the case of the three collinear stationary points: L_1, L_2 and L_3, they are always unstable. Whereas the stability of L_4 and L_5 points depends on the mass ratio between the two larger bodies (DANBY, 1962). In important celestial couples like Earth-Moon or Sun-Earth these points are stable. Moreover, there exists a family of periodic orbits around L_4 and L_5. This stability property makes the fuel required for a spacecraft to maintain its relative position there to be almost zero. Despite this advantage, today there are no missions orbiting L_4 or L_5 points for any celestial couple. In the case of Earth-Moon, if a spacecraft were placed at these triangular

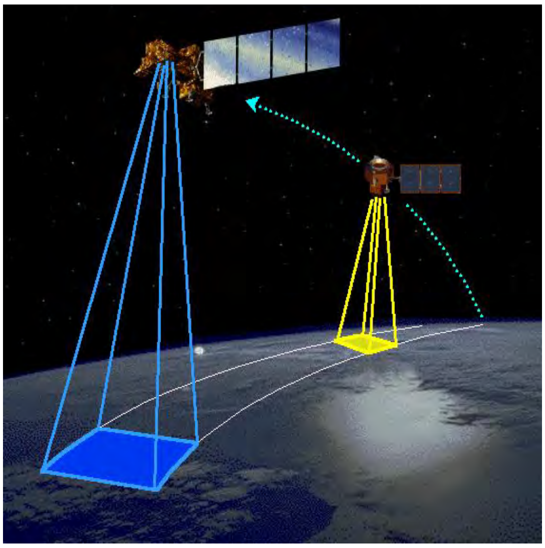

Figure 1.3 - Illustration of satellites Landsat 7 with EO-1 in formation flying.
From: (NASA, 2011)

Lagrangian points, for example, the perturbations due to Earth's electromagnetic interference would be minimal because the distance between the spacecraft and Earth is the same between the Earth and the Moon as shown in Fig. 1.4. In this manner, L_4 and L_5 points could be excellent locations to place space telescopes for astronomical observations or a space station (SCHUTZ, 1977). In addition, there is the renewed interest of major space agencies for Lagrangian point colonization. Furthermore, de Fillipi (FILLIPI, 1978) has made a review of the ideas of O'Neill (O'NEILL, 1974) about building space colonies at the L_4 and L_5 positions. These space stations could be used as a way-point for travel to and from the region between Earth's atmosphere and the Moon (cis-lunar space).

In the other hand, the vicinity of point L_1 of the sun-Earth system is a very convenient location for solar observations because a three-dimensional orbit in its neighborhood would allow that the satellite points constantly toward the sun, without any concealment made by the Earth or lunar eclipse. Additionally, this position is away enough to keep the satellites distant from Earth's electromagnetic interference. Moreover, the vicinity of L_2 is a very convenient location to position satellites for astronomical observations, particularly in the infrared region, because in this vicinity the apparent size of the Earth, which is one of the dominant sources of heat, becomes reduced while all other sources of heat are practically in the same direction, facilitating the shielding of the telescope with respect to solar radiation.

Another example of missions involved Lagrangian points is the NASA's STEREO solar science mission whose objective was to do an excursion to L_4 and L_5 of the Sun-Earth to try and verify a theory by Richard Gott and Edward Belbruno (BELBRUNO; GOTT,) about the origin of the Moon. This theory hypothesizes that a giant Mars-sized impactor, called Theia, hit the Earth to form the Moon billions of years ago. It actually coalesced at Sun-Earth equilateral L_4, L_5 points, 93 million miles from the Earth in either direction, on the Earth's orbit. It is felt that residual material exist near L_4, L_5. To verify this, the STEREO mission, consisting of two spacecraft, were being redirected to go to these points to investigate the possible remains of the mysterious planet that may have been there long ago. An illustration of missions around Lagrangian points L_1 and L_2 in the Sun-Earth system is shown in Fig. 1.5.

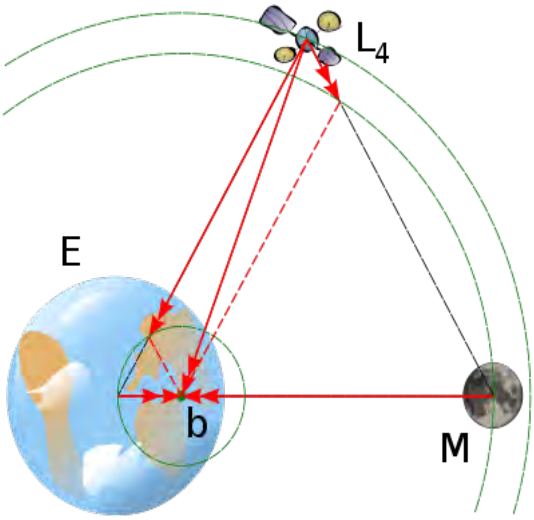

Figure 1.4 - Illustration of a mission around Lagrangian point L_4 in the Earth-Moon system.
From: (WIKIPEDIA, 2012)

One of the problems of positioning satellites in formation flying is the cost to maintain them continuously orbiting each other, requiring higher fuel cost. In particular, missions in the vicinity of the Lagrangian points, considering the scenario of the Circular Restricted Three Body Problem (CRTBP), may be placed in families of halo (periodic and Lissajous (quasi-periodic) orbits. All these orbits are inherently unstable (GÓMEZ; MASDEMONT, 1993), which means that satellites positioned there are very susceptible to perturbations, predominantly in the form of solar radiation pressure. These effects may drive the SFF out of it desired configuration. Thereby, a less difficult option is to place the Satellite Formation Flying in the vicinity of Lagrangian points L_4 and L_5 in the Earth-Moon system. Because they are stable

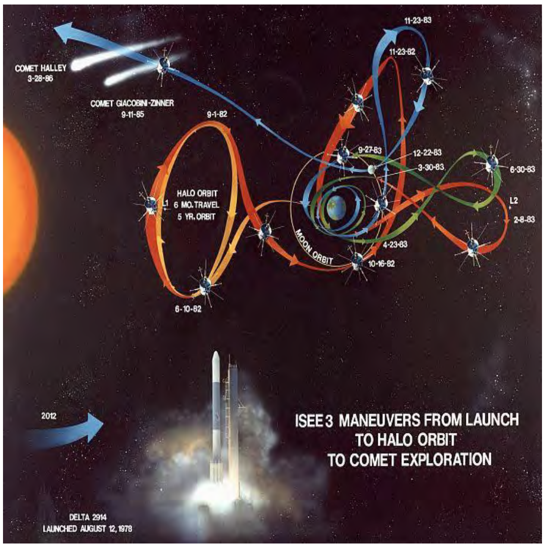
COMET HALLEY
3-28-86
COMET GIACOBINI-ZINNER
9-11-85
9-1-82
11-23-83
11-23-82
9-27-83
12-22-83
3-30-83
6-30-83
HALO ORBIT
6 MO. TRAVEL
5 YR. ORBIT
L1
L2
2-8-83
MOON ORBIT
4-23-83
10-16-82
6-10-82
2012
ISEE 3 MANEUVERS FROM LAUNCH
TO HALO ORBIT
TO COMET EXPLORATION
DELTA 2914
LAUNCHED AUGUST 12, 1978

Figure 1.5 - Illustration of missions around Lagrangian points L_1 and L_2 in the Sun-Earth system.
From (MATHEMATICAL ASSOCIATION OF AMERICA, 2004)

equilibrium points, less energy would be required to keep the formation in its proper configuration.

In despite of the intense research activity directed toward the development of effective techniques that make SFF missions possible in outer space, many challenges must still be faced. Thus, it is necessary to find methods to determine trajectories that exploit the inherent complexity that the dynamic of CRTBP dynamic has, and can be used to delivery the satellites to their locations in the formation flying. The idea is to exploit the dynamics seen in the CRTBP so that, applying certain low cost transfer orbits, the satellites be guided to the desired region where the cost to maintain the formation flying is minimum and make it robust to perturbations.

1.1 Objectives

The objectives in this work are:

a) Development and implementation of alternative transfer strategies to deploy satellites to a formation flight orbiting around the Lagrangian points L_4 and L_5 in the Earth-Moon system. The satellites originally are located in a parking orbit around the Earth.

b) Study of the relative dynamical behaviour of satellites with respect to periodic orbits around L_4 and L_5 and the regions with good properties to formation flying.

1.2 Transfer Orbits Methods

A satellite in orbit on the Earth-Moon system can be described in the context of the Circular Restricted Three Body Problem. In this system, there are equilibrium points named as L_4 and L_5 that may provide a good position to be exploited to positioning spacecrafts. Lagrangian points L_4 and L_5 lie at 60 degrees ahead of and behind Moon in its orbit with respect to the Earth as shown in Fig. 1.6. Each one of them is a third point of an equilateral triangle with the base of the line defined by those two bodies. These Lagrangian points are stable for the Earth-Moon mass ratio. Because of their distance electromagnetic radiations from the Earth arrive on them substantially attenuated. Thus, these Lagrangian points represent remarkable positions to host astronomical observatories. However, this same characteristic distance may be a challenge for periodic servicing mission. Actually, so far there are no missions orbiting the L_4 and L_5 points for any celestial couple. By contrast, there exist several natural examples like Trojan asteroids at the Sun-Jupiter L_4 and L_5 points (YOSHIDA; NAKAMURA, 2005).

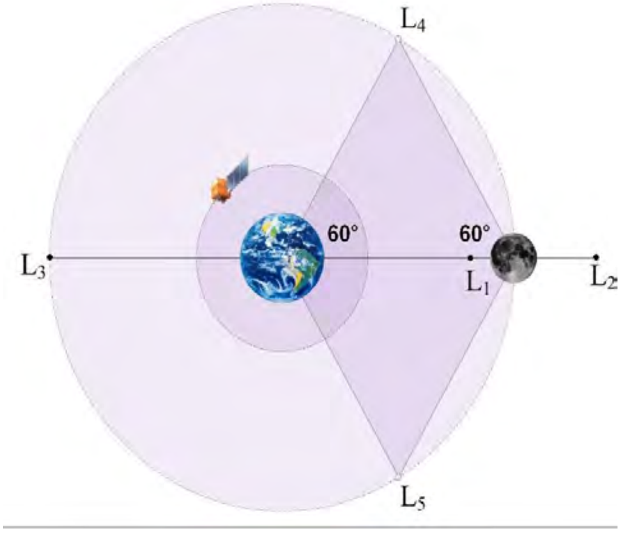

Figure 1.6 - Lagrange equilibrium points geometry for the Earth-Moon system in the synodic frame.
From: (ARAÚJO, 2011)

In this scenario, the Circular Restricted Three Body Problem exhibits dynamical characteristics that allow us to applied alternative techniques to transfer orbits (BOYD; MCMILLAN, 1993), (GÓMEZ et al., 2001a), (GÓMEZ et al., 2001b). In particular, we are interested in the following techniques:

a) Hohmann Transfer Orbit

b) Swing-by Maneuver

c) G Trajectories

d) Chaos Control

For simplicity, our model only considers motions on the plane of the orbit of the Earth-Moon system.

1.2.1 Hohmann Transfer Orbit

The Hohmann transfer orbit is an orbital maneuver that uses two impulses which, under standard assumptions, move a spacecraft between two coplanar circular orbits. Hohmann transfer orbit is the most efficient intermediate orbit to transfer from one circular orbit to another (MCLAUGHLIN, 2000).

Let us consider the case in which a spacecraft has to be brought from a circular orbit of radius r_0 about the Earth to a higher circular orbit of radius r_1 following an elliptic trajectory of minimum energy as shown in Fig. 1.7. This type of minimum energy transfer orbit is commonly referred to as a Hohmann Transfer Orbit. Therefore, the question is to determine the transfer velocity at point P_0 such that the spacecraft reaches the point P_1 following an elliptic trajectory and enters a higher circular orbit. All of this, using minimum energy.

Let $\boldsymbol{v_i}$ denote the orbital velocity of the respective initial circular orbit whose magnitude is given through the energy equation as

$$v_i = \sqrt{\frac{\mu_E}{r_0}}, \tag{1.1}$$

where μ_E is the Earth gravitational constant. The value of the astrodynamic constants used along this work are given in Appendix .

In this manner, Walter Hohmaan showed in 1925 that an elliptic transfer orbit to point P_1 from point P_0 using minimum energy requires a departure velocity $\boldsymbol{v_0}$ at

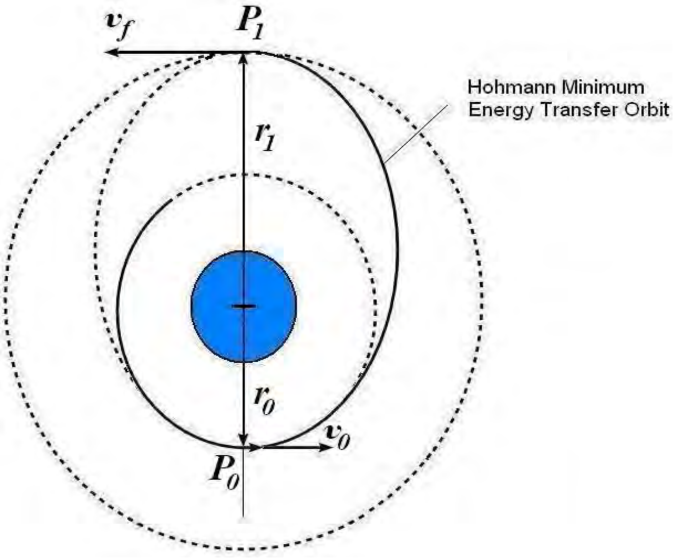

Figure 1.7 - Illustration of a Hohmann Transfer Orbit.

point P_0 given by

$$v_0 \quad = \quad v_i \left(\sqrt{\frac{2r_1}{r_0 + r_1}} \right). \tag{1.2}$$

This fact implies that to achieve point P_1 a change velocity $\Delta \boldsymbol{v_1}$ must be applied

$$\Delta v_1 \quad = \quad v_i \left(\sqrt{\frac{2r_1}{r_0 + r_1}} - 1 \right). \tag{1.3}$$

Being a minimum energy transfer orbit, no radial velocity will be present at this point. Note that one of the focus of this elliptic transfer is precisely the center of the Earth. Since $r_1 > r_0$, Δv_1 will be always positive.

Once the spacecraft reaches the point P_1 a second burn will be necessary to inject it into the circular orbit of radius r_1. The change in velocity Δv_2 of the second burn is given by

$$\Delta v_2 \quad = \quad v_f \left(1 - \sqrt{\frac{2r_0}{r_0 + r_1}} \right), \tag{1.4}$$

where

$$v_f = \sqrt{\frac{\mu_E}{r_1}}. \tag{1.5}$$

The goal of this work is to apply a minimum energy transfer orbit for placing a spacecraft around the Lagrangian points L_4 and L_5.

1.2.2 Swing-By Maneuver

Over the last few years, studies like those of Broucke (BROUCKE, 1979) and Prado (PRADO, 1993) on transfer orbits in the restricted three-body Earth-Moon-particle problem have been analyzed. The solutions found for the Earth-Moon system guide a spacecraft from the Moon to the Lagrangian points and back to the Moon. However, in the case of L_4 and L_5 points, the particle passes very far to the Earth, i.e., it passes an altitude greater than 2,000 kilometers above the Earth's surface. This means that these trajectories are not useful for a transfer between Low Earth Orbits (LEO) and Lagrangian points L_4 and L_5. On the other hand, Broucke (BROUCKE, 1988) showed that the gravitational force of the Moon could be useful to increase or reduce the relative energy of the particle with respect to the Earth. This variation of energy would be enough to change the trajectory of the particle and guide it to a specific position, e.g. L_4 and L_5. This maneuver, known as gravity assist, is usually called 'swing-by' and is illustrated in Fig. 1.8.

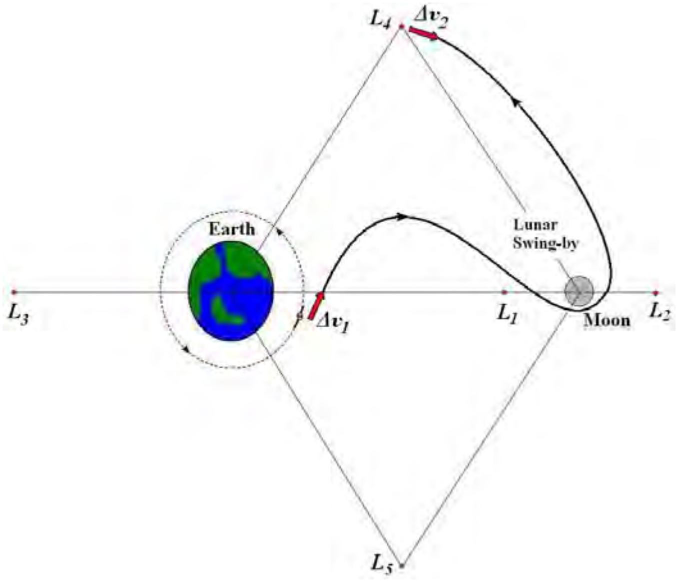

Figure 1.8 - Illustration of a swing-by maneuver with the Moon guiding a spacecraft to L_4.

Therefore, our goal is to use a gravity assist maneuver with the Moon in such a way that a spacecraft can be transferred from a parking orbit around the Earth to the

Lagrangian points L_4 and L_5. For this purpose, depending of the relative energy of the spacecraft to the Earth, the relative orbit of the spacecraft will be one of the three conic solutions of the Two-body problem, i.e., be either elliptic, parabolic, or hyperbolic. The Moon's gravitational force can be considered as a slight perturbation. However, as the spacecraft travels between the Earth and Moon, the lunar effects must be included. In this manner, treating the Moon's gravitational acceleration as a perturbation leads to the concept of sphere of influence (BATTIN, 1987). The sphere of influence is the region around the Moon where the trajectory of any body is largely determined by the lunar force. The gravitational attraction of the Earth would be very small within the Moon's sphere of influence, and therefore this force can be neglected. This concept is illustrated in Fig. 1.9. Thus, we will separate the Earth-Moon-spacecraft problem in two problems of two bodies: Earth-spacecraft and Moon-spacecraft. This approach is called 'patched conic'. While the spacecraft is outside the gravitational sphere of influence of the Moon, the trajectory is approximated taking only the terrestrial gravity into account and using the two-body orbital mechanics. Similarly, once the spacecraft enters the Moon's sphere of influence, we will assume that the spacecraft moves only under the gravitational influence of the Moon. Depending on the speed and direction of the spacecraft relative to the center of the Moon, it is possible to change the energy of the spacecraft relative to the Earth and guide it to the Lagrangian points L_4 and L_5. The key point is, using this approach, to determine the geometry of the geocentric departure orbit such that the spacecraft can be placed around the equilibrium points.

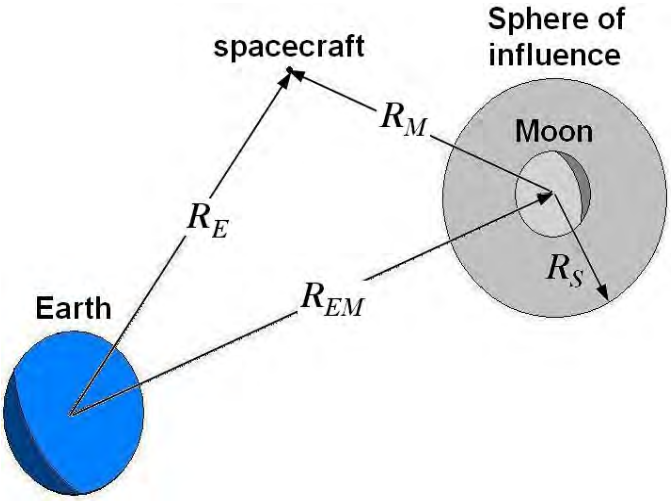

Figure 1.9 - Illustration of the sphere of influence concept in the Earth-Moon system.

1.2.3 G Trajectories

Considering minimum energy trajectories, Prado (PRADO, 1996) obtained a significant reduction in the fuel needed to move between the five Lagrangian points and the Earth-Moon system. In this scenery, alternative transfer techniques between terrestrial orbits and Lagrangian points L_4 and L_5 with a time of flight between 18 and 20 days could be useful. This work has the goal of finding a group of G Trajectories that make such transfers possible.

Over the last few years, studies like those of Broucke and Prado (PRADO; BROUCKE, 1996) were obtained using a regularized model to avoid the numerical integration errors in trajectories passing near one of the primaries. Similarly, the solutions found for the Earth-Moon system guide a spacecraft from the Moon to the Lagrangian points and back to the Moon. However, the particle passes very far from the Earth, thus these trajectories are not useful for a transfer between Low Earth Orbits and Lagrangian points L_4 and L_5.

On the other hand, there is a family of periodic orbits, in the restricted three-body Earth-Moon-particle problem, around the Lagrangian equilibrium point L_1, called G Family (BROUCKE, 1968). Since some orbits of this family pass just a few hundred kilometers from the Earth's surface and, between 13 and 15 days later, they pass just a few dozen kilometers from the Moon's surface (see Fig. 1.10), it is possible to determine trajectories such that, using the lunar gravity, send spacecrafts to the Lagrangian points L_4 and L_5.

This work proposes to investigate a set of trajectories in order to establish parameters for a guided transfer between Earth parking orbits and periodic orbits around L_4 and L_5 that uses the Moon's gravitational force. In this way, a very efficient strategy can be applied to place astronomical missions at the Earth-Moon L_4 and L_5 points.

1.2.4 Chaos Control

Directing a dynamical system to a desired state as quickly as possible is an important goal in many engineering applications. With the development of nonlinear control techniques for chaotic dynamical systems, this so-called ‘targeting’ has become feasible, using small, inexpensive control actions. Applications of nonlinear targeting arise, for example, in space flight, where a spacecraft goes through a chaotic region and has to reach its destination quickly, using as little fuel as possible. Due to the particularly complicated dynamics of the chaotic region, conventional transfer

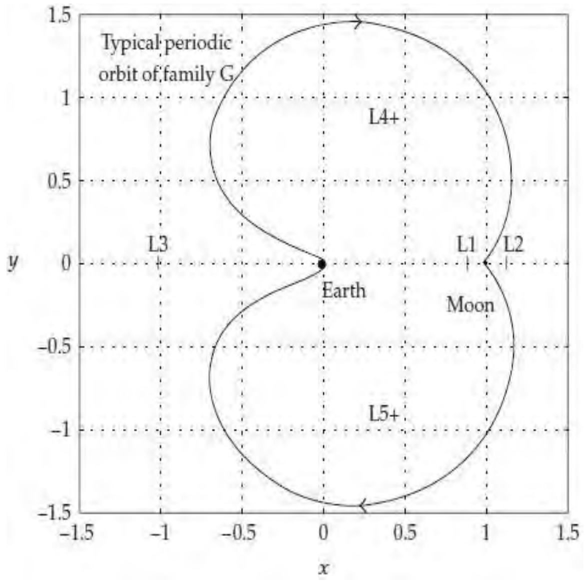

Figure 1.10 - Lagrangian equilibrium points and a typical orbit of the G Family in the synodic frame. (From: (MELO et al., 2007)

techniques often become infeasible. The targeting technique used in this work takes full advantage of the dynamical structure of these systems and yields robust, time optimal trajectories to a desired target.

The control of a dynamical system is usually applied by changing some accessible system parameter or by adding an external force. In space flight applications, for example, impulsive thrusts of a rocket engine are commonly used for trajectory control. With this application in mind we assume, for simplicity's sake, direct access to the phase space momentum variables to achieve control.

Chaos in physical systems like the restricted three body Earth-Moon-particle problem can be exploited to direct a chaotic trajectory to a target (see Fig. 1.11). In particular, the outcome of any given interaction depends sensitively on the initial conditions (OTT, 2002). Chaos is usually viewed as undesirable when designing a space mission: This sensitivity to slight changes in initial conditions makes hard to predict future trajectories, and requires frequent and wasteful control impulses to keep a probe on the desired path. However, in a series of relatively recent works Bollt and Meiss (BOLLT; MEISS, 1995a), (BOLLT; MEISS, 1995b), Schroer and Ott (SCHROER; OTT, 1997), and Macau and Grebogi (MACAU; GREBOGI, 2001), (MACAU; GREBOGI, 2006), (MACAU et al., 2011) present three different ways to drive trajectories in chaotic systems which use only small controls that yield optimal transport times. However, all of these techniques assume that the particle is in the chaotic region. In the case of the restricted three body Earth-Moon-particle problem, the chaotic region is at an altitude of about 59,669 kilometers above the Earth's center (BOLLT; MEISS, 1995b). For example, a Hohmann transfer requires two parallel burns of $\Delta v = 4.1$ km/s approximately to transfer a spacecraft from a circular parking orbit at an altitude of 400 km above the Earth's surface to the chaotic region between the Earth and the Moon (MELO et al., 2007). However, this kind of maneuver is not economically viable. Additionally, de Melo et al. (MELO et al., 2007) showed that this value could be reduced using bi-elliptic transfers, such that the total change in velocity obtained was between 3.5 km/s and 3.7 km/s. Although the total change is less than the Hohmann transfer, the maneuver could be not economically viable if the mission needs to spend more fuel to guide the spacecraft to the Lagrangian equilibrium points L_4 or L_5.

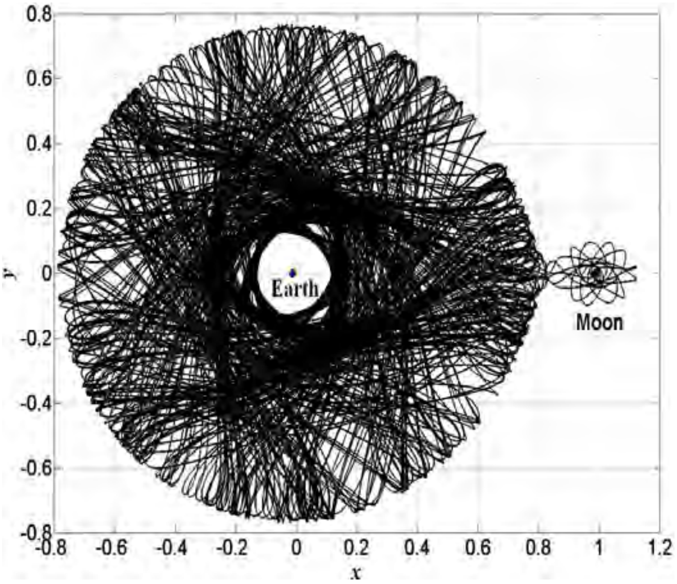

Figure 1.11 - Chaotic Trajectory in the Earth-Moon system in the synodic frame.

This work proposes a new low-cost orbital transfer strategy that uses a hybrid propulsion system. Firstly, electric propulsion to transfer a spacecraft from a LEO with an altitude of 400 km from Earth's surface to a higher circular orbit of 59,669 km above the Earth's center. Once the spacecraft reaches this altitude, a chemical thruster makes a first impulse to enter the chaotic region between the Earth and Moon, in such a way that, using only small perturbations, the spacecraft can reach the Moon through the connected chaotic component and using the Moon's gravitational force, the spacecraft finally arrives at the equilibrium points L_4 or L_5 as illustrated in Fig. 1.12.

The total cost of the transfer orbits implemented in this work are given in terms of the sum of all required changes in velocities to reach the equilibrium points and finally to stabilize the spacecraft around them.

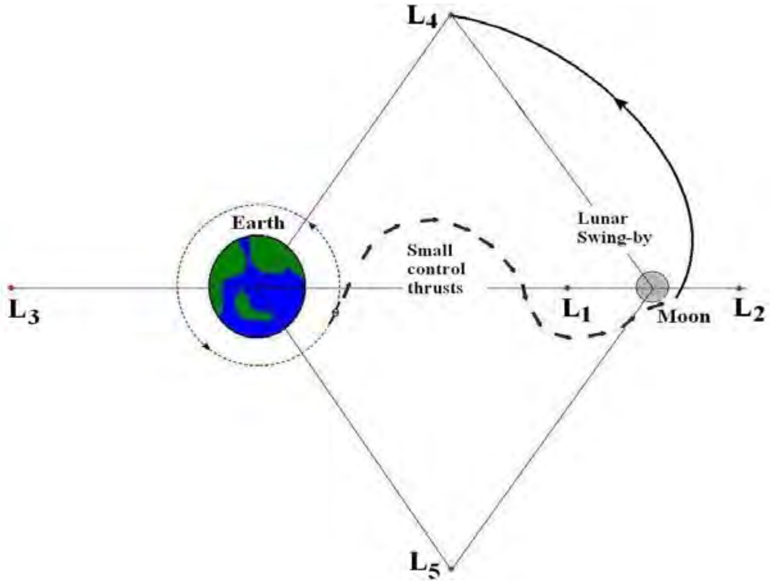

Figure 1.12 - Illustration of the controlled chaotic trajectory reaching Lagrange equilibrium point L_4 for the Earth-Moon system.

1.3 Natural Configurations and Controlled Motions Suitable for Formation Flying

The simplest type of spacecraft formation flying geometry is the leader-follower type shown in Fig. 1.13. Here the two spacecraft are essentially in identical orbits, but separated from each other only by different anomalies. If this orbit is circular, then the spacecraft separation will remain fixed. If the orbit is elliptic, then the spacecraft separation will contract and expand over the time.

The satellite about which all other satellite motions are referenced is called the chief satellite. The remaining satellites, referred to as the deputy satellites, are to fly in formation with the chief. It is not necessary that the chief position is occupied by a physical satellite, the chief position could be used as an orbiting reference point about which the deputy satellites orbit.

A dynamical more challenging type of general spacecraft formation flying than the

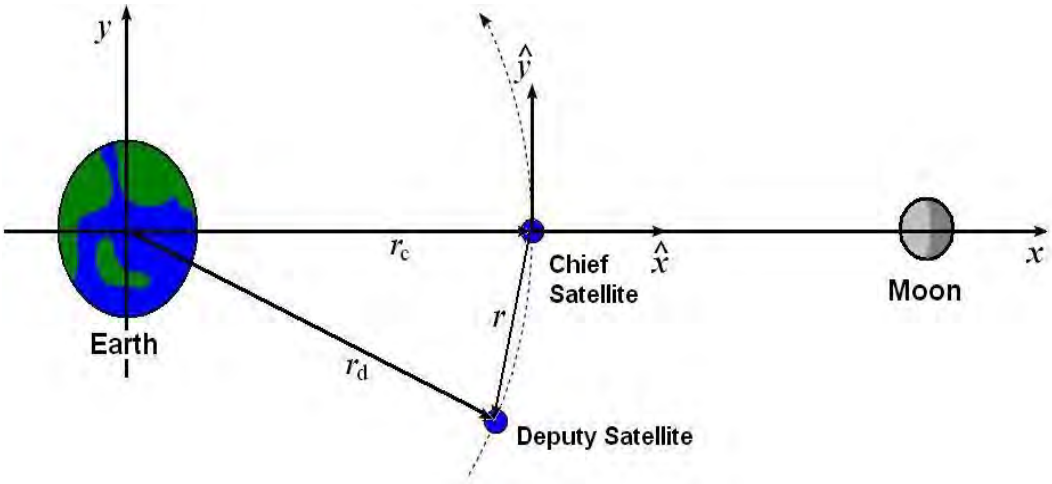

y
$\hat{y}$
r_c
Chief Satellite
$\hat{x}$
Moon
x
Earth
r
r_d
Deputy Satellite

Figure 1.13 - Illustration of a leader-follower type of a two-spacecraft formation.

leader-follower type is shown in Fig. 1.14. Here several spacecrafts are on slightly different orbits according some specific constraints to ensure that the relative orbits are bounded and that the spacecrafts will not drift apart. Note that here the chief satellite (or chief position) is the one in relative interior orbit about which all of the other deputy satellites are orbiting. In particular, Figure 1.14 shows the chief satellite placed in a periodic orbit around L_4. The goal of this work is to place a constellation of satellites such that the chief position is in a periodic orbit around L_4 or L_5.

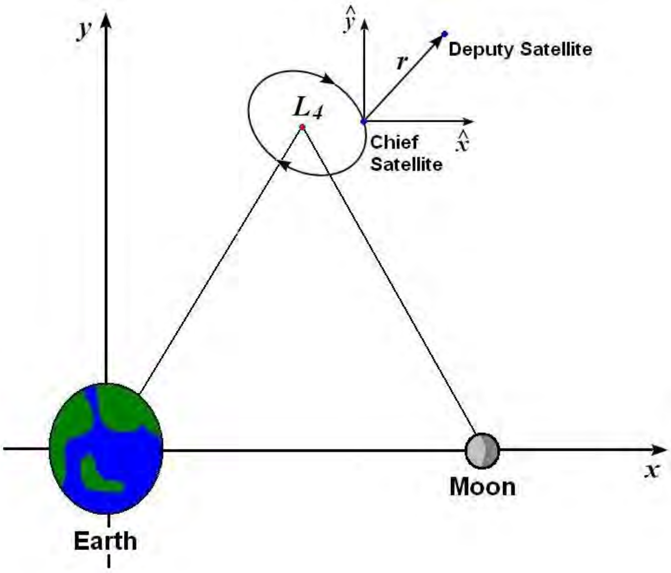

y
$\hat{y}$
r
Deputy Satellite
L_4
Chief Satellite
$\hat{x}$
Moon
x
Earth

Figure 1.14 - Illustration of a general type of spacecraft formation where the chief satellite is placed in a periodic orbit around L_4.

In the synodic frame referential system, the chief and deputy positions are given by the vectors $\boldsymbol{r_c}$ and $\boldsymbol{r_d}$, respectively. The relative deputy satellite position is given by $\boldsymbol{r}$, where its origin is at the chief satellite position and its orientation is given by the unit vectors $\{\hat{\boldsymbol{x}}, \hat{\boldsymbol{y}}\}$ which are parallel to the synodic frame as shown in Figs. 1.13 and 1.14. Since the present work is devoted to study natural configurations suitable for formation flying, we are interested in to find the relative deputy positions such that large variations of the mutual distance between the spacecrafts are avoided. In Fig. 1.15, we depict three cases of variations of the mutual distance between the spacecrafts in a formation flying. Supposing that the relative deputy velocity is zero, if the initial relative deputy position at instant $t = t_0$ is the vector $\boldsymbol{r_1}$ or $\boldsymbol{r_3}$, the behaviour of the relative distance changes over the time such that at instant $t = t_1$, the separation from the chief satellite is larger or smaller than the initial state, respectively. However, if the initial relative deputy position is the vector $\boldsymbol{r_2}$, the relative distance remains constant until the instant $t = t_1$. What determines the characteristics of this behaviour is the radial component of the relative deputy acceleration (GÓMEZ et al., 2006). In the two first cases explained previously, the relative radial acceleration is positive or negative, but in the third one, it is zero. Therefore, a deputy satellites, with zero relative velocity placed in the region where the relative radial acceleration is zero will keep fixed their mutual relative distance.

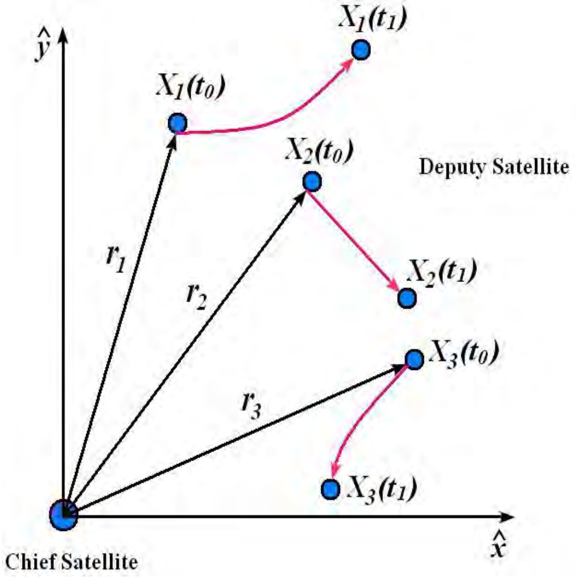

Figure 1.15 - Illustration of three cases of variations of the mutual distance between the spacecrafts in a formation flying.

In this work, we present analytical and numerical methods based on the linearization of the relative equations of motion to find the regions where the relative radial componente of the relative acceleration is zero. Gómez et al. (GÓMEZ et al., 2006) applied the same methodology for halo orbits around the collinear equilibrium point L_2, which is unstable, in the Sun-Earth system. In our case, we are interested in to apply it in periodic orbits around the equilateral equilibrium points L_4 and L_5, which are stable, in the Earth-Moon system. Additionally, the cost to maintain a formation flying placed on these regions is compared from other geometries as well as an analysis of the expansion or contraction of the configuration.

2 DYNAMICS IN THE CIRCULAR RESTRICTED THREE BODY PROBLEM

The fundamental model applied in the scenario of transfer orbits and Satellite Formation Flying in the Earth-Moon system is the Circular Restricted Three Body Problem (CRTBP) (SZEBEHELY, 1967) which is obtained from the model of the three body problem with the Earth and the Moon as the primaries and using the following simplifications:

a) the lunar eccentricity is zero,

b) the lunar inclination is zero.

The first simplification implies that the two primaries are in circular orbits about their mutual center of mass, and the second one involves that the spacecraft can move from one point in the plane defined by the two revolving bodies to another point in the same plane without to change the plane orientation of the initial parking orbit. These two simplifications satisfy the hypothesis of the Minimum Energy Transfer (see Sect. 1.2.1).

In the following sections first the equations of motion are derived, assuming motions only on the plane of the orbit of the Earth-Moon system. The Jacobian integral, the Lagrangian points, the zero-velocity curves and the stability of the Lagrangian points are treated next. Finally, the equations of relative motion of formation flying are derived as well as numerical methods to find periodic solutions in the CRTBP.

2.1 Formulation of the Circular Restricted Three Body Problem and Equations of Motion

In this section we show how the equations of the CRTBP problem are derived from the equations of motion of the general problem of three bodies. Here the three bodies will be the Earth, the Moon, and the spacecraft, and their masses denoted by m_E, m_M, and m, respectively, such that $m << m_M < m_E$. The position vectors of the Earth, the Moon, and the spacecraft relative to an inertial origin with perpendicular axes ξ, η centered at the barycenter are $\boldsymbol{r_E}$, $\boldsymbol{r_M}$, and $\boldsymbol{r}$, respectively, as shown in Fig. 2.1.

Let the coordinates of the Earth, the Moon and the spacecraft in the inertial system be (ξ_E, η_E), (ξ_M, η_M), and (ξ, η), respectively. Then applying the vector form of the

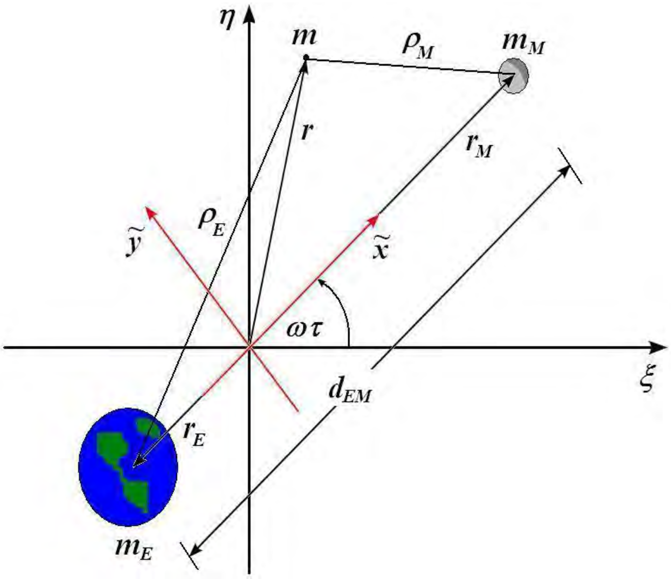

Figure 2.1 - Illustration of Circular Restricted Three Body Problem: Earth-Moon-particle.

inverse square law, the equations of motion of the particle are

$$\ddot{\xi} = \frac{Gm_E}{\rho_E^3}(\xi_E - \xi) + \frac{Gm_M}{\rho_M^3}(\xi_M - \xi), \tag{2.1}$$

$$\ddot{\eta} = \frac{Gm_E}{\rho_E^3}(\eta_E - \eta) + \frac{Gm_M}{\rho_M^3}(\eta_M - \eta), \tag{2.2}$$

where G is the universal gravitational constant and ρ_E and ρ_M are the distances of spacecraft to the Earth and the Moon, respectively. Dots denote derivatives with respect to the dimensional time τ.

Consider a new, rotating coordinate system with perpendicular axes $\tilde{x}$, $\tilde{y}$ that has the same origin as the ξ, η system but which is rotating at a uniform rate given by the Kepler's third law of planetary motion

$$\omega = \sqrt{\frac{G(m_E + m_M)}{d_{EM}^3}}, \tag{2.3}$$

where d_{EM} denotes the constant relative $m_E - m_M$ distance. The direction of the $\tilde{x}$ is chosen such that the two primaries lie along it. This coordinate system is called synodic.

Substituting the value of the constants G, m_E, m_M and d_{EM} (see Appendix) in Eq. 2.3, the magnitude of the constant angular velocity ω of the Earth-Moon system is equal to

$$\omega \;=\; 2.66525 \times 10^{-6}\ \frac{\mathrm{rad}}{\mathrm{s}}.$$

Let the coordinates of the Earth, the Moon and the spacecraft in the rotational system be $(\tilde{x}_E, \tilde{y}_E)$, $(\tilde{x}_M, \tilde{y}_M)$, and $(\tilde{x}, \tilde{y})$, respectively. At instant τ, the synodic system has rotated an angle $\omega\tau$. Thus, these coordinates are related to the coordinates in the inertial system by the following rotation

$$\begin{pmatrix} \xi \\ \eta \end{pmatrix} \;=\; \begin{pmatrix} \cos\omega\tau & -\sin\omega\tau \\ \sin\omega\tau & \cos\omega\tau \end{pmatrix} \begin{pmatrix} \tilde{x} \\ \tilde{y} \end{pmatrix}. \tag{2.4}$$

Differentiating each component in Eq. (2.4) twice we obtain

$$\begin{pmatrix} \ddot{\xi} \\ \ddot{\eta} \end{pmatrix} \;=\; \begin{pmatrix} \cos\omega\tau & -\sin\omega\tau \\ \sin\omega\tau & \cos\omega\tau \end{pmatrix} \begin{pmatrix} \ddot{\tilde{x}} - 2\omega\dot{\tilde{y}} - \omega^2\tilde{x} \\ \ddot{\tilde{y}} + 2\omega\dot{\tilde{x}} - \omega^2\tilde{y} \end{pmatrix}. \tag{2.5}$$

Note that in the synodic frame, it was introduced the terms $\omega\dot{\tilde{x}}$, $\omega\dot{\tilde{y}}$ that represent the Corioli's acceleration and $\omega^2\tilde{x}$, $\omega^2\tilde{x}$ that represent the centrifugal acceleration. Using these substitutions for ξ, η, $\ddot{\xi}$, $\ddot{\eta}$ in Eqs. (2.1) and (2.2) and after some algebraic manipulations we obtain the equations of motion in the synodic system:

$$\ddot{\tilde{x}} - 2\omega\dot{\tilde{y}} - \omega^2\tilde{x} \;=\; -G\left(\frac{m_E}{\rho_E^3}\left(\tilde{x}_E - \tilde{x}\right) + \frac{m_M}{\rho_M^3}\left(\tilde{x}_M - \tilde{x}\right)\right), \tag{2.6}$$

$$\ddot{\tilde{y}} + 2\omega\dot{\tilde{y}} - \omega^2\tilde{x} \;=\; -G\left(\frac{m_E}{\rho_E^3} + \frac{m_M}{\rho_M^3}\right)\tilde{y}. \tag{2.7}$$

The equations of motion in Eqs. (2.6) and (2.7) can be written in a convenient non-dimensional form. Firstly, we introduce the non-dimensional time variable t as

$$t \;=\; \omega\tau. \tag{2.8}$$

The non-dimensional time derivative is related to the previous time derivate through

$$\frac{d\tilde{x}}{d\tau} \;=\; \omega\frac{d\tilde{x}}{dt}, \tag{2.9}$$

$$\frac{d^2\tilde{x}}{d\tau^2} \;=\; \omega^2\frac{d^2\tilde{x}}{dt^2}. \tag{2.10}$$

Now, any scalar distances are non-dimensionalized by dividing them with the constant distance d_{EM} as

$$x = \frac{\tilde{x}}{d_{EM}} \qquad y = \frac{\tilde{y}}{d_{EM}} \qquad x_E = \frac{\tilde{x}_E}{d_{EM}} \qquad x_M = \frac{\tilde{x}_M}{d_{EM}}. \tag{2.11}$$

Finally, the mass quantities are non-dimensionalized by introducing the scalar parameter μ as

$$\mu = \frac{m_M}{m_E + m_M}. \tag{2.12}$$

Similarly, substituting the value of the Earth and Moon masses (see Appendix) in Eq. 2.12, the scalar parameter μ of the Earth-Moon system is equal to

$$\mu = 0.01215.$$

Note that with this new non-dimensional quantities, the unit distance between the masses m_E and m_M, and the definition of the barycenter imply that

$$x_M - x_E = 1, \tag{2.13}$$

$$(1-\mu)\, x_E + \mu x_M = 0. \tag{2.14}$$

Using Eqs. (2.13) and (2.14), the non-dimensional coordinates of m_E and m_M in terms of the parameter μ are given by

$$x_E = -\mu, \tag{2.15}$$

$$x_M = 1 - \mu. \tag{2.16}$$

Combining all of these definitions, the equations of motion of m in Eqs. (2.6) and (2.7) can be rewritten in the following non-dimensional form:

$$\ddot{x} - 2\dot{y} = \frac{\partial U}{\partial x}, \tag{2.17}$$

$$\ddot{y} + 2\dot{x} = \frac{\partial U}{\partial y}, \tag{2.18}$$

where $U = U(x, y)$ is given by

$$U(x,y) = \frac{1}{2}\left(x^2+y^2\right) + \frac{1-\mu}{\rho_E} + \frac{\mu}{\rho_M}, \tag{2.19}$$

and the non-dimensional relative distance ρ_i is defined as

$$\rho_i = \sqrt{(x-x_i)^2+y^2}. \tag{2.20}$$

U is called a 'pseudo-potential'. Similarly, dots denote derivatives with respect to the non-dimensional time t.

2.2 The Jacobi integral

If we multiply Eq. (2.17) by $\dot{x}$ and (2.18) by $\dot{y}$, and add the results, the non-dimensional equations of motion in the synodic system become

$$\dot{x}\ddot{x} + \dot{y}\ddot{y} = \frac{\partial U}{\partial x}\dot{x} + \frac{\partial U}{\partial y}\dot{y}, \tag{2.21}$$

$$\frac{1}{2}\frac{d}{dt}\left(\dot{x}^2+\dot{y}^2\right) = \frac{dU}{dt}. \tag{2.22}$$

Integrating Eq. (2.22) with respect to time yields a global integral of the motion C:

$$\dot{x}^2+\dot{y}^2 = 2U - C, \tag{2.23}$$

Then for Eq. (2.19),

$$\left(x^2+y^2\right) + \left(\frac{1-\mu}{\rho_E} + \frac{\mu}{\rho_M}\right) - \dot{x}^2 - \dot{y}^2 = C. \tag{2.24}$$

This is the Jacobi integral, or Jacobi constant, and is the only integral of the motion in the Restricted Three Body Problem (SZEBEHELY, 1967).

2.3 Lagrangian Equilibrium Points

Setting the velocities and accelerations in Eqs. (2.17) and (2.18) equal to zero, we obtain the conditions that are satisfied by the equilibrium points of the CRTBP:

$$x - (1-\mu)\frac{x+\mu}{\rho_E^3} - \mu\frac{x-1+\mu}{\rho_M^3} = 0 \tag{2.25}$$

$$\left(1 - \frac{1-\mu}{\rho_E^3} - \frac{\mu}{\rho_M^3}\right)y = 0. \tag{2.26}$$

Equation (2.26) is only equal to zero for two geometric configurations. Either $y = 0$ which corresponds to the collinear solution with all bodies aligned with the rotating axis $\tilde{x}$, or $\rho_E = \rho_M = 1$, which corresponds to the equilateral triangle solution. Substituting $y = 0$ in Eq. (2.25) leads to the expression

$$x - (1-\mu)\frac{x+\mu}{|x+\mu|^3} - \mu\frac{x-1+\mu}{|x-1+\mu|^3} = 0. \tag{2.27}$$

Solving Eq. (2.27), we find the x coordinates of the three collinear equilibrium points denoted by L_1, L_2, and L_3 for the Earth-Moon system:

$$L_1: \quad x = 0.836915 \qquad L_2: \quad x = 1.15568 \qquad L_3: \quad x = -1.00506$$

Note that, the L_1 point is between the Earth-Moon system, the L_3 is on the 'backside' of the Earth, and L_2 is on the 'backside' of the Moon a shown in Fig. 1.6.

Finally, the equilibrium condition $\rho_E = \rho_M = 1$ yields to find the coordinates for the two equilateral equilibrium points denoted by L_4 and L_5:

$$L_4: \quad x = \frac{1}{2} - \mu, \; y = \sqrt{3}/2,$$

$$L_5: \quad x = \frac{1}{2} - \mu, \; y = -\sqrt{3}/2.$$

The five equilibrium points L_1, L_2, L_3, L_4 and L_5 are called Lagrangian equilibrium points and were discovered by mathematicians Leonard Euler (EULER, 1776) and Josep-Lois Lagrange (LAGRANGE, 1772) in the eighteenth century. Table 2.1 shows the coordinates of the Lagrangian equilibrium points on the Earth-Moon plane.

Table 2.1 - Coordinates of the Lagrangian Equilibrium points on the Earth-Moon plane

Lagrangian equilibrium point	x	y
L_1	0.836915	0
L_2	1.15568	0
L_3	-1.00506	0
L_4	0.48785	0.86603
L_5	0.48785	-0.86603

2.4 Zero-Velocity Curves

A common use of the Jacobi integral is to establish regions around m_E and m_M within which m may travel given its initial states. Equation (2.23) implies that $2U \geq C$ otherwise the velocity of m would be complex. Therefore, $2U = C$ defines the boundary curves of region where particle motion is not possible. Setting $\dot{x} = \dot{y} = 0$ in Eq. (2.24) for a given constant C, provides an algebraic expression for the regions of the $x - y$ space where the particle can not be:

$$\left(x^2 + y^2\right) + \left(\frac{1-\mu}{\rho_E} + \frac{\mu}{\rho_M}\right) \quad = \quad C. \tag{2.28}$$

Figure 2.2 shows selected zero-velocity curves for the Earth and Moon system. For example, from Fig. 2.2a we can see that if a particle with that value of C is in the unshaded region around the Earth then it can never orbit the Moon or escape from the system because it would have to cross the excluded region to do so. Similarly, in Fig. 2.2b, if a particle is orbiting the Earth then it is possible that it could orbit the Moon, but it could never escape from the system.

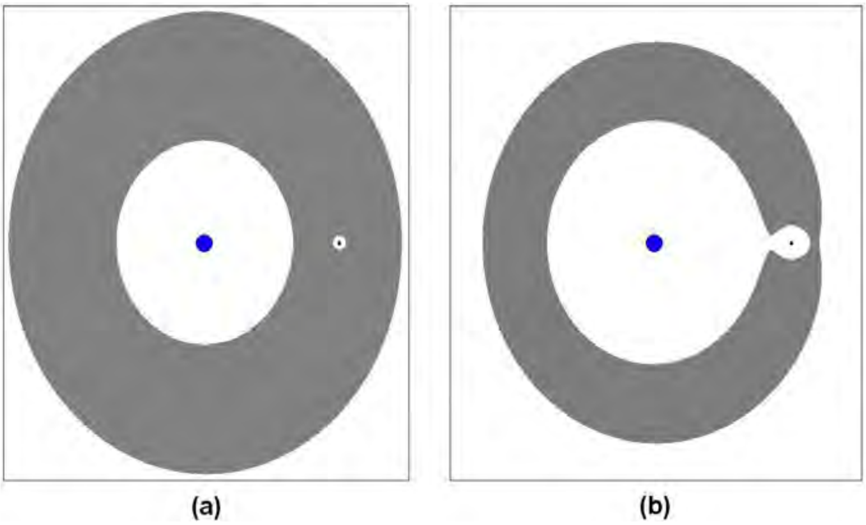

Figure 2.2 - Zero-velocity curves for the Earth-Moon system. The values of C are (a) $C = 3.50$ and (b) $C = 3.18$. The shaded areas denote the exclude regions.

Substituting the non-dimensional coordinates of the L_i Lagrangian equilibrium points (see Table 2.1) in Eq. 2.28, we obtain the critical values C_i which corresponds to the regions such that the Lagrangian points are reachable in the Earth-Moon system. Table 2.2 shows the critical values of C and the corresponding Lagrangian points that are reachable. Similarly, in Fig. 2.3, we show the zero-relative curves of the Earth-Moon system touching the Lagrangian equilibrium points. As we can see the equilibrium points L_4 and L_5 are reachable if and only if $C \leq C_4$. This fact is important for us due to we are interested in to guide a formation flying around them.

Table 2.2 - Critical values of C and the corresponding Lagrangian points that are reachable in the Earth-Moon system

C	Value	Reachable Lagrangian Points
C_1	3.1883	L_1
C_2	3.1721	L_1, L_2
C_3	3.0121	L_1, L_2, L_3
C_4	2.9879	L_1, L_2, L_3, L_4, L_5

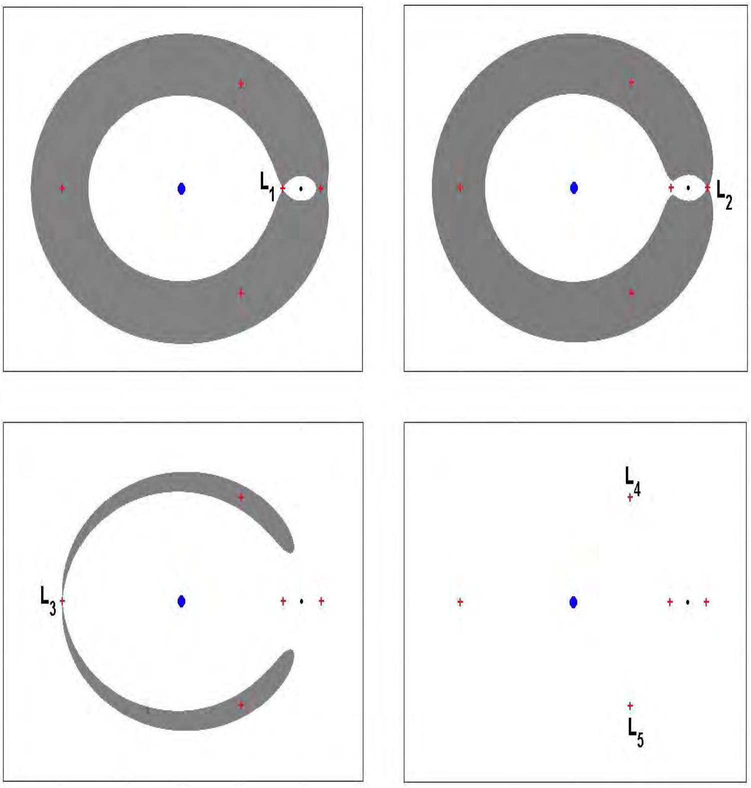

Figure 2.3 - Critical Zero-Velocity curves about Earth and Moon touching the Lagrangian equilibrium points.

2.5 The Stability of the Lagrangian Equilibrium Points

Let the coordinates of the Lagrangian equilibrium points be (x^*, y^*) and let the position of mass m be $(x^* + x', y^* + y')$ where x' and y' are small. Substituting the coordinates $x = x^* + x'$, $y = y^* + y'$ of the mass m in Eqs. (2.17) and (2.18), and expanding the partial derivatives $\partial U/\partial x$, $\partial U/\partial y$ around (x^*, y^*) by using the Taylor's theorem (LANG, 1997), we have that, considering only the linear terms and remembering that $\partial U/\partial x = \partial U/\partial y = 0$ at (x^*, y^*), the equations of motion around the Lagrangian Equilibrium points are

$$\ddot{x}' - 2\dot{y}' = x'\left(\frac{\partial^2 U}{\partial x^2}\right)_* + y'\left(\frac{\partial^2 U}{\partial x \partial y}\right)_*, \tag{2.29}$$

$$\ddot{y}' + 2\dot{x}' = x'\left(\frac{\partial^2 U}{\partial y \partial x}\right)_* + y'\left(\frac{\partial^2 U}{\partial^2 y}\right)_*, \tag{2.30}$$

where the subscript $*$ denotes evaluation of the partial derivatives at the points of equilibrium so they have constant values.

For a collinear equilibrium point for which $y^* = 0$, we have

$$\ddot{x}' - 2\dot{y}' = x'(1 + 2\zeta), \tag{2.31}$$

$$\ddot{y}' + 2\dot{x}' = y'(1 - \zeta), \tag{2.32}$$

where ζ is defined by

$$\zeta = \frac{1-\mu}{\rho_E^3} + \frac{\mu}{\rho_M^3}. \tag{2.33}$$

We try a solution $x' = Ae^{\lambda t}$, $y' = Be^{\lambda t}$. Substituting the trial solutions into Eqs. (2.31) and (2.32), we have

$$\lambda^4 + (2-\zeta)\lambda^2 + (1+2\zeta)(1-\zeta) = 0. \tag{2.34}$$

The roots for λ^2 are given by

$$\lambda_1^2 = \frac{-(2-\zeta) + \sqrt{(2-\zeta)^2 - 4(1+2\zeta)(1-\zeta)}}{2}, \tag{2.35}$$

$$\lambda_2^2 = \frac{-(2-\zeta) - \sqrt{(2-\zeta)^2 - 4(1+2\zeta)(1-\zeta)}}{2}. \tag{2.36}$$

Now by Eq. (2.27) we know that

$$x^{*}-(1-\mu)\frac{x^{*}+\mu}{\rho_E^3}-\mu\frac{x^{*}-1+\mu}{\rho_M^3} = 0.$$

This expression can be written in the form

$$x^{*}\left(1-\frac{1-\mu}{\rho_E^3}-\frac{\mu}{\rho_M^3}\right)-\mu\left(1-\mu\right)\left(\frac{1}{\rho_E^3}-\frac{1}{\rho_M^3}\right) = 0.$$

So, using the definition of ς, we find that

$$1-\zeta = \frac{\mu\left(1-\mu\right)}{x^{*}}\left(\frac{1}{\rho_E^3}-\frac{1}{\rho_M^3}\right). \qquad (2.37)$$

From simples inspection we have for L_1 and L_2 that $x^{*} > 0$ and $\rho_E > \rho_M$, then $1-\zeta < 0$. Similarly, we have for L_3 that $x^{*} < 0$ and $\rho_E < \rho_M$, thus $1-\zeta < 0$. Therefore for each collinear equilibrium point $\lambda_1^2 > 0$ and $\lambda_2^2 < 0$. This means that the collinear equilibrium points are unstable. However, the purely imaginary roots imply that there exits infinitesimal periodic orbits around the collinear points. These periodic orbits correspond to a family which can be generated from infinitesimal elliptic orbits around the equilibrium points (BROUCKE, 1962). An example of this family is the G Trajectories which represent a set of periodic orbits around L_1 in the Earth-Moon system as shown in Fig. 1.10.

Now we analyze the stability of the triangular equilibrium points. We have $x^{*}=\frac{1}{2}-\mu$, $y^{*}=\pm\sqrt{3}/2$, and $\rho_E=\rho_M=1$. The equations of motion are

$$\ddot{x}'-2\dot{y}' = \frac{3}{4}x'+\frac{3\sqrt{3}}{4}\left(1-2\mu\right)y', \qquad (2.38)$$

$$\ddot{x}'+2\dot{y}' = \frac{9}{4}y'+\frac{3\sqrt{3}}{4}\left(1-2\mu\right)x'. \qquad (2.39)$$

We again try a solution $x'=Ae^{\lambda t}$, $y'=Be^{\lambda t}$. Substituting the trial solutions into Eqs. (2.38) and (2.39), we have

$$\lambda^4+\lambda^2+\frac{27}{4}\mu\left(1-\mu\right) = 0. \qquad (2.40)$$

The roots for λ^2 are given by

$$\lambda_1^2 = \frac{-1+\sqrt{1-27\mu\left(1-\mu\right)}}{2}, \tag{2.41}$$

$$\lambda_2^2 = \frac{-1-\sqrt{1-27\mu\left(1-\mu\right)}}{2}. \tag{2.42}$$

For stability λ must be purely imaginary so that there must be two real negative roots for λ^2. Substituting the mass ratio $\mu = 0.01215$, we find that the condition

$$1-27\mu\left(1-\mu\right) > 0 \tag{2.43}$$

is satisfied for the Earth-Moon system. This implies that the roots will occur in pairs of the form $\lambda_{1,2} = \pm ik_1$ and $\lambda_{3,4} = \pm ik_2$, where k_1, k_2 are real numbers and $k_1 = 0.2982$, $k_2 = 0.9545$ for this system. Since x', y', $\dot{x}'$, $\dot{x}'$ must all be real, the coefficients of the exponential terms consist of complex conjugates. Hence our solution for x' can be written

$$\begin{aligned} x'\left(t\right) &= \left(a_1+ib_1\right)e^{ik_1t}+\left(a_1-ib_1\right)e^{-ik_1t} \\ &\quad +\left(a_2+ib_2\right)e^{ik_2t}+\left(a_2-ib_2\right)e^{-ik_2t}, \end{aligned} \tag{2.44}$$

with a similar equation for $y'\left(t\right)$. Since $e^{i\theta} = \cos\theta + i\sin\theta$ and the coefficients are complex conjugates, Equation (2.44) can be rewritten as

$$x'\left(t\right) = 2\left(a_1\cos k_1t - b_1\sin k_1t\right) + 2\left(a_2\cos k_2t - b_2\sin k_2t\right). \tag{2.45}$$

So the resulting motion of the particle displaced from the equilibrium point L_4 (or L_5) in the Earth-Moon system is oscillatory in form; hence the particle will remain in the vicinity of the equilibrium point and the motion is stable. Note that the both purely imaginary roots for λ implies the existence of these two frequencies in the solution for x' and y'. Therefore the motion is the superposition of two harmonic oscillations: a short-period motion with a period $2\pi/\left|k_2\right| \approx 2\pi$ and a superimposed longer period motion with a period $2\pi/\left|k_1\right|$ about the equilibrium point. In the system of units that we have chosen the short period is approximately the same as the period of the revolution of the primaries.

After the elimination of either the short- or the long-period terms, the orbit of the particle becomes an ellipse which can be seen in Eq. (2.45). Figure 2.4 shows two elliptic orbits of periods 6.58 and 21.07 non-dimensional units around L_4 for the Earth and the Moon system. The center of the ellipses is at the origin of the coordinate system with perpendicular axes x', y' which coincides with L_4. The principal axes of the ellipses are rotated relative to the coordinate system x', y' by an angle α given by (SZEBEHELY, 1967):

$$\alpha = \frac{1}{2}\tan^{-1}\sqrt{3}\,(1-2\mu). \tag{2.46}$$

In the Earth-Moon system, α is equal to 29.7°.

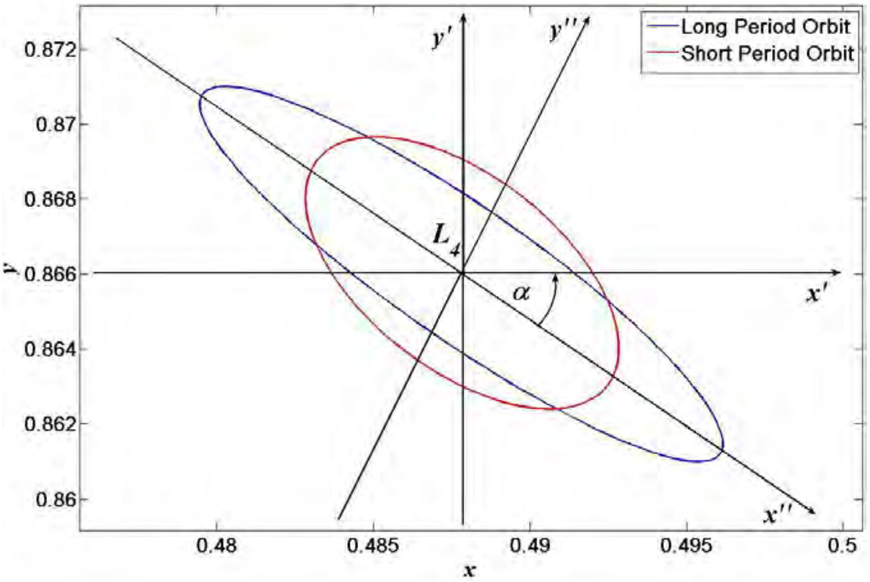

Figure 2.4 - Long and Short Period Orbits about L_4 for the Earth and the Moon system. The principal axes of the elliptic trajectories are oriented according to the angle α

2.6 Equations of Local Dynamics of Satellite Formation Flying

In this section we describe a linear approach to the problem of Formation Flying that gives the relevant information about the local dynamics of the problem.

Let $X = (x, y, \dot{x}, \dot{y})^T$ be the vector that describes the position and velocity of the mass m. Hence the equations of motion in Eqs. (2.17) and (2.18) can be written in vector form as

$$\dot{X} = \boldsymbol{f}(X), \tag{2.47}$$

where

$$\boldsymbol{f} = \begin{pmatrix} \dot{x} \\ \dot{y} \\ 2\dot{y} + \frac{\partial U}{\partial x} \\ -2\dot{x} + \frac{\partial U}{\partial y} \end{pmatrix}. \tag{2.48}$$

Now assume a formation flying such that the chief satellite is placed in a periodic orbit around L_4. Let $X_h(t)$ and $X(t)$ be the vectors corresponding to the trajectories of the chief and deputy satellites, respectively. Therefore the vector $\Delta X(t) = X(t) - X_h(t)$ represents the relative position and velocity vectors of the deputy satellite with respect to the chief satellite at instant t. The coordinates of vector $\Delta X(t)$ are defined in a coordinate system $\hat{x}, \hat{y}$ which is parallel to the rotating coordinate system x, y and is centered at $X_h(t)$ as shown in Fig. 2.5.

Differentiating the vector ΔX with respect to time t, we have

$$\begin{aligned} \Delta\dot{X} &= \dot{X} - \dot{X}_h \\ &= \boldsymbol{f}(X) - \boldsymbol{f}(X_h). \end{aligned} \tag{2.49}$$

Supposing that the radius of the formation flying (largest separation between the spacecrafts) is small, then we can linearize the vector field $\boldsymbol{f}(X)$ around the periodic orbit $X_h(t)$

$$\boldsymbol{f}(X) \approx \boldsymbol{f}(X_h) + D\boldsymbol{f}(X_h)\,\Delta X. \tag{2.50}$$

Substituting this expression in Eq. (2.49), we obtain that the linear behaviour of the deputy satellite around a periodic solution:

$$\Delta\dot{X} = D\boldsymbol{f}(X_h)\,\Delta X, \tag{2.51}$$

where

$$D\boldsymbol{f} = \begin{pmatrix} 0 & 0 & 1 & 0 \\ 0 & 0 & 0 & 1 \\ \frac{\partial^2 U}{\partial x^2} & \frac{\partial^2 U}{\partial y \partial x} & 0 & 2 \\ \frac{\partial^2 U}{\partial x \partial y} & \frac{\partial^2 U}{\partial y^2} & -2 & 0 \end{pmatrix}. \tag{2.52}$$

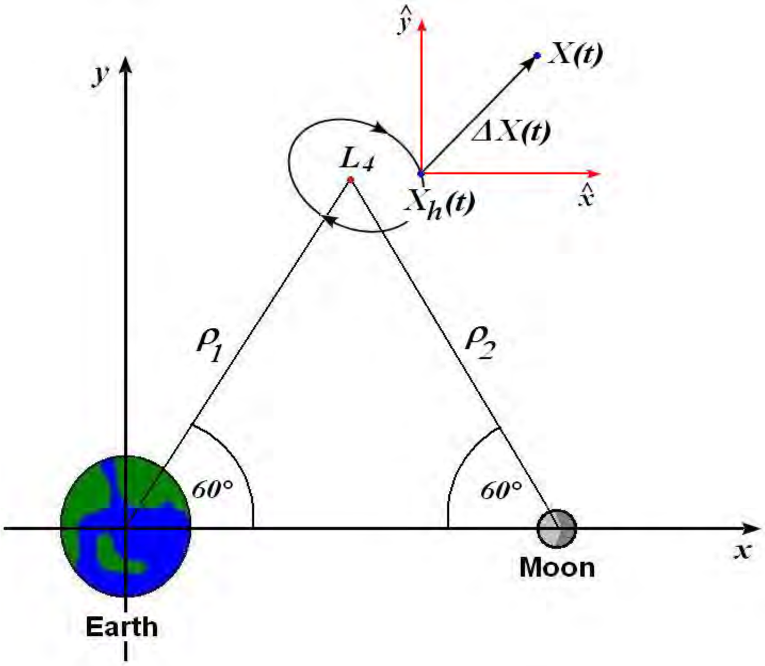

Figure 2.5 - Illustration of a satellite formation flying about L_4. The vectors $X_h(t)$ and $X(t)$ are the corresponding trajectories of the chief and deputy satellites, respectively. Vector $\Delta X(t)$ represents the relative position and velocity of the deputy satellite with respect to the chief satellite at instant t.

2.7 Newton's Method to find Periodic Orbits

In this last section we describe briefly a numerical algorithm to design periodic solutions in the CRTBP.

Let $\phi(t, X_0)$ be the orbit which passes through X_0 at time $t = 0$ and intersects the x-axis at point X_f at time $t = T$ as shown in Fig. 2.6, i.e. $\phi(0, X_0) = X_0$ and $\phi(T, X_0) = X_f$.

A periodic solution must satisfy the following condition

$$\begin{aligned} \phi(t, X^*) &= X^*, \\ \phi(t, X^*) - X^* &= \mathbf{0}. \end{aligned} \tag{2.53}$$

Therefore Eq. (2.53) can be solved using the Newton's method (GAUTSCHI, 1997). Given an initial condition X_0, the sequence

$$X_{n+1} = X_n - \left(\frac{\partial \phi(T, X_n)}{\partial X}\right)^{-1} \left(\phi(T, X_n) - X_f\right), \tag{2.54}$$

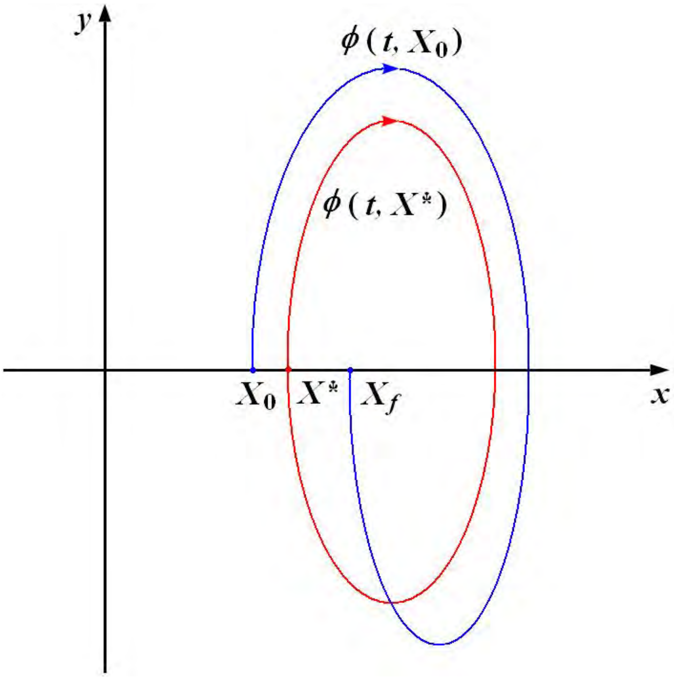

Figure 2.6 - Orbit $\phi(t, X_0)$ passes through X_0 at time $t = 0$ and intersects the x-axis at the point X_f at time $t = T$. Periodic solution $\phi(t, X^*)$ satisfies the condition $\phi(t, X^*) = X^*$.

converges to a solution X^*. The matrix $\Phi(t) = (\partial\phi(t, X_n)/\partial X)$ is called the State Transition Matrix (SCHAUB; JUNKINS, 2003) and satisfy the differential equation (MORRIS; SMALE, 1974)

$$\dot{\Phi} = (D\boldsymbol{f})\,\Phi, \tag{2.55}$$

$$\Phi(0) = I, \tag{2.56}$$

where $D\boldsymbol{f}$ is the derivative of the vector field $\boldsymbol{f}$ in Eq. (2.47) and I is the identity matrix.

In this manner, starting from an initial condition X_0, we find a periodic solution in the CRTBP integrating the system of differential equations (2.47) and

$$\dot{\phi} = \boldsymbol{f}(\phi), \tag{2.57}$$

$$\phi(0) = X_0, \tag{2.58}$$

until the orbit $\phi(T, X_0)$ intersects the x-axis at a time $t = T$ as shown in Fig. 2.6. The vector $\phi(T, X_0)$ and the inverse of matrix $\Phi(T)$ are substituted in Eq. (2.54), and we iterate the Newton's method that converges to a solution X^* for some prescribed tolerance (approx. 10^{-6}). The existence of the inverse of the state transition matrix is guaranteed by the Inverse Function Theorem (LANG, 1997). A good approximation for an initial condition X_0 near X^* can be given by the linear approach in Eq. 2.44.

The procedure described here is sometimes called the method of differential corrections or differential correction procedure (ALLGOVER; GEORG, 1990).

3 TRANSFER ORBITS

In the following sections we will describe the transfer methods used in this work to place a spacecraft in a periodic orbit around the Lagrangian points L_4 and L_5 for the Earth and the Moon system. Essentially, the methods consist in to find the initial conditions such that the trajectory of the spacecraft intersects the semi-major or -minor axes of an elliptic orbit around the equilibrium points and to apply a stabilizing impulsive thrust in order that the spacecraft enters the elliptic trajectory. The initial conditions depends on the set of parameters that determine the first impulse thrust applied to guide the spacecraft to L_4 and L_5.

The first section presents in general the stabilizing impulsive thrust applied on the spacecraft once it intersects the axis of the elliptic orbit. The second section describes the elements of the Hohmann Transfer Orbit used to accomplish our mission. The third section presents the mathematical description of the swing-by maneuver as well as the patched conic approximation such that we will discuss the geometric parameters involved in the transfer orbits. Finally, the third and fourth sections introduce two alternative new techniques to guide spacecrafts to equilibrium points L_4 and L_5: G Trajectories and Chaos. Basically, the difference between these new techniques and the swing-by maneuver is the way the spacecraft leaves the Earth's sphere of influence and enters the lunar sphere of influence. In fact, G Trajectories and Chaos will use the family of periodic orbits around the equilibrium point L_1 and the chaotic region that exists in the Earth-Moon system to achieve our objective, respectively.

3.1 Stabilizing Impulsive Thrust

Suppose that our mission consists in to place a spacecraft in an elliptic orbit centered at triangular equilibrium point L_4 (or L_5) such that the lengths of the semi-major and minor axes are a and b, respectively. Since the principal axes of the ellipse are rotated relative to the coordinate system x', y' by an angle $\alpha = 29.7^\circ$ as shown in Fig. 2.4, the equations of motion around the equilibrium point can be simplified by rotating the coordinate system by 29.7° clockwise about the equilibrium point. The new coordinates, (x'', y''), are given by

$$\begin{pmatrix} x''(t) \\ y''(t) \end{pmatrix} = \begin{pmatrix} \cos 27.9^\circ & -\sin 27.9^\circ \\ \sin 27.9^\circ & \cos 27.9^\circ \end{pmatrix} \begin{pmatrix} x'(t) \\ y'(t) \end{pmatrix}, \tag{3.1}$$

where

$$x'(t) = x(t) - \left(\frac{1}{2} - \mu\right), \quad (3.2)$$

$$y'(t) = y(t) - \frac{\sqrt{3}}{2}, \quad (3.3)$$

and, $x(t)$ and $y(t)$ are the coordinates of the spacecraft in the rotating system.

Given a trajectory with a vector of initial conditions $X(0) = (x_0, y_0, \dot{x}_0, \dot{y}_0)^T$, let us assume that this trajectory intersects the axis x'' at a point $x''(t^*) > 0$ at time $t = t^*$ as shown in Fig. 3.1. Since the trajectory is defined by the vector $X(0)$, then the goal of this work is to find the initial conditions such that

$$x''(t^*) - a = 0. \quad (3.4)$$

Similarly, if the trajectory intersects the axis y'' at a point $y''(t^*) > 0$ at time $t = t^*$, then we must find the initial conditions such that

$$y''(t^*) - b = 0. \quad (3.5)$$

The same idea also works whether $x''(t^*), y''(t^*) < 0$.

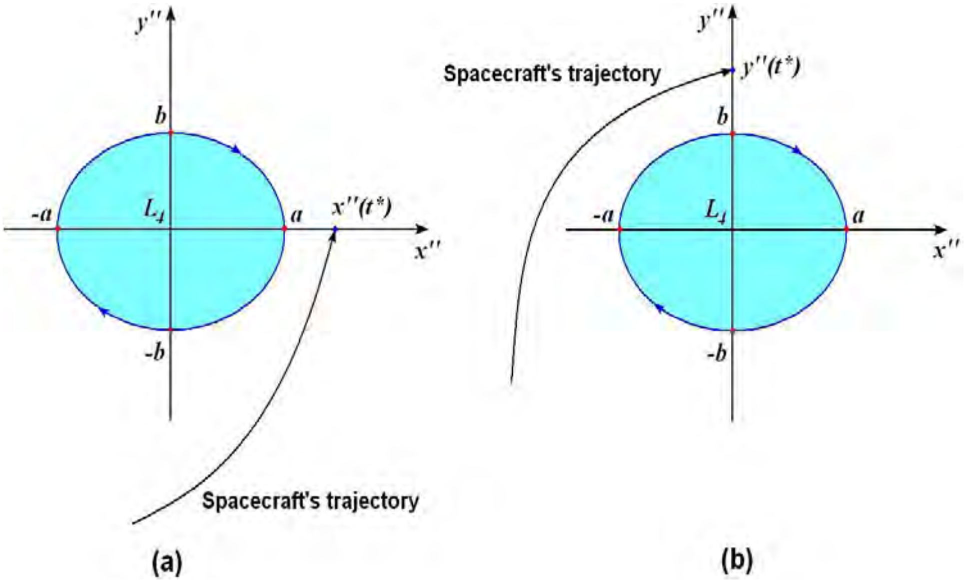

Figure 3.1 - Illustration of the spacecraft's trajectory intersecting the perpendicular axes x'', y''.

Now denote by $\boldsymbol{v_a}$ and $\boldsymbol{v_a^*}$ the velocities with respect to coordinate system x'', y'' at the point $(a, 0)$ of the elliptic orbit and the spacecraft, respectively, as shown in Fig. 3.2. Therefore the change in velocity $\Delta\boldsymbol{v_2}$ of the stabilizing impulsive thrust to enter the elliptic orbit is given by

$$\Delta\boldsymbol{v_2} = \boldsymbol{v_a} - \boldsymbol{v_a^*}. \tag{3.6}$$

Similarly if we denote by $\boldsymbol{v_b}$ and $\boldsymbol{v_b^*}$ the velocities at the point $(0, b)$ of the elliptic orbit and the spacecraft, respectively, as shown in Fig. 3.2, the change in velocity $\Delta\boldsymbol{v_2}$ of the stabilizing impulsive thrust to enter the elliptic orbit is given by

$$\Delta\boldsymbol{v_2} = \boldsymbol{v_b} - \boldsymbol{v_b^*}. \tag{3.7}$$

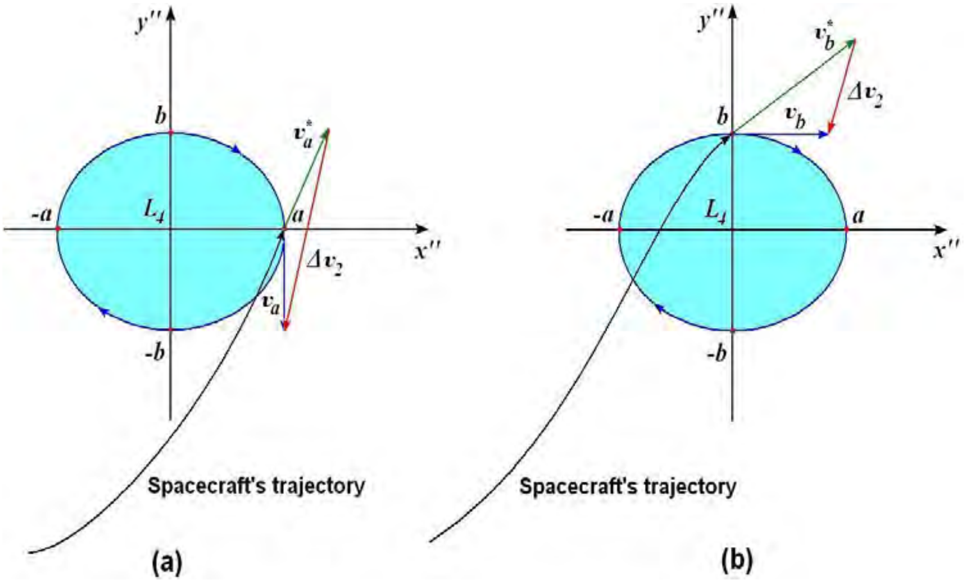

Figure 3.2 - Illustration of the stabilizing impulsive thrust applied to enter the elliptic orbit around L_4 when the spacecraft intersects (a) the semi-major axis and (b) the semi-minor axis.

3.2 Modified Hohmann Transfer Orbit

Consider an Earth-centered inertial coordinate system $\hat{\boldsymbol{n}}_{\boldsymbol{1}}, \hat{\boldsymbol{n}}_{\boldsymbol{2}}$ and suppose a spacecraft in a circular orbit of radius r_0 around the Earth such that the inertial axes are aligned with the rotating coordinate system at time $t = 0$ as shown in Fig. 3.3.

Therefore the angle between the axis $\hat{\boldsymbol{n}}_{\mathbf{1}}$ and L_4 (or L_5) is 60° ($\pi/3$ radians) at that instant. In the dimensional system of units, the mean motion of the equilibrium points L_4 and L_5 is $\omega = 2.66525 \times 10^{-6}$ rad/s (see Sect. 2.1) with respect to the inertial frame.

As we can see in Fig. 3.3, the geometry of any spacecraft's trajectory is given by the the velocity at departure $\boldsymbol{v}_{\mathbf{0}}$ and the phase angle γ_0 of departure. Therefore our goal is to find $\boldsymbol{v}_{\mathbf{0}}$ and γ_0 to place the spacecraft in a periodic orbit around the triangular equilibrium points. This problem can be simplified if we neglect the effects of the lunar gravity (this approximation is called 'Patched Conic' and will be explained with more details in the next section). Thus, the problem becomes in a two-body problem and we are interested in determine a suitable transfer orbit that will connect the corresponding position vector $\boldsymbol{r}_{\mathbf{0}}$ with the orbit of L_4 and L_5. Remember that with respect to the inertial frame, the resulting motion of L_4 and L_5 is a circular orbit about the Earth.

Now note that this problem is essentially the minimum energy transfer orbit described in Sect.1.2.1 where for the spacecraft to leave its circular orbit of radius r_0 and enter the elliptic orbit of semi-major axis of $a_m = (r_0 + d)/2$, a tangential change in velocity $\Delta\boldsymbol{v}_{\mathbf{1}}$ is required

$$\Delta v_1 = v_i \left(\sqrt{\frac{2d}{r_0 + d}} - 1 \right). \tag{3.8}$$

where $v_i = \sqrt{\mu_E / r_0}$. Therefore the magnitude of the velocity at departure v_0 is

$$v_0 = v_i \left(\sqrt{\frac{2d}{r_0 + d}} \right). \tag{3.9}$$

The phase angle γ_0 can be computed once the time of of flight Δt is determined. The time of transfer follows from the Kepler's equation (SCHAUB; JUNKINS, 2003):

$$\Delta t = \pi \sqrt{\frac{a_m^3}{\mu_E}}. \tag{3.10}$$

The points L_4 and L_5 move through an angle $\omega \Delta t$ between the injection and arrival at the periodic orbit about them. Hence the phase angles at departure for L_4 and

L_5 missions, are then determined from

$$\gamma_0 = \pi - \left(\omega \Delta t + \frac{\pi}{3}\right), \tag{3.11}$$

$$\gamma_0 = \pi - \left(\omega \Delta t - \frac{\pi}{3}\right), \tag{3.12}$$

respectively.

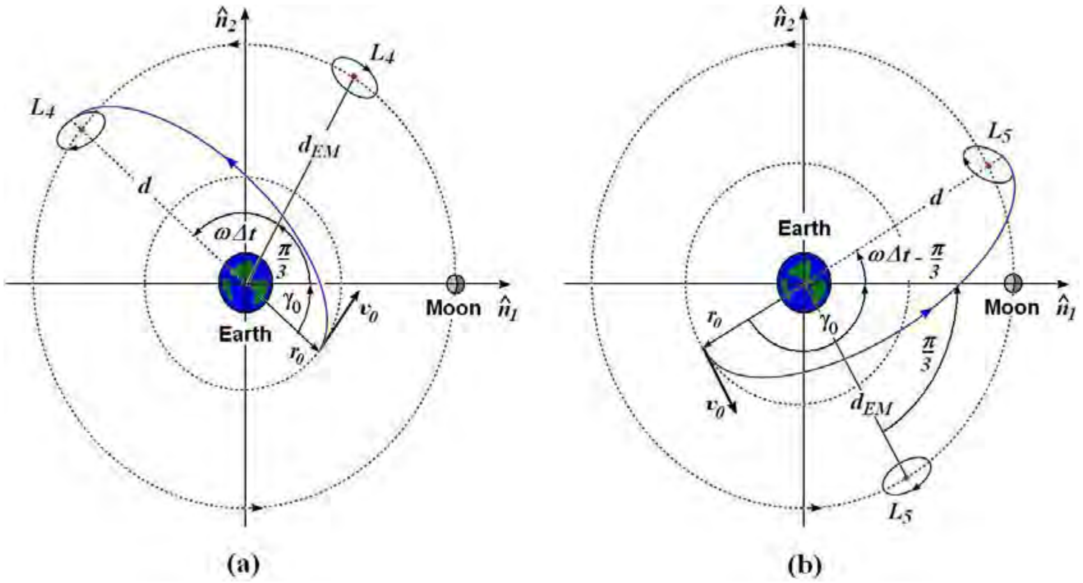
$\hat{n}_2$
L_4
L_4
d_{EM}
d
$\omega\Delta t$
$\frac{\pi}{3}$
γ_0
v_0
Moon
$\hat{n}_1$
Earth
r_0
(a)
$\hat{n}_2$
L_5
Earth
d
$\omega\Delta t - \frac{\pi}{3}$
r_0
γ_0
$\frac{\pi}{3}$
Moon
$\hat{n}_1$
v_0
d_{EM}
L_5
(b)

Figure 3.3 - Illustration of the minimum energy transfer orbit to periodic orbits around (a) L_4 and (b) L_5.

As we can see in Fig. 3.3, the position and velocity vectors $\boldsymbol{r_0}$, $\boldsymbol{v_0}$ at the injection point for L_4 and L_5 missions are expressed with respect to the inertial frame components as

$$\boldsymbol{r_0} = r_0 \cos\gamma_0 \boldsymbol{\hat{n}_1} - r_0 \sin\gamma_0 \boldsymbol{\hat{n}_2}, \tag{3.13}$$

$$\boldsymbol{v_0} = v_0 \sin\gamma_0 \boldsymbol{\hat{n}_1} + v_0 \cos\gamma_0 \boldsymbol{\hat{n}_2}. \tag{3.14}$$

The coordinates of the Earth in the non-dimensional rotating system are $(-\mu, 0)$. Because in the system of units that we have chosen, the non-dimensional synodic frame system is rotating at a uniform unitary rate, therefore, using the Transport Theorem (SCHAUB; JUNKINS, 2003) in Eqs. (3.13) and (3.14), the non-dimensional coordinates of the position vector $\boldsymbol{r_0} = (x_0, y_0)^T$ and velocity vector $\boldsymbol{v_0} = (\dot{x}_0, \dot{y}_0)^T$

with respect to the rotating coordinate system are

$$\begin{aligned} x_0 &= \frac{r_0 \cos\gamma_0}{d_{EM}} - \mu, & (3.15)\\ y_0 &= -\frac{r_0 \sin\gamma_0}{d_{EM}}, & (3.16)\\ \dot{x}_0 &= \frac{v_0 \sin\gamma_0}{\omega d_{EM}} + y_0, & (3.17)\\ \dot{y}_0 &= \frac{v_0 \cos\gamma_0}{\omega d_{EM}} - x_0 - \mu. & (3.18) \end{aligned}$$

Finally, from Eqs. (3.9) and (3.10), the velocity and phase angle at departure depends on the radius r_0 and the apocentre d. As the initial radius is fixed, the only independent variable is the apocentre. Therefore, the goal consists in to find the value of d such that Eq. (3.4) or (3.5) is satisfied. In other words, to find a zero of a function. Because the continuity of the system of differential equations (2.47), Equations (3.4) and (3.5) can be solved quickly using the Newton-secant method. Since the periodic orbits are close to equilibrium points, then $d \approx d_{EM}$. Once the spacecraft intersects the elliptic orbit, the stabilizing impulsive thrust $\boldsymbol{\Delta v_2}$ is required to place the spacecraft into the periodic orbit as shown in Fig. 3.2.

The total cost Δv_T of the transfer is computed by

$$\Delta v_T = \Delta v_1 + \Delta v_2. \qquad (3.19)$$

3.3 Using the gravitational field of the Moon

In the previous section, the lunar gravity was neglected to transfer the spacecraft from a circular parking orbit around the Earth to a periodic orbit about the equilateral equilibrium points. Now, we will use a gravity assist maneuver with the Moon to transfer the spacecraft. For this purpose, we will use the ‘patched conic’ approximation, separating the Earth-Moon-spacecraft problem in two problems of two bodies: Earth-spacecraft and Moon-spacecraft. While the spacecraft is outside the gravitational sphere of influence of the Moon, the trajectory is approximated by taking only the terrestrial gravity into account and using the two-body orbital mechanics. Similarly, once the spacecraft enters the Moon’s sphere of influence, we will assume that the spacecraft moves only under the gravitational influence of the Moon. Depending on the speed and the direction of the spacecraft relative to the center of the Moon, it is possible to change the energy of the spacecraft relative to the Earth and guide it to the Lagrangian points L_4 and L_5. The key point using this approach is to determine the geometry of the geocentric departure orbit such that the spacecraft can be placed around L_4 and L_5.

In order to look for trajectories like that, a first simplifying assumption is to consider only the gravitational attraction force of the Earth as long as the spacecraft is around it and receives the first impulsive to enter into an elliptic transfer orbit. While the trajectory does not cross the gravitational sphere of influence of the Moon, the two-body orbital scenario is considered. One of the advantages of this approach is that the solution of the two-body problem is analytical (BATTIN, 1987). Additionally, the Moon's orbit will be assumed as circular with radius of d_{EM} and angular velocity ω_M (see Appendix).

Now, a second assumption is made when the spacecraft crosses the Moon's sphere of influence. In that instant, the spacecraft will be regard as moving only under the gravitational influence of the Moon. Similarly, a second problem of two bodies has to be analyzed. To express the sphere of influence concept in mathematical terms we rewrite the equations of motion of the spacecraft in Eqs. (2.1) and (2.2). Let $\boldsymbol{R_E}$ and $\boldsymbol{R_M}$ be the position vectors of the spacecraft relative to the Earth and Moon, respectively. Similarly, the position vector from the Moon to the Earth is denoted by $\boldsymbol{R_{EM}}$, as illustrated in Fig. 3.4. The equation of motions of the spacecraft relative to either the Earth or Moon are given by

$$\begin{aligned}
\ddot{\boldsymbol{R}}_{\boldsymbol{E}} &= \underbrace{-\frac{Gm_E}{R_E^3}\boldsymbol{R_E}}_{\boldsymbol{a_E}} \underbrace{- Gm_M\left(\frac{\boldsymbol{R_M}}{R_M^3} + \frac{\boldsymbol{R_{EM}}}{R_{EM}^3}\right)}_{\boldsymbol{a_{d_E}}}, \\
\ddot{\boldsymbol{R}}_{\boldsymbol{M}} &= \underbrace{-\frac{Gm_M}{R_M^3}\boldsymbol{R_M}}_{\boldsymbol{a_M}} \underbrace{- Gm_E\left(\frac{\boldsymbol{R_E}}{R_E^3} - \frac{\boldsymbol{R_{EM}}}{R_{EM}^3}\right)}_{\boldsymbol{a_{d_M}}}.
\end{aligned}$$

In this case, the gravitational attraction of the other celestial body is expressed as a disturbance acceleration $\boldsymbol{a_{d_E}}$ on the two-body solution about the Earth and $\boldsymbol{a_{d_M}}$ on the two-body solution about the Moon. The lunar sphere of influence is the region around the Moon where the magnitude of the disturbance acceleration vector $\boldsymbol{a_{d_M}}$ is equal to the magnitude of the two-body acceleration vector $\boldsymbol{a_M}$. Since the mass of the Earth is greater than the mass of the Moon (almost 82 times greater), the radius R_S of the gravitational sphere of influence of the Moon is approximately (BATTIN, 1987):

$$R_S = d_{EM}\left(\frac{m_M}{m_E}\right)^{2/5}. \tag{3.20}$$

Substituting the values of d_{EM}, m_E and m_M (see Appendix) in Eq. (3.20) yields the value

$$R_S = 66,181 \text{ km},$$

or about 1/6 the Earth-Moon distance.

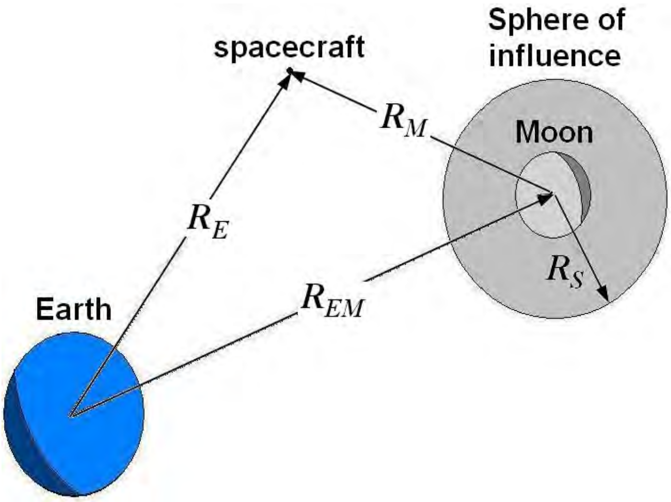

Figure 3.4 - Illustration of the sphere of influence concept in the Earth-Moon system. The radius R_S of the lunar sphere of influence is about 1/6 the distance from Earth to the Moon.

3.3.1 The Mathematical Description of the Swing-By

Figure 3.5 illustrates the geometry of the geocentric departure orbit. Originally, the spacecraft is in a parking circular orbit of radius r_0 around the Earth. The four quantities that determine totally the geometry of the departure orbit are

$$r_0, v_0, \phi_0, \lambda_0, \tag{3.21}$$

where v_0 and ϕ_0 are the velocity and angle at departure, and λ_0 is the angle that specifies the point at which the geocentric trajectory intersects the lunar sphere of influence. Another important quantity shown in Fig. 3.5 is the phase angle of departure γ_0 which can be easily determined once the four quantities are known. As we can saw in the previous section, this angle is necessary to determine the initial conditions of the departure in the rotating frame. Additionally, since we are interested in minimum energy trajectories to reach the Moon's sphere of influence, the angle at departure $\phi_0 = 0$ in all trajectories.

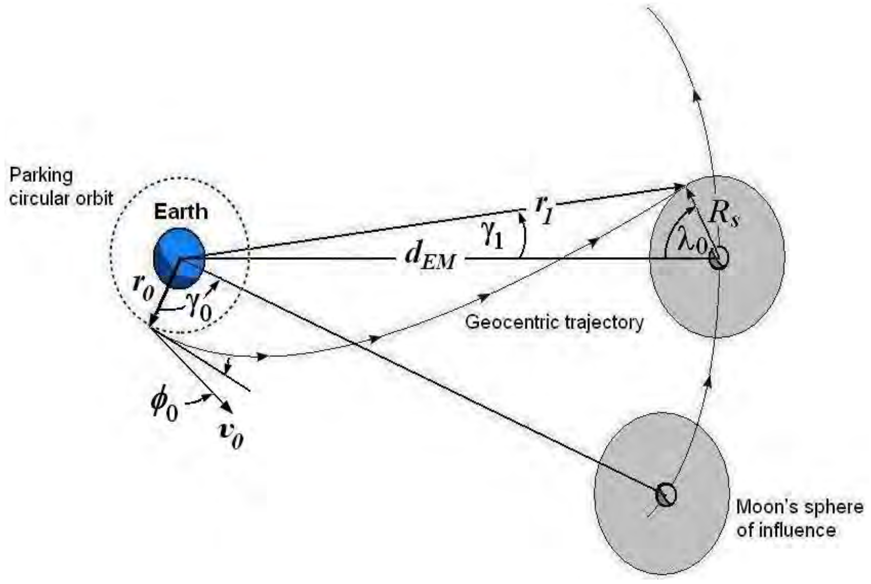
Parking
circular orbit
Earth
r_0
γ_0
ϕ_0
v_0
r_1
γ_1
d_{EM}
R_s
λ_0
Geocentric trajectory
Moon's sphere
of influence

Figure 3.5 - Illustration of the geocentric departure orbit.

3.3.1.1 The Geocentric Departure Orbit

The geometry of the departure begins computing the radius r_1 and angle γ_1 by using the law of cosines and sines in the triangle defined by the radius R_S and d_{EM}:

$$r_1 = \sqrt{d_{EM}^2 + R_S^2 - 2 d_{EM} R_S \cos \lambda_0}, \tag{3.22}$$

$$\gamma_1 = \sin^{-1}\left(\frac{R_S}{r_1}\sin \lambda_0\right). \tag{3.23}$$

Similarly, the energy ε_E and angular momentum h_E of the spacecraft relative to the center of the Earth can be computed from the departure conditions (3.21):

$$\varepsilon_E = \frac{v_0^2}{2} - \frac{\mu_E}{r_0}, \tag{3.24}$$

$$h_E = r_0 v_0. \tag{3.25}$$

Finally, from the conservation of energy and angular momentum, the geocentric speed v_1 and the flight path angle ϕ_1 at arrival (see Fig. 3.6) are given by

$$v_1 = \sqrt{2\left(\varepsilon_E + \frac{\mu_E}{r_1}\right)}, \tag{3.26}$$

$$\phi_0 = \cos^{-1}\frac{h_E}{r_1 v_1}. \tag{3.27}$$

3.3.1.2 The Selenocentric Arrival Orbit

Once the spacecraft enters the lunar sphere of influence, the velocity vector with respect to the Moon is determined by

$$\boldsymbol{v_1} = \boldsymbol{v_2} - \boldsymbol{v_M}, \tag{3.28}$$

where $\boldsymbol{v_M}$ is the velocity vector of the Moon with respect to the center of the Earth (see Fig. 3.6). Based on our simplified model of the Earth-Moon system, the orbital speed of the Moon is

$$\begin{aligned} v_M &= \omega_M d_{EM}, \\ &= 1.0183 \quad \frac{\text{km}}{\text{s}}. \end{aligned} \tag{3.29}$$

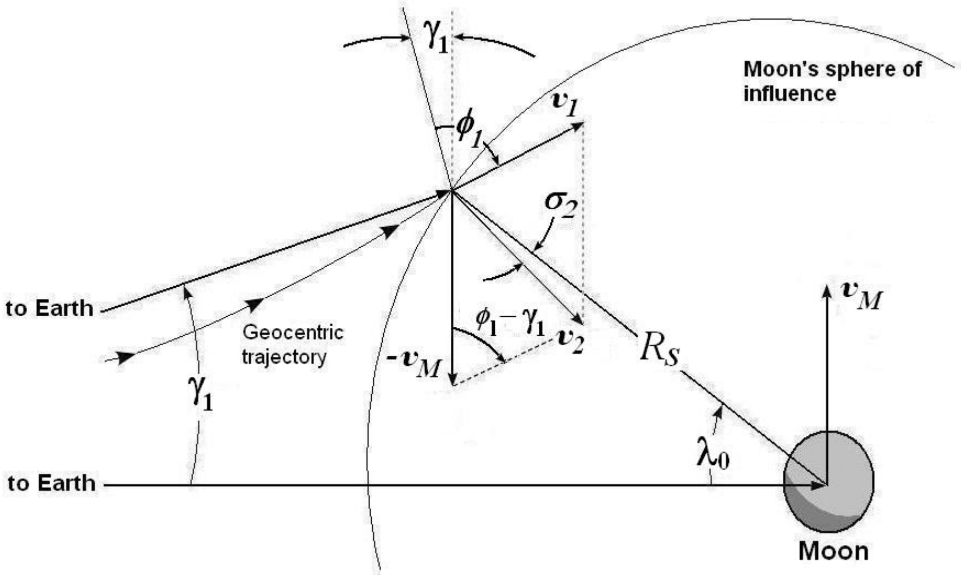

γ_1
Moon's sphere of influence
$\boldsymbol{v_1}$
ϕ_1
σ_2
to Earth
Geocentric trajectory
$\phi_1-\gamma_1$
$\boldsymbol{v_2}$
$-\boldsymbol{v}_M$
R_S
$\boldsymbol{v}_M$
γ_1
λ_0
to Earth
Moon

Figure 3.6 - Illustration of the selenocentric arrival orbit.

Similarly, applying the law of cosines to the vectorial triangle between the velocity vectors $\boldsymbol{v_1}$ and $-\boldsymbol{v_M}$, the selenocentric arrival speed v_2 is given by

$$v_2 = \sqrt{v_1^2 + v_M^2 - 2v_1 v_M \cos\left(\phi_1 - \gamma_1\right)}. \tag{3.30}$$

The angle σ_2 defines the direction of the arrival velocity vector $\boldsymbol{v_2}$ relative to the Moon's center, and can be determined from (BATE et al., 1971)

$$\sigma_2 = \sin^{-1}\left(\frac{v_M}{v_2}\cos\lambda_0 - \frac{v_1}{v_2}\cos\left(\lambda_0 + \gamma_1 - \phi_1\right)\right). \tag{3.31}$$

In this way, if the arrival conditions R_S , v_2 and σ_2 are known, therefore the periselene radius r_p and speed v_p of the spacecraft can be easily computed. Firstly, the energy ε_M and angular momentum h_M of the spacecraft relative to the Moon are determined from the arrival conditions (3.30) and (3.31):

$$\varepsilon_M = \frac{v_2^2}{2} - \frac{\mu_M}{R_S}, \tag{3.32}$$

$$h_M = v_2 R_S \sin\sigma_2, \tag{3.33}$$

where μ_M is the Moon gravitational constant (see Appendix).

Now that these two quantities are know, the semilatus rectum p_M and eccentricity e_M of the selenocentric arrival orbit can be expressed in terms of energy and angular momentum, respectively:

$$p_M = \frac{h_M^2}{\mu_M}, \tag{3.34}$$

$$e_M = \sqrt{1 + \frac{2\varepsilon_M h_M^2}{\mu_M^2}}. \tag{3.35}$$

From the polar equation of conics and the conservation of energy follows that

$$r_p = \frac{p_M}{1 + e_M}, \tag{3.36}$$

$$v_p = \sqrt{2\left(\varepsilon_M + \frac{\mu_M}{r_p}\right)}. \tag{3.37}$$

It is important to note that the periselene radius can not be less than the radius of the Moon (see Fig. 3.7), otherwise, the spacecraft will impact the Moon.

3.3.1.3 Swing-By Maneuver

When the spacecraft makes a close approach with the Moon, this close approach changes the trajectory of the spacecraft. Figure 3.7 shows this event and the variables involved.

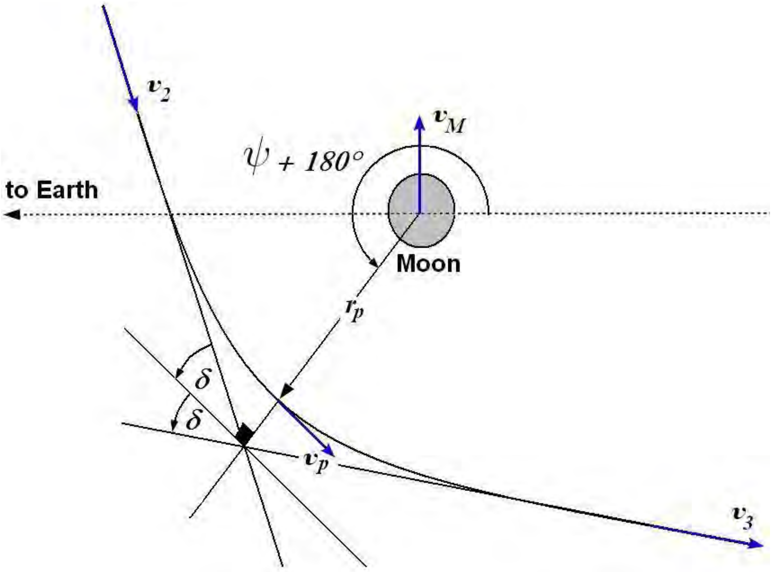

Figure 3.7 - The Swing-by Maneuver with the Moon.

The vector $\boldsymbol{v_3}$ represents the velocity vector of the spacecraft with respect to the Moon when it leaves the lunar sphere of influence and ψ, the angle between the periselene and the line that connects the Earth with the Moon, is called the angle of approach. Under the hypothesis of the patched-conic model, the orbit of the Earth and Moon are not changed by this close approach.

Assuming that the approach trajectory is a hyperbolic orbit, the relative velocity $\boldsymbol{v_2}$ rotates by an angle 2δ when the spacecraft crosses again the lunar sphere of influence as shown in Fig. 3.7. At that moment, the relative velocity $\boldsymbol{v_3}$ will have the same magnitude as the arrival velocity $\boldsymbol{v_2}$. The angle δ can be determined through the expression for the hyperbolic asymptote angle (SCHAUB; JUNKINS, 2003) and the eccentricity of the selenocentric arrival orbit (3.35):

$$\delta = \sin^{-1}\frac{1}{e_M}. \tag{3.38}$$

After the spacecraft leaves the lunar sphere of influence, it returns to a new Keplerian orbit around the Earth and the swing-by maneuver is complete. The differences between the orbits before and after this close encounter will determine the trajectory that intersects the periodic orbit around L_4 or L_5.

The first important quantity that has to be computed is the difference $\boldsymbol{\Delta v}$ between the velocities with respect to the Earth before and after the swing-by. Assuming that the close approach is instantaneous, then the vector velocity of the Moon with respect to the Earth remains practically constant. Therefore,

$$\begin{aligned}\boldsymbol{\Delta v} &= (\boldsymbol{v_2} + \boldsymbol{v_M}) - (\boldsymbol{v_3} + \boldsymbol{v_M}), \\ &= \boldsymbol{v_2} - \boldsymbol{v_3}. \end{aligned} \tag{3.39}$$

Now, from Fig. 3.7 we can get a vector diagram as shown in Fig. 3.8. This diagram shows that the magnitude of the vector difference $\boldsymbol{\Delta v}$ is equal to

$$\Delta v = 2v_2 \sin\delta, \tag{3.40}$$

and that this vector makes an angle ψ with the line that connects the Earth with the Moon. This fact gives us the components Δv_x and Δv_y for the increment in velocity $\boldsymbol{\Delta v}$:

$$\Delta v_x = 2v_2 \sin\delta \cos\psi, \tag{3.41}$$

$$\Delta v_y = 2v_2 \sin\delta \sin\psi. \tag{3.42}$$

In this way, the second important quantity that has to be derived is the change in energy $\Delta\varepsilon$. Since the close approach is instantaneous, the potential energy does not change before and after the encounter, however the kinetic energy does. Therefore, the change in energy can be computed subtracting the kinetic energy ε^+ after the encounter and the kinetic energy ε^- before. So, let us denote by

$$\boldsymbol{v_1} = \begin{pmatrix} v_1^x \\ v_1^y \end{pmatrix}, \tag{3.43}$$

the coordinates of the geocentric velocity vector $\boldsymbol{v_1}$ just before the encounter (see Fig. 3.6). Then, the coordinates of the geocentric velocity vector after the encounter

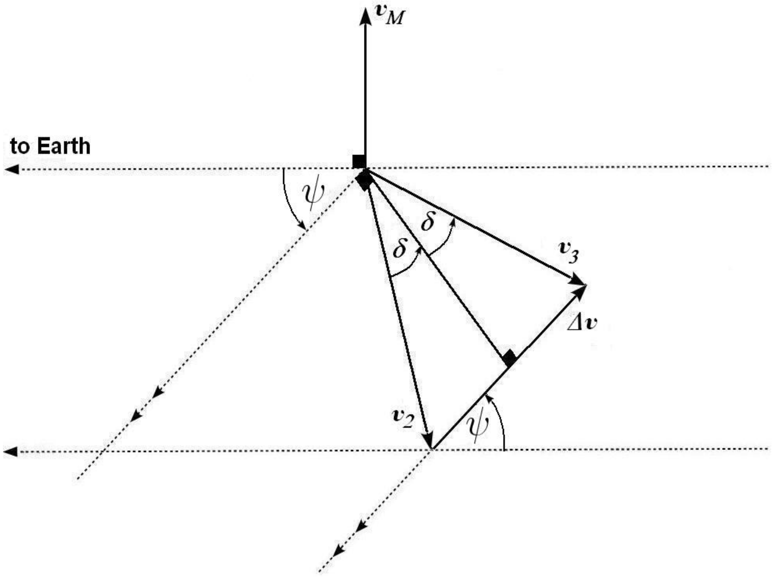

Figure 3.8 - Velocity vectors involved in a swing-by maneuver with the Moon.

are

$$\boldsymbol{v_1} + \Delta\boldsymbol{v} \;=\; \begin{pmatrix} v_1^x + \Delta v_x \\ v_1^y + \Delta v_y \end{pmatrix}. \tag{3.44}$$

Thus the result is

$$\begin{aligned} \Delta\varepsilon &= \varepsilon^+ - \varepsilon^-, \\ &= \frac{1}{2}\left((v_1^x + \Delta v_x)^2 + (v_1^y + \Delta v_y)^2\right) - \frac{1}{2}\left((v_1^x)^2 + (v_1^y)^2\right), \\ &= v_1^x \Delta v_x + v_1^y \Delta v_y + \frac{1}{2}\left((\Delta v_x)^2 + (\Delta v_y)^2\right). \end{aligned} \tag{3.45}$$

The point is therefore to determine the coordinates of vector velocity $\boldsymbol{v_1}$.

Firstly, Figure 3.9 shows the vector diagram obtained by the vector addition $\boldsymbol{v_1} = \boldsymbol{v_2} + \boldsymbol{v_M}$. In this case, the angle β can be computed applying the law of cosines to the vectorial triangle between the velocity vectors $\boldsymbol{v_1}$, $\boldsymbol{v_2}$ and $\boldsymbol{v_M}$:

$$\beta \;=\; \cos^{-1}\frac{v_2^2 + v_M^2 - v_1^2}{2 v_2 v_M}. \tag{3.46}$$

Now, since the angle between the vector velocity $\boldsymbol{v_2}$ and the vertical line is equal to

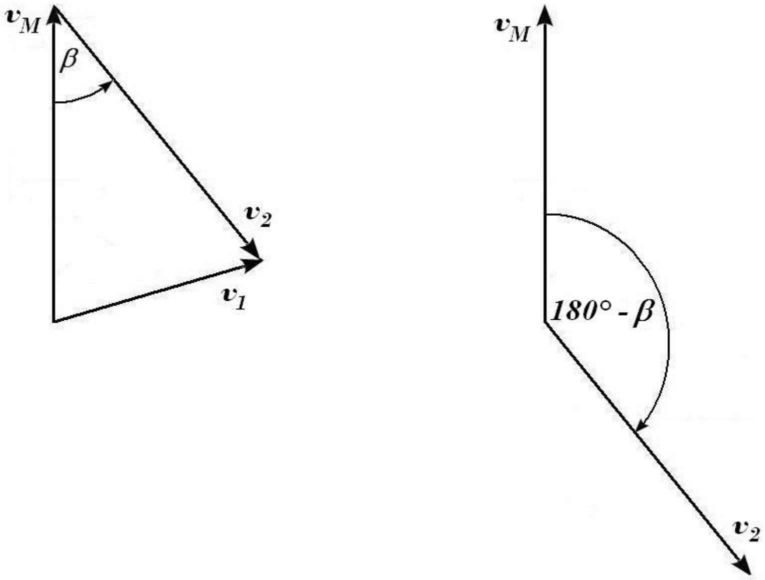

Figure 3.9 - Vector diagram describing the vectorial sum $\boldsymbol{v_1} = \boldsymbol{v_2} + \boldsymbol{v_M}$.

β then coordinates of vector velocity $\boldsymbol{v_1}$ are equal to:

$$\begin{aligned}
\boldsymbol{v_1} &= \boldsymbol{v_2} + \boldsymbol{v_M}, \\
&= \begin{pmatrix} v_2 \sin\beta \\ -v_2 \cos\beta \end{pmatrix} + \begin{pmatrix} 0 \\ v_M \end{pmatrix}, \\
&= \begin{pmatrix} v_2 \sin\beta \\ v_M - v_2 \cos\beta \end{pmatrix}. \qquad (3.47)
\end{aligned}$$

In other words

$$v_1^x = v_2 \sin\beta, \qquad (3.48)$$

$$v_1^y = v_M - v_2 \cos\beta. \qquad (3.49)$$

Substituting the velocity components (3.41)-(3.42) and (3.48)-(3.49) in Eq. (3.45), this leads to

$$\Delta\varepsilon = 2v_2 \sin\delta \left(v_2 \sin\delta - v_2 \sin\left(\psi - \beta\right) + v_M \sin\psi\right). \qquad (3.50)$$

Finally, to determine the changes in velocity and energy, it is necessary to compute the value of the angle of approach ψ. Thus, using the vector diagrams described in

Figs. 3.8 and 3.9, we find (see Fig. 3.10)

$$\psi \quad = \quad \delta + \beta. \tag{3.51}$$

Therefore, the $\Delta\varepsilon$ expression can be simplified to:

$$\Delta\varepsilon \quad = \quad \Delta v \left(v_M \sin\psi \right). \tag{3.52}$$

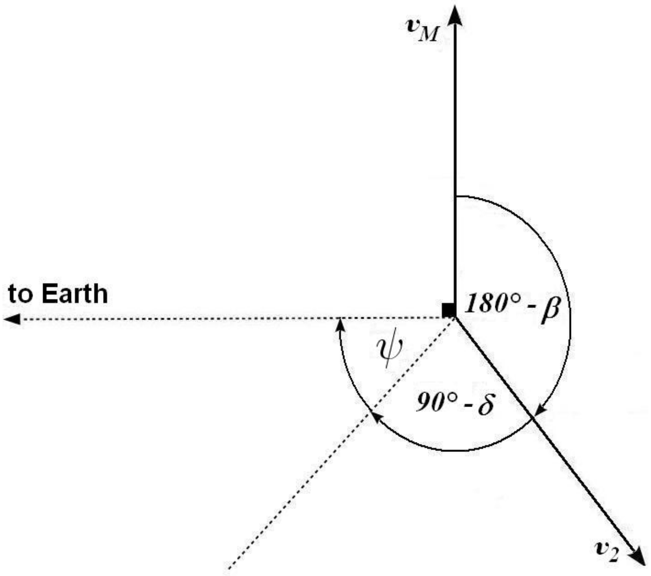

Figure 3.10 - Geometric relation between angles δ, β, and ψ.

3.3.2 Initial Conditions

Considering a spacecraft in an Earth circular parking of radius r_0, we use a minimum energy transfer orbit so that the spacecraft leaves its circular orbit, enters an elliptic orbit of semi-major axis of $a_m = (r_0 + d)/2$ and crosses the Moon's sphere of influence as shown in Fig. 3.11. Therefore, assuming no lunar gravity, the magnitude of the tangential change in velocity $\boldsymbol{\Delta v_1}$ and the injection speed v_0 are given by Eqs. (3.8) and (3.9), respectively. The tangential change in velocity implies that $\phi_0 = 0$.

In this way, once the radius r_0 of the circular parking orbit and the apocentre d of the elliptic transfer orbit are fixed, the minimum energy transfer give us automatically three of the four parameters that describe the geometry of the departure orbit: r_0,

v_0, ϕ_0. The fourth parameter λ_0 remains as independent variable.

Let us suppose that the radius r_0 and the apocentre d are given; the angle λ_0 specifies the point at which the geocentric trajectory will cross the lunar sphere of influence, and the swing-by maneuver will generate different trajectories for different values of λ_0. In this case, as we could see in Sect. 3.3.1, all the parameters involved in the patched-conic approximation and swing-by maneuver can be easily determined for each trajectory. Once the geometry of the departure orbit is known, the non-dimensional initial conditions $\boldsymbol{r_0} = (x_0, y_0)^T$ and $\boldsymbol{v_0} = (\dot{x}_0, \dot{y}_0)^T$ at the injection point which determine the space's trajectory in the rotating coordinate system, can also be computed.

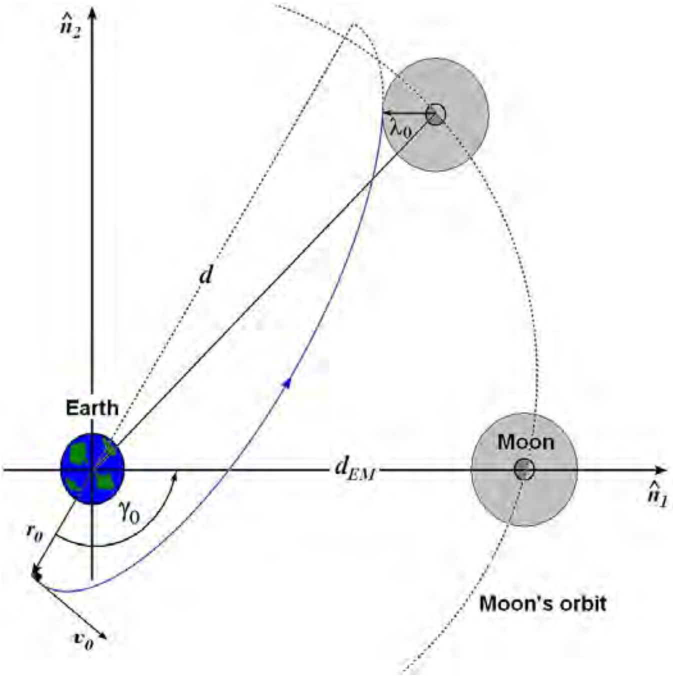

Figure 3.11 - Illustration of a minimum energy transfer orbit of semi-major axis of $a_m = (r_0 + d)/2$ to cross the lunar sphere of influence.

Firstly, suppose similarly that the Earth-centered inertial coordinate system $\boldsymbol{\hat{n}_1}, \boldsymbol{\hat{n}_2}$ are aligned with the rotating coordinate system at time $t = 0$ as shown in Fig. 3.11. Therefore, the initial conditions can be found whether we know the phase angle at departure γ_0 as we could see in Sect. 3.2.

In this manner, let us denote by f_1 and Δt the angle and time of flight of the spacecraft between injection and arrival at the lunar sphere of influence. Based on our simplified model, the Moon moves through an angle $\omega_M \Delta t$ between these two events. Figure 3.12 shows how these angles: γ_0, f_1, $\omega_M \Delta t$, are related. Therefore, if we determine the angle f_1 and the time Δt, the value of the angle at departure γ_0 will be easily computed.

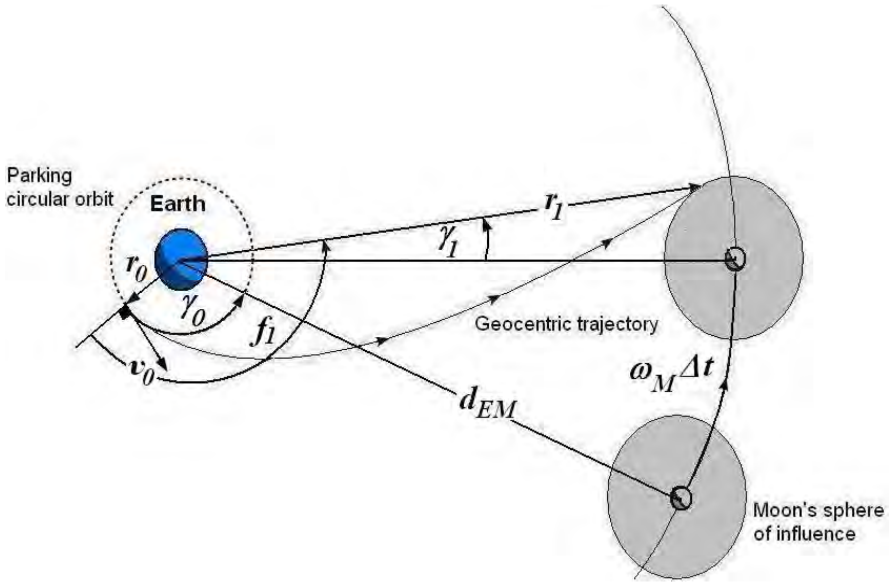
Parking
circular orbit
Earth
r_0
γ_0
v_0
f_1
r_1
γ_1
Geocentric trajectory
$\omega_M \Delta t$
d_{EM}
Moon's sphere
of influence

Figure 3.12 - The spacecraft and Moon move through an angle f_1 and $\omega_M \Delta t$, respectively, between injection and arrival at the lunar sphere of influence.

Now, to find the value of f_1 and Δt, we must determine the semilatus rectum p_E and eccentricity e_E of the geocentric departure orbit. Thus, from the energy and angular momentum of the departure orbit computed in Eqs. (3.24) and (3.25), we have

$$p_E = \frac{h_E}{\mu_E}, \tag{3.53}$$

$$e_E = \sqrt{1 + \frac{2\varepsilon_E h_E^2}{\mu_E^2}}. \tag{3.54}$$

Then f_1 follows from the polar equation of conic:

$$f_1 = \cos^{-1} \frac{p_E - r_1}{r_1 e_E}. \tag{3.55}$$

Next, the eccentric anomaly E_1 can be determined from

$$E_1 = \cos^{-1} \frac{e_E + \cos f_1}{1 + e_E \cos f_1}. \tag{3.56}$$

Finally, the time of flight Δt is obtained from

$$\Delta t = (E_1 - e_E \sin E_1) \sqrt{\frac{a_m^3}{\mu_E}}. \tag{3.57}$$

Therefore, the phase angle at departure γ_0 is determined from Fig. 3.12:

$$\gamma_0 = f_1 - \gamma_1 - \omega_M \Delta t. \tag{3.58}$$

Once the angle at departure γ_0 is known, the non-dimensional initial conditions $(x_0, y_0, \dot{x}_0, \dot{y}_0)^T$ follow from Eqs. (3.15)-(3.18). Thus, once the radius r_0 and the apocentre d are fixed, the goal is to find the angle λ_0 that solves Eq. (3.4) or (3.5). Similarly, when the spacecraft intersects the elliptic orbit around L_4 or L_5, a stabilizing impulsive thrust $\Delta \boldsymbol{v_2}$ is required to place the spacecraft into the periodic orbit. The total cost Δv_T of the transfer is computed by Eq. (3.19).

3.4 G Trajectories for L_4 and L_5

The dynamics of the CRTBP predicts the existence of periodic orbits around the Lagrangian equilibrium points (BROUCKE, 1968). We are interested in the family of periodic orbits around the L_1 point.

In general, the initial conditions in the system of differential equations (2.47) that allow finding periodic orbits of G Family have the following form

$$(x_0, y_0, \dot{x}_0, \dot{y}_0) = (x_0, 0, 0, \dot{y}_0), \tag{3.59}$$

where $(-\mu + r_E/d_{EM}) < x_0 < x_{L_1}$, r_E is the average radius of the Earth (see Appendix) and x_{L_1} is the abscissa of the Lagrangian equilibrium point L_1 in the non-dimensional synodic frame (see Table 2.1). Note that Eq. 3.59 implies that the necessary condition to put a spacecraft into a periodic orbit of G Family is that the Earth, the spacecraft and the Moon are aligned in this order at $t = 0$. This alignment does not represent a significant restriction. For example, if a spacecraft is in a circular parking orbit of 400 km above the Earth's surface, it will occur every

1.54 hours; practically the orbital period of the parking orbit. Figure 3.13 shows a typical periodic orbit of G Family. This kind of trajectory is a starting point of the transfers presented in this work.

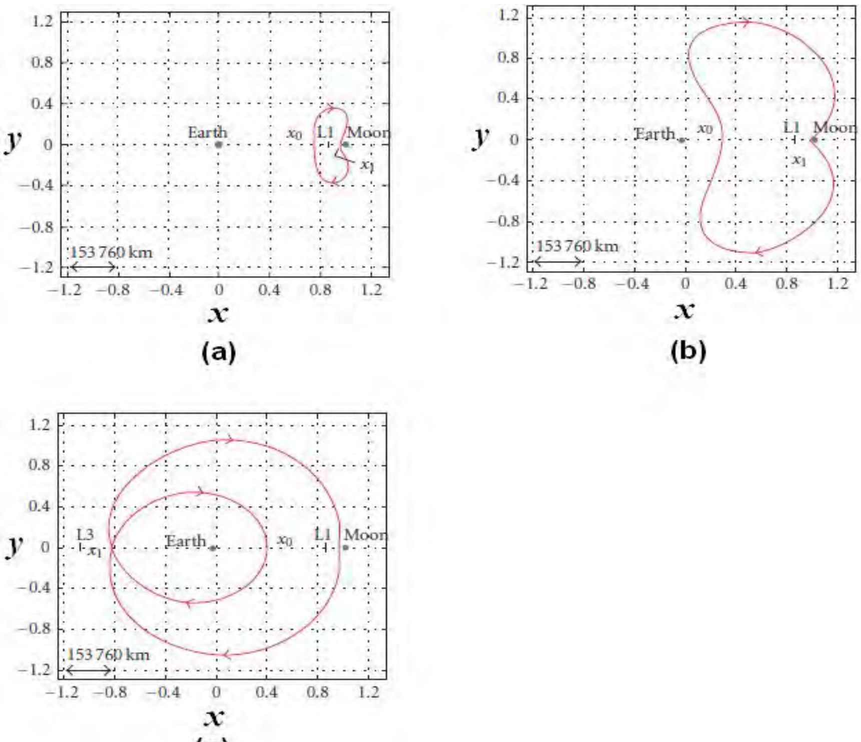

(a)

(b)

(c)

Figure 3.13 - Lagrangian equilibrium points and typical orbits of the G Family in the synodic coordinate system: (a) $(x_0, 0, \dot{x}_0, \dot{y}_0) = (0.741686, 0, 0, 0.53176)$, (a) $(x_0, 0, \dot{x}_0, \dot{y}_0) = (0.299999, 0, 0, 0.195941)$ and (c) (a) $(x_0, 0, \dot{x}_0, \dot{y}_0) = (0.399997, 0, 0, -2.271238)$.
From: (MELO et al., 2007)

One of the characteristics of the periodic orbits of G Family is the instability, mainly those that pass few hundred kilometers from the Earth's surface and a few dozen kilometers from the Moon's surface as show in Fig. 3.13(b). Therefore, it is possible to derive, from these periodic orbits, trajectories capable to transfer spacecraft from an Earth parking orbit to the Moon's sphere of influence.

Once the spacecraft reaches the Moon's sphere of influence, our goal is to use the Moon's gravitational force in such a way that the spacecraft either gains or losses enough energy to arrive at L_4 or L_5. Therefore, the firsts step is to inject the spacecraft into one of these trajectories that link the Earth to the Moon's sphere of influence.

Starting at a circular Earth parking orbit of radius r_0, a first thrust impulsive $\Delta \boldsymbol{v_1}$ is applied to the spacecraft to put it in a trajectory derived from the G Family. Figure 3.14 illustrates the quantities involved in the problem. The initial conditions in the non-dimensional synodic frame are given in the form of Eq. (3.59):

$$x_0 = \frac{r_0}{d_{EM}} - \mu, \tag{3.60}$$

$$\dot{y}_0 = \left(\frac{v_0}{\omega d_{EM}}\right) - x_0 - \mu. \tag{3.61}$$

where v_0 is the magnitude of the velocity at departure.

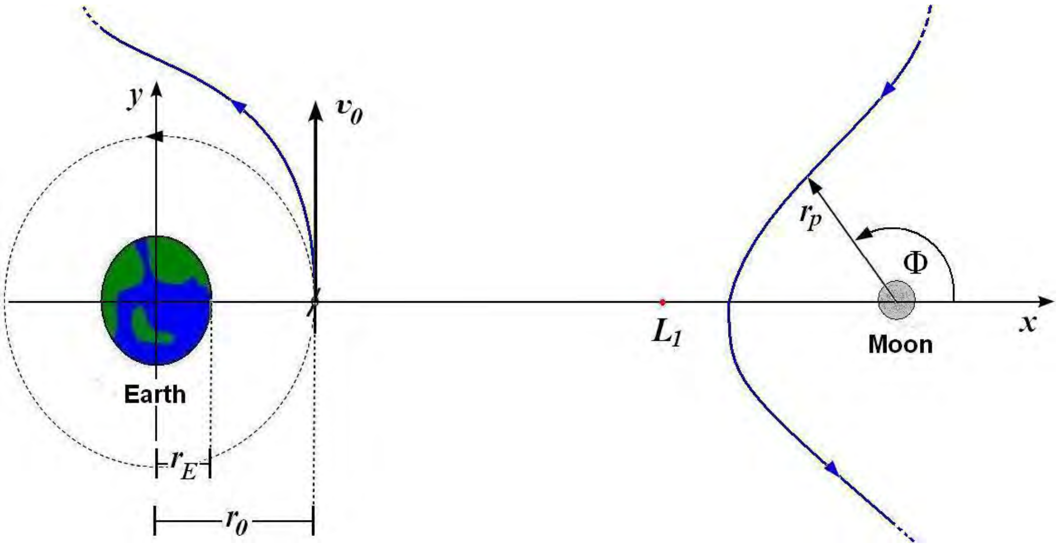

Figure 3.14 - Illustration of the quantities involved in the insertion of a spacecraft into a periodic orbit of G Family. Orbit seen in the synodic frame (not to scale).

In a previous study, de Melo et al. (MELO et al., 2007), (MELO et al., 2009) established a mathematical expression for the first Δv_1 as a function of the radius r_0 of the initial circular Earth parking orbit. This expression has the following form,

$$\Delta v_1 = \frac{v_i}{2}\left(-2.3340 \times 10^{-6}\left(r_0 - r_E\right) + 0.08085 \pm 0.0001\right) + \varphi + \vartheta, \tag{3.62}$$

where $v_i = \sqrt{\mu_E / r_0}$. The term φ corresponds to disturbances to the dynamics of the restricted three-body Earth-Moon-particle problem as Sun's gravitational field, solar radiation pressure, Earth oblateness, the eccentricities of the Earth's and the Moon's orbits, among others. Whether none is considered, $\varphi = 0$. The term ϑ represents small increments in Δv_1 and its value will determine the magnitude and the positioning of the periselenium vector, $\boldsymbol{r_p}$, relative to the Moon and the kind of Trajectory G that will be generated. Values for φ that describe the actions of the Sun's gravitational field and the eccentricities of the Earth's and the Moon's orbits can be found in (MELO et al., 2009).

Thus, it is possible to generate a G Trajectory from a periodic orbit of G Family ($\varphi = 0$) in two ways. With a small increment in Δv_1 ($\vartheta \neq 0$), or with the application of a small Δv in the orbit's apogee prior the passage through the lunar sphere of influence (MELO et al., 2007), (MELO et al., 2009). Any of these procedures is sufficient to produce a swing-by with the Moon during the spacecraft passage through the lunar sphere of influence. The second is more complex, because it requires a control system to provide the correct direction to the small Δv at the correct time. However, there is not a significant difference in terms of the increment of the velocity due to the inherent instabilities of the orbits when the objective is to reach L_4 or L_5. On the other hand, a control system always will be required to keep the spacecraft in the appropriated trajectory mainly due to the disturbances of the Sun's gravitational field in real missions. Therefore the magnitude of the velocity at departure $\boldsymbol{v_0}$ is

$$v_0 = v_i \left(1 + \frac{1}{2}\left(-2.3340 \times 10^{-6}\left(r_0 - r_E\right) + 0.08085 \pm 0.0001\right)\right) + \vartheta. \qquad (3.63)$$

When the spacecraft reaches the Moon's sphere of influence, the sign of the variation of the spacecraft's energy relative to the Earth due to the swing-by will depend on the angle between the direction of the radius vector of the spacecraft's periselenium, $\boldsymbol{r_p}$, and the axis-x of the synodic frame that unites the Earth to the Moon (BROUCKE, 1988). This angle is denoted by Φ. These quantities are shown in Fig. 3.14. According to Broucke (BROUCKE, 1988), for $0^\circ \leq \Phi \leq 180^\circ$ the energy variation will be negative and for $180^\circ < \Phi \leq 360^\circ$ the energy variation will be positive.

Considering the synodic frame, it is verified numerically that the spacecraft must realize a swing-by passing by the Moon's trailing side to reach an orbit around L_4. This implies $180^\circ < \Phi \leq 360^\circ$ and the energy increment is positive. On the other hand, to deliver a spacecraft up to an orbit around L_5, it must realize a swing-by passing by the Moon's leading side ($0^\circ < \Phi \leq 180^\circ$) to get a negative energy variation (SALAZAR et al., 2012). Figure 3.15 shows these two situations explored here. Once the swing-by is made, the spacecraft will reach the Lagrangian points L_4

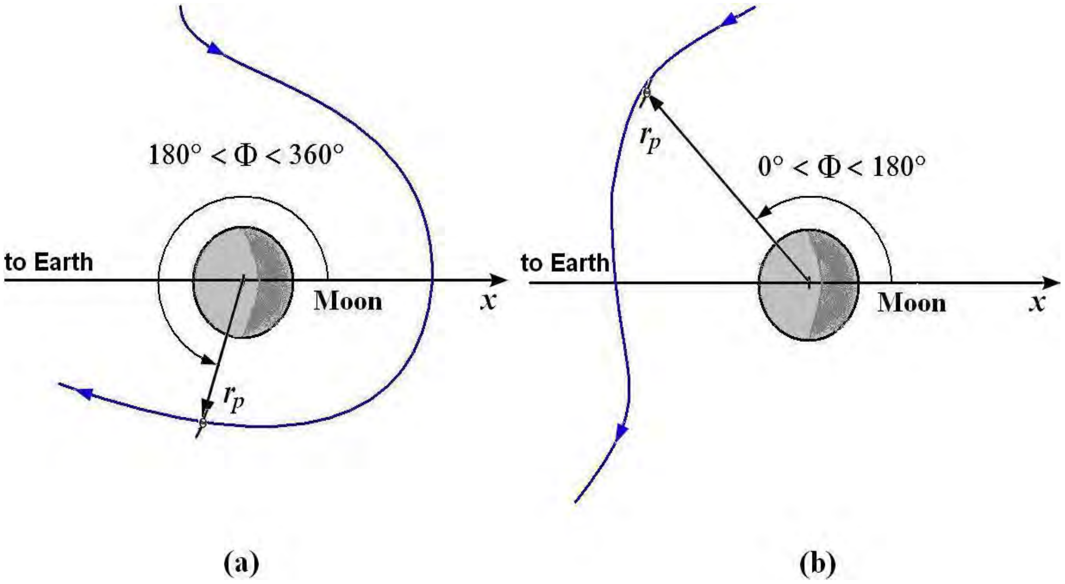

Figure 3.15 - Swing-by orbits: (a) Passing by the Moon's trailing side to reach L_4 ($180° < \Phi \leq 360°$) (b) Passing by the Moon's leading side to reach L_5 ($0° < \Phi \leq 180°$).

and L_5.

In this manner whether the radius r_0 of the initial parking orbit is fixed, the only independent variable is the magnitude of the velocity at departure v_0 as we can see in initial conditions (3.62) and (3.63). The goal therefore is to find the value of v_0 such that, making a swing-by with the Moon, the spacecraft's trajectory intersects the semi-major or semi-minor axis of the periodic orbits around L_4 and L_5. Now, note that, if r_0 is fixed, the only term in Eq. (3.63) that can be altered is the parameter ϑ which defines exactly the spacecraft's relative position to the Moon. The other terms remain fixed. Therefore, the objective is to determine the value of the parameter ϑ such that Eq. (3.4) or (3.5) is satisfied. Similarly, because the continuity of the system of differential equations (2.47), Equations (3.4) and (3.5) can be solved quickly using the Newton-secant method. Once the spacecraft intersects the elliptic orbit, the stabilizing impulsive thrust $\Delta \boldsymbol{v_2}$ is applied to place the spacecraft into the periodic orbit. The total cost Δv_T of the transfer is computed by Eq. (3.19).

3.5 Using Chaos for transference to L4 and L5 Earth-Moon System

In this section, we introduce a new low-cost orbital transfer strategy that opportunistically combine electric propulsion, chaotic and swing-by transfers to get a very efficient strategy to place a spacecraft in Lagrangian points L_4 or L_5. This strategy is not only efficient with respect to thrust requirement, but also its time transfer is comparable to others known transfer techniques based on time optimization.

3.5.1 Entering the Connected Chaotic Component that leads to the Moon

As we could see in Sect. 2.2, there exits a quantity that remains constant along the trajectory of the particle in the CRTBP. This constant quantity is known as Jacobi integral. In 1890, H. Poincaré showed that for a certain value of the Jacobi integral, the trajectory of the third body presents an irregular behavior that now is know as a 'chaotic behavior' (LI; YORKE, 1975), i.e. sensitivity to initial conditions and parameters values. These 'chaotic trajectories', due to their sensitivity to initial conditions can be exploit to allow low energy transfer of a spacecraft from a circular parking orbit around the Earth to the Moon (SCHROER; OTT, 1997), (MACAU; GREBOGI, 2001), (MACAU; GREBOGI, 2006), (MACAU et al., 2011). However, the flight time for this kind of transfer orbit may be too long compared with other transfer methods studied in the previous sections.

The first step to transfer a spacecraft from an Earth circular parking orbit to the Moon's sphere of influence through the connected chaotic component is to place the spacecraft at an altitude of $59,669$ km (BOLLT; MEISS, 1995b). However, using the Hohmann transfer, the cost for this maneuver could be very high (approx. 4.1 km/s). In this case, the cost of the mission must first be reduced for small levels. One of the alternatives that have been used for many years, specially for Russian satellites, is the electric propulsion which offers much higher specific impulse but the thrust is much weaker compared to the chemical one. This technique offers the advantage of consuming a quantity of propellant mass much smaller than the chemical propulsion will consume for the same mission.

Space orbit transfers can be accomplished by using low thrust trajectories with spacecrafts propelled by electric thrusters. A Permanent Magnet Hall Thruster (PMHT) is an example of propulsion system that could be used. This kind of system will be used in the ASTER Mission, the first Brazilian space exploration mission which is to be launched in 2017 (MACAU et al., 2011),(SUKHANOV, 2010). Considering this propulsion system in our mission, the performance expected for PMHT is shown in Table 3.1

Table 3.1 - Performance expected for PMHT to be used in the ASTER spacecraft From: (MACAU et al., 2011)

Propulsion System	Average Measured Thrust (mN)	Measured Specific Impulse (s)	Propellant Consumption (kg/s)
PHMT	120	$1,600$	$1,0 \times 10^{-6}$

Considering a transfer between two circular Earth orbits, the problem is to find parameters of the spacecraft motion such that the transfer time must be minimum. The following assumptions are taken:

a) The thrust and mass flow rate are constant

b) The thrust is assumed tangential

c) The thrust is not interrupted during the whole transfer

d) The external forces include only the Earth's gravitational force

e) The initial and final orbits are circular

Under these assumptions, the low-thrust trajectory is spiral with instantaneous orbits close to circular ones at any time of the transfer as illustrated in Fig. 3.16. Let us suppose an initial circular orbit of radius r_0. The spacecraft must be transferred to a higher orbit of radius $r_f = 59,669$ km.

In this manner, once the spacecraft is boosted to achieve the higher orbit, the mass flow rate can be found as follows:

$$\dot{m} \;=\; -\frac{F}{I_{sp}g}, \tag{3.64}$$

where F and I_{sp} are the thrust and the specific impulse, respectively, $g = 9.80665$ m/s^2 is the acceleration of free fall (GREENWOOD, 1988), (WERTZ; LARSON, 1991). Therefore, if the spacecraft has an initial mass of m_0, then the final spacecraft mass

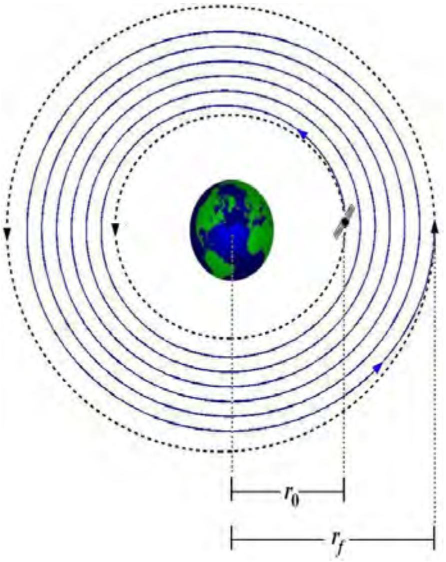

Figure 3.16 - Spiral trajectory to transfer a spacecraft between two circular Earth orbits of radius r_0 and r_f using a constant tangential thrust.

m_f, transfer time Δt and number of spacecraft orbits $\mathcal{N}$ during the time Δt can be computed using the following equations (SCHAUB; JUNKINS, 2003)

$$m_f = m_0 e^{\left(-\frac{v_f - v_i}{I_{sp}}\right)}, \tag{3.65}$$

$$\Delta t = \frac{m_0 - m_f}{\dot{m}}, \tag{3.66}$$

$$\mathcal{N} = \frac{(I_{sp} g)^3}{2\pi \mu_E \dot{m}} |L_3|, \tag{3.67}$$

where $v_i = \sqrt{\mu_E / r_0}, v_f = \sqrt{\mu_E / r_f}$ and the integral

$$L_3 = \int_0^{\Delta t} \left(\frac{v_i}{I_{sp} g} + \ln s \right) ds, \tag{3.68}$$

is calculated using the following relation:

$$L_n = m_f \left(\frac{v_f}{I_{sp} g} \right)^n - m_0 \left(\frac{v_i}{I_{sp} g} \right)^n - n L_{n-1}, \tag{3.69}$$

with

$$L_0 = m_f - m_0, \tag{3.70}$$

and $n = 1, 2, \ldots$ (MACAU et al., 2011).

3.5.2 Chaos in the CRTBP

H. Poincaré (POINCARÉ, 1890) showed that there exists a region of irregular behavior in the phase space $(x, y, \dot{x}, \dot{y})$ of the system (2.47) at $C = 3.17948$. This irregular behavior is called today as chaotic (LI; YORKE, 1975). To inject a spacecraft into the chaotic phase space region, the particle must reach altitudes about 59,669 km from the Earth's center. So, starting at a circular parking orbit of radius r_0, an electric propulsion system could transfer the spacecraft to a higher orbit of radius $r_f = 59,669$ km. Once the spacecraft has reached this altitude, a first burn is required to inject the spacecraft into the chaotic region such that the Jacobi integral (2.24) must be equal to 3.17948. This burn represents a change in velocity of $\Delta v_1 = 0.7444$ km/s (BOLLT; MEISS, 1995b). A typical trajectory of the spacecraft after the first burn is depicted in Fig. 3.17. The spacecraft moves freely in the chaotic region until it reaches the Moon. However, in this particular case, the vicinity of the Moon is reached for the first time after 25 years. This flight time is not compatible with a real mission.

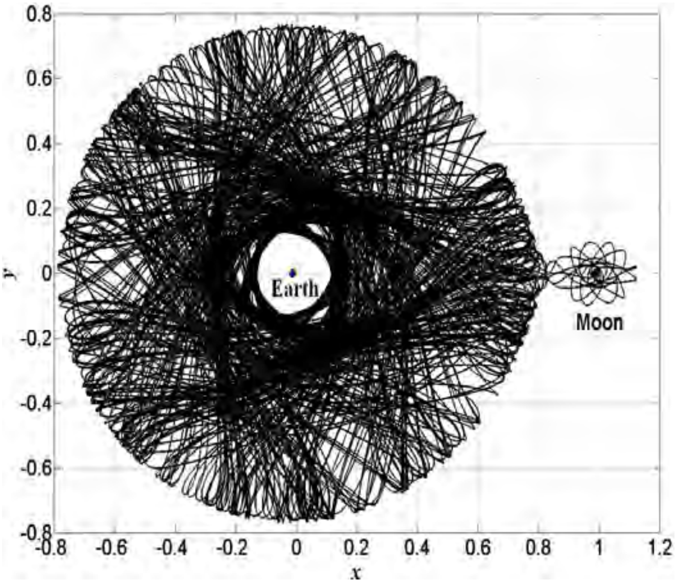

Figure 3.17 - Trajectory of the spacecraft in the chaotic region for the Earth-Moon system (time of flight: 25 years).

Thus the first question at this point is the following: Why this time of flight is so long. To answer this question, let us first introduce a Poincaré section on the phase space $(x, y, \dot{x}, \dot{y})$ such that the trajectories intersect it. In this case, the section defined is the set of points with $y = 0$. In this manner, given any trajectory, only the points, in which this trajectory intersects the x-axis with either $\dot{y} > 0$ or $\dot{y} < 0$, are obtained and positioned properly on the Poincaré Section. So, the analysis of trajectories can be undertaken just considering the points on this section. Notice that this is also just possible because of the Jacobi constant, which by itself confines the dynamics in a space of dimension equals to 3. As so, the dynamics of our problem can be analyzed in a two dimensional phase space.

Figure 3.18a shows the Poincaré section of approximately 200 trajectories of the CRTBP at $C = 3.17948$. The positions of the Earth and the Moon are $(-\mu, 0)$ and $(1 - \mu, 0)$, respectively. Figure 3.17b also shows the chaotic region in the middle of periodic orbits represented by robust islands. Additionally, this chaotic region extends to the vicinity of the Moon. Therefore this shows why it is possible to transfer a spacecraft from the Earth to the Moon through the chaotic region.

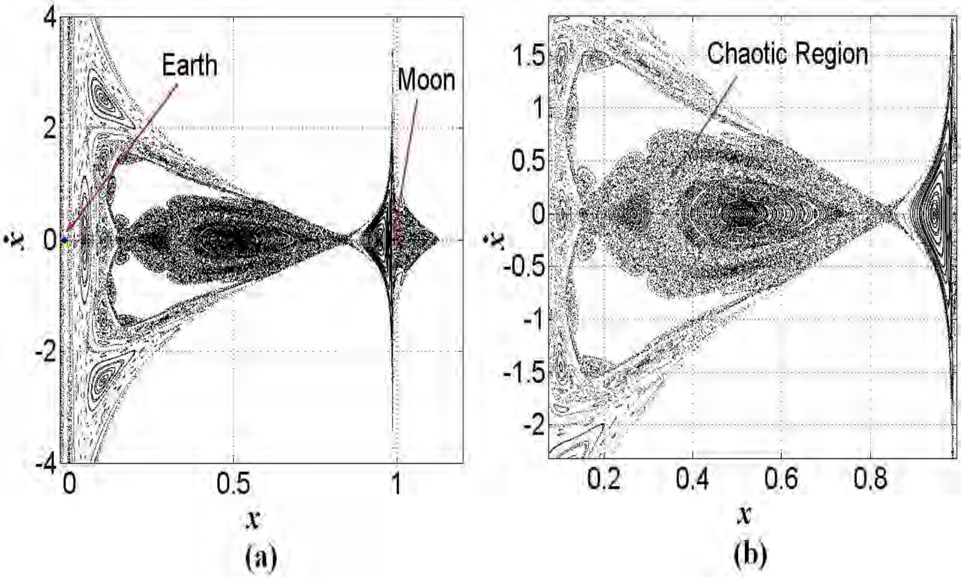

Figure 3.18 - (a) Poincaré section of the CRTBP at $C = 3.17948$ for the Earth-Moon system, (b) Chaotic region in the middle of periodic orbits represented by robust islands.

Figure 3.19 shows the Poincaré section with negative $\dot{y}$ of the trajectory shown in Fig. 3.17. This section shows a 703 iterate orbit, where the last iterate reaches the Moon at about 2,472 km above its center and is denoted by $(x_N, \dot{x}_N)$. This orbit is inside of the chaotic region and we can note that the orbit returns to points of the same orbit very close and this happens many times as illustrated in Fig. 3.20. This fact is known as recurrences and its existence is proved in the Poincaré recurrence theorem (POINCARÉ, 1890). This explains why the flight time of the trajectory is so long.

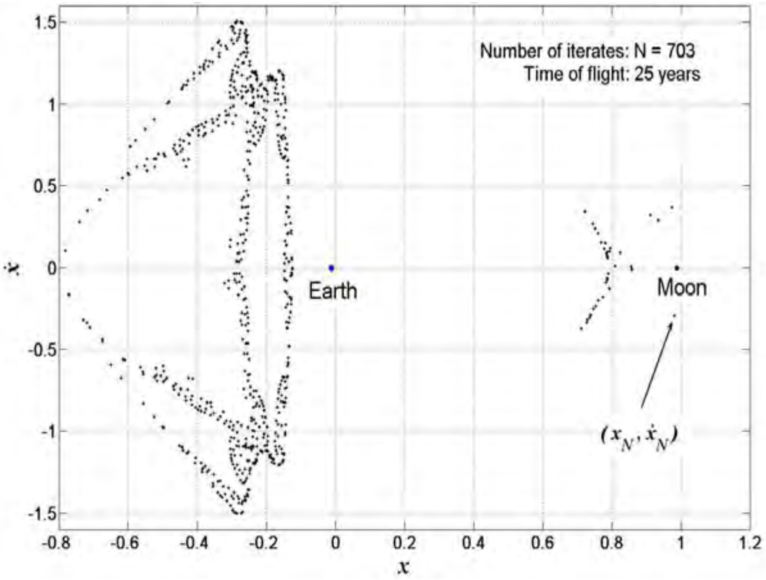

Figure 3.19 - Poincaré section with negative $\dot{y}$ of the chaotic trajectory of the spacecraft shown in Fig. 3.17.

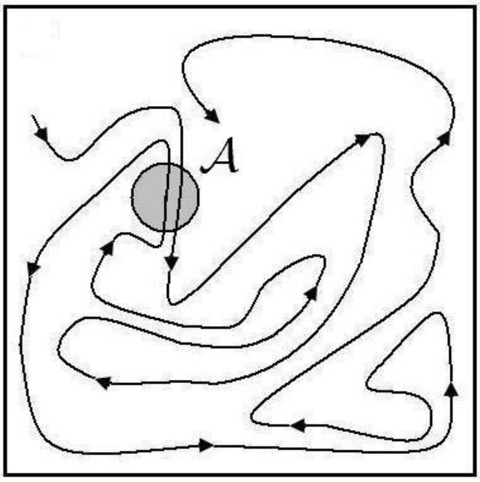

Figure 3.20 - Poincaré recurrences: the orbit returns to set $\mathcal{A}$ many times.

3.5.3 Removing Recurrences

Bollt and Meiss (BOLLT; MEISS, 1995a) introduced an algorithm to remove recurrences of a chaotic orbit in the Poincaré section. This strategy is, firstly, to find the recurrent loops and, finally, to cut them making small perturbations (controls) along the stable and unstable manifolds in the phase space $(x, \dot{x})$. Therefore, this algorithm permits constructing an Earth-Moon pseudo-orbit from a chaotic orbit such that the flight time of the uncontrolled chaotic trajectory is reduced substantially.

Let

$$(z_0, \ldots, z_i, \ldots, z_N)\,, \tag{3.71}$$

denote the points of the orbit shown in Fig. 3.18. In this case,

$$z_i \;=\; (x_i, \dot{x}_i)\,. \tag{3.72}$$

A loop is said to be recurrent when given $\epsilon > 0$, there exist positive integers i and s such that

$$\|z_i - z_{i+s}\| < \epsilon, \tag{3.73}$$

where $\| \;\; \|$ denotes the Euclidean norm.

Therefore, given a $\epsilon > 0$, the following algorithm described in Fig. 3.21 finds efficiently the recurrences in the orbit (3.71):

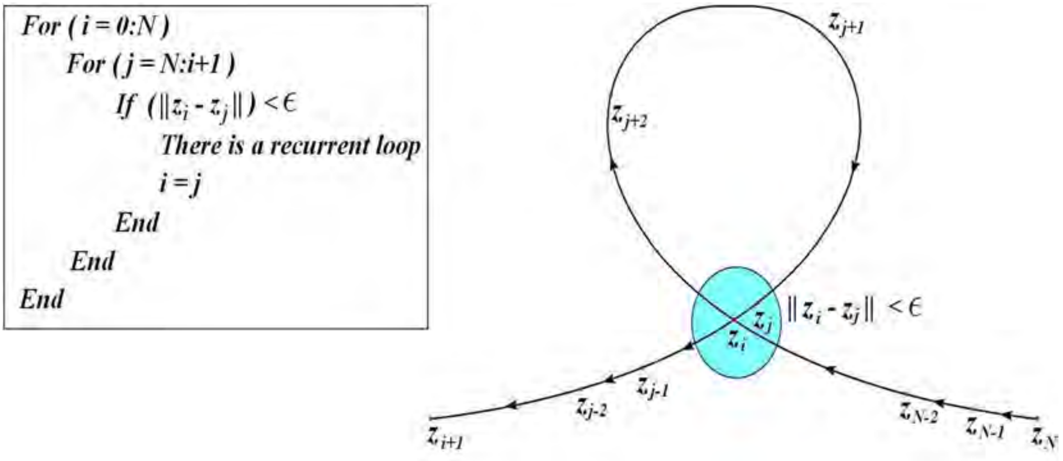

```
For ( i = 0:N )
    For ( j = N:i+1 )
        If ($\|z_i - z_j\|$) < $\epsilon$
            There is a recurrent loop
            i = j
        End
    End
End
```

Figure 3.21 - Algorithm to find efficiently recurrences.

Given a $\epsilon > 0$, suppose that the previous algorithm found a recurrent loop between iterates i and $i+s$ as shown in Fig. 3.22. Because the orbit (3.71) is hyperbolic, then it has two invariant sets: a stable manifold and an unstable manifold associated to this trajectory (OTT, 2002). The stable manifold is the set of points z such that the forward iterated on time orbit starting from z approaches the orbit (3.71). Similarly, the unstable orbit is the set of points z such that the backward iterated on time orbit starting from z approaches the orbit (3.71).

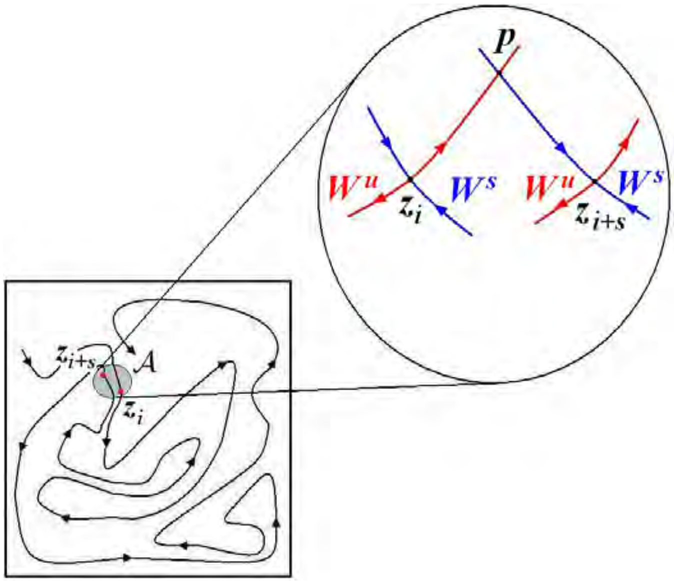

Figure 3.22 - Illustration of a recurrent loop between iterates i and $i+s$. Stable W^s and unstable W^u manifolds intersect each other at a point p.

Now, let W^s and W^u denote the stable and unstable manifolds of the orbit (3.71), respectively. Since there exists a recurrent loop between iterates i and $i+s$ and they are on a hyperbolic set, then stable and unstable manifolds intersect each other at a point p as shown in Fig. 3.22. Thus let

$$(p_{-m}, p_{-m+1}, \ldots, p_{-1}, p)\,, \tag{3.74}$$

and

$$(p, p_1, \ldots, p_{n-1}, p_n)\,, \tag{3.75}$$

be the pre-orbit and orbit of point p, respectively. By the definition of unstable manifold, the pre-orbit of point p will approach the pre-orbit of iterate i before the recurrence. Similarly, the orbit of point p will approach the orbit of iterate $i+s$ after the recurrence as illustrated in Fig. 3.23.

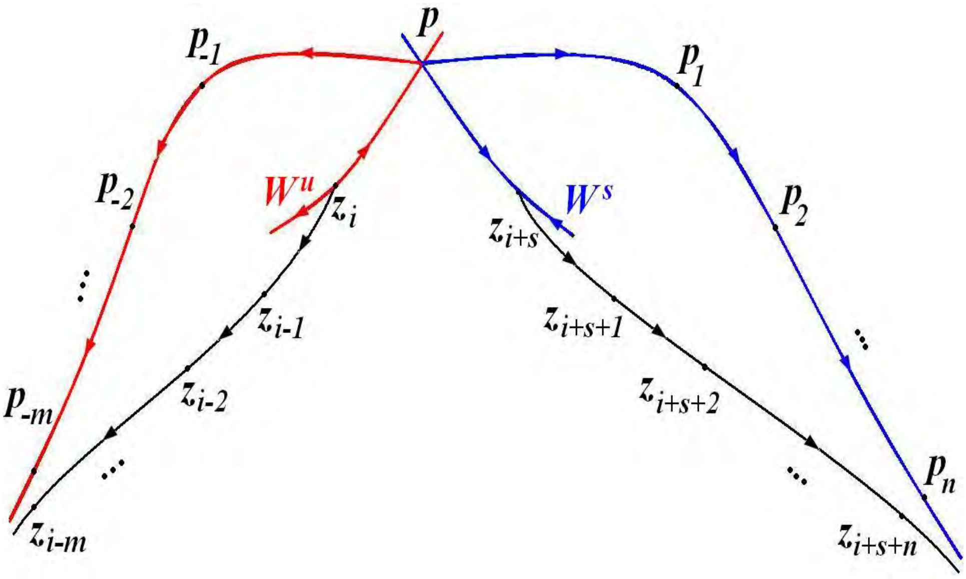

Figure 3.23 - Iterates i and $i+s$ intersect each other at a point p such that the pre-orbit and orbit of p approach the pre-orbit and orbit of iterate i and $i+s$, respectively.

In other words

$$\lim_{m \to +\infty} \|p_{-m} - z_{i-m}\| = 0, \tag{3.76}$$

and

$$\lim_{n \to +\infty} \|p_n - z_{i+s+n}\| = 0. \tag{3.77}$$

From the above result follows that for a sufficiently large integers m,n, the $(s-1)$-step loop can be removed making a small perturbation Δu_1 in the iterate $i-m$,

$$z_{i-m} + \Delta u_1 = z'_0, \tag{3.78}$$

such that, the orbit

$$\left(z'_0, \ldots, z'_{n+m}\right), \tag{3.79}$$

approaches the iterate $i+s+n$. Making a second small perturbation Δu_2 in the last iterate of the orbit (3.79), it is possible to get back to the original orbit (3.71),

$$z'_{m+n} + \Delta u_2 \quad = \quad z_{i+s+n}, \tag{3.80}$$

as illustrated in Fig. 3.24. Now, note that the perturbations (3.78) and (3.80) can only be made in the $\dot{x}$ component of the phase space (since teleportation is not physical). Therefore, perturbation (3.80) requires that the two points have the same x coordinate, thus

$$x'_{m+n} - x_{i+s+n} \quad = \quad 0. \tag{3.81}$$

Thus, given a $\epsilon > 0$ small enough so that a recurrent loop exists between iterates i and $i+s$, then the $(s-1)$-steep loop can be removed finding integers m and n large enough and a perturbation (3.78) small enough such that Eq. 3.81 is satisfied. These can be found using the Newton-secant method for some prescribed tolerance (approx. 10^{-6}).

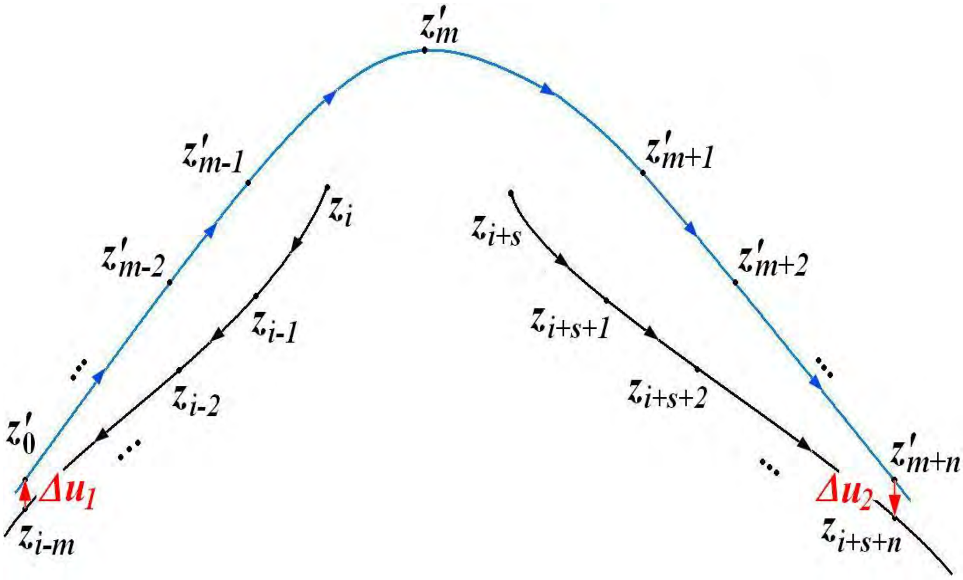

Figure 3.24 - A small perturbation Δu_1 is made in the pre-orbit of iterate i such that the new orbit approaches the orbit of iterate $i+s$ and finally a second small perturbation Δu_2 must be made to get back to the original orbit.

3.5.4 Reaching L_4 and L_5

Once the recurrences have been removed the spacecraft will reach the Moon as shown in Fig. 3.17, and it will be possible to use its gravitational force to change the trajectory of the spacecraft and reach, for example, the Lagrangian points L_4 or L_5 in the Earth-Moon system (PRADO, 1993), (PRADO, 1996). However, in this particular case, the Moon's gravitational force is not enough and an impulsive thrust is necessary to increase the energy such that the zero-velocity curves permit the spacecraft to reach either L_4 or L_5.

Let

$$(x_N, y_N, \dot{x}_N, \dot{y}_N) \tag{3.82}$$

be the final position of chaotic trajectory shown in Fig. 3.19. Thus $y_N = 0$ and $\dot{y}_N < 0$. Since the Jacobi integral C is equal to 3.17948 along the trajectory, a new boost is required such that $C < 2.9880$. If $C < 2.9880$, the zero-velocity curves disappear and the spacecraft can arrive at either L_4 or L_5 as illustrated in Fig. 3.25 (see Table 2.2). Therefore, applying an impulsive thrust Δu_N parallel to the y-axis as shown in Fig. 3.25, the change in the velocity for arriving at equilibrium points is given by Eq. 2.24:

$$\Delta u_N = \left(\sqrt{x_N^2 + 2\frac{1-\mu}{\rho_E} + 2\frac{\mu}{\rho_M} - \dot{x}_N^2 - 2.9880 + \varsigma}\right) + \dot{y}_N. \tag{3.83}$$

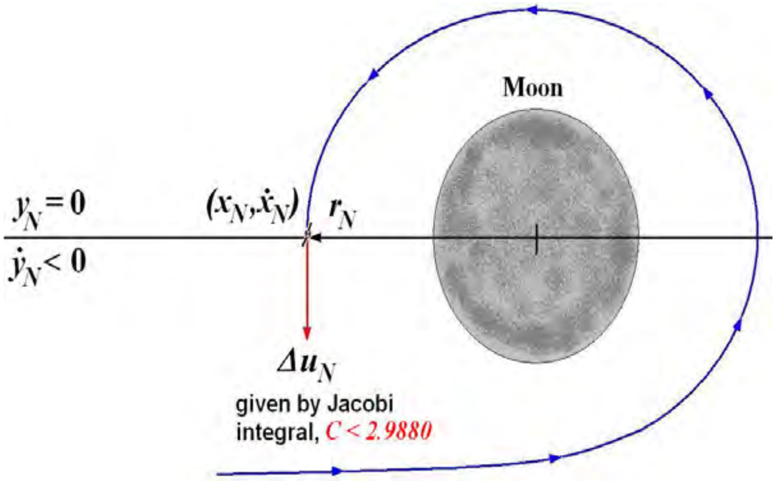

Figure 3.25 - Swing-by maneuver to reach Lagrange equilibrium points L_4 or L_5 for the Earth-Moon system.

Note that Eq. (3.83) has the term ς. This term is a correction due to Eq. (2.24) is the Jabobi integral and it only gives the necessary condition for the velocity curves disappear, however, this does not guarantee that the spacecraft arrives at Lagrangian points. So, a small correction is needed. The term ς depends on the characteristics of the periodic orbit around the equilibrium point where the spacecraft has to be placed, i.e. semi-major and -minor axes. Therefore the goal is to find the value of ς such that Eq. (3.4) or (3.5) is satisfied. This can be done following a continuation criterion. Once the spacecraft intersects the elliptic orbit, the stabilizing impulsive thrust $\Delta \boldsymbol{v_2}$ is applied to place the spacecraft into the periodic orbit. The total cost Δv_T of the transfer is

$$\Delta v_T \quad = \quad \Delta v_1 + \sum \Delta u_1 + \sum \Delta u_2 + \Delta u_N + \Delta v_2, \tag{3.84}$$

where $\sum \Delta u_i$ denotes the sum of the all perturbations applied to eliminate the recurrences.

4 THE ZERO, MINIMUM AND MAXIMUM RELATIVE RADIAL ACCELERATION FOR FORMATION FLYING

The transfer methods described in Chapter 3 permit to place a spacecraft in a periodic orbit around L_4 or L_5. These methods can be applied to one or more spacecrafts, placing them in different periodic orbits. In this manner, assume a constellations of satellites flighting close a given nominal trajectory around L_4 or L_5 in the Earth-Moon system in such a way that there is freedom in the selection of the geometry of the constellation. We are interested in to avoid large variations of the mutual distance between the spacecrafts. In this case, the existence of regions of zero and minimum relative radial acceleration with respect to the nominal trajectory will prevent from the expansion or contraction of the constellation. In the other case, the existence of regions of maximum relative radial acceleration with respect to the nominal trajectory will produce a greater expansion and contraction of the constellation. The goal of this chapter is the study of theses regions using the linearized equations of motion (2.51). At the end, the results will be compared with the dynamical behaviour of the deviation of the constellation from a periodic orbit.

4.1 The Zero Relative Radial Accelerations Lines

In order to avoid expansion or contraction in the relative distance among the satellites of the formation, we have studied the existence of regions with Zero Relative Radial Acceleration (ZRRA). For a simple model, such as the CRTBP, it is possible to compute an analytical expressions for the above regions if the radius of the formation (largest separation between spacecrafts) is small, such that a linear approach gives the relevant information about the local dynamics of the problem. For simplicity, our model only considered motions on the plane of the orbit of the Earth-Moon system. As reference solutions, we will only use a family of periodic orbits around L_4 in each case because the results obtained are the same for periodic orbits around L_5 due to the Theorem of Mirror applied in the Earth-Moon system (MIELE, 1960).

Assume two satellites flying in a formation in a periodic orbit around L_4 as shown in Fig. (4.1). Let $X_h(t)$ and $X(t)$ be the vectors corresponding to the trajectories of the chief and deputy satellites, respectively. The vector $\Delta X(t) = X(t) - X_h(t)$ represents the relative position and velocity vectors of the deputy satellite with respect to the chief satellite at instant t. The coordinates of vector $\Delta X(t)$ are defined in a coordinate system which is parallel to the rotating coordinate system x, y and is centered at $X_h(t)$. Writing the array ΔX as $(\boldsymbol{r}, \dot{\boldsymbol{r}})^T$, where $\boldsymbol{r} = (\Delta x, \Delta y)^T$, the linear system (2.51) becomes

$$\begin{pmatrix} \dot{\boldsymbol{r}} \\ \ddot{\boldsymbol{r}} \end{pmatrix} = \begin{pmatrix} 0 & I \\ F & J \end{pmatrix} \begin{pmatrix} \boldsymbol{r} \\ \dot{\boldsymbol{r}} \end{pmatrix} \tag{4.1}$$

where

$$I = \begin{pmatrix} 1 & 0 \\ 0 & 1 \end{pmatrix}, \quad J = \begin{pmatrix} 0 & 2 \\ -2 & 0 \end{pmatrix}, \quad F = \begin{pmatrix} \frac{\partial^2 U}{\partial x^2} & \frac{\partial^2 U}{\partial y \partial x} \\ \frac{\partial^2 U}{\partial x \partial y} & \frac{\partial^2 U}{\partial y^2 \partial x} \end{pmatrix}.$$

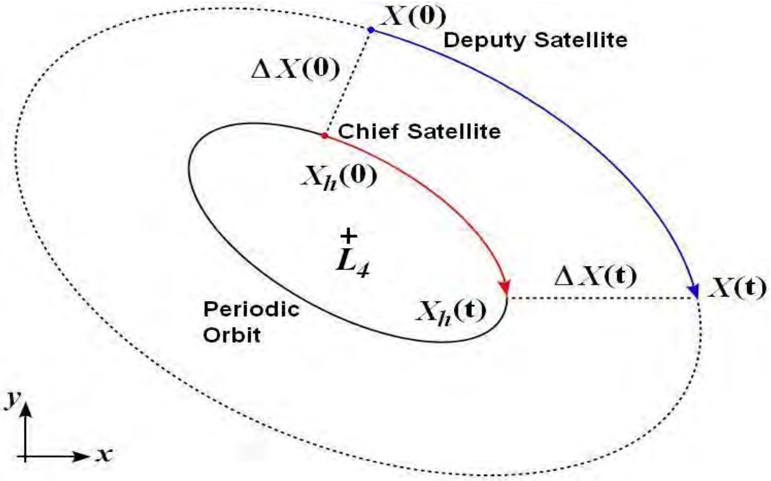

Figure 4.1 - Chief and deputy satellites in a formation in a periodic orbit around L_4.

The points with zero relative velocity are those such that $\dot{\boldsymbol{r}} = \boldsymbol{0}$, and, in this case, we have that the relative acceleration is given by

$$\ddot{\boldsymbol{r}} \;=\; F\boldsymbol{r}. \tag{4.2}$$

Therefore, the radial component of the relative acceleration will be zero in the set of points where the vectors $\ddot{\boldsymbol{r}}$ and $\dot{\boldsymbol{r}}$ are perpendicular, in other words,

$$\boldsymbol{r}^T F \boldsymbol{r} \;=\; 0. \tag{4.3}$$

Equation (4.3) represents two lines which depend on the point $X_h\,(t)$ selected along the periodic solution of system (2.47) as illustrated in Fig. 4.2.

The Zero Relative Acceleration Lines (ZRRAL) can be also computed numerically (GÓMEZ et al., 2006). Given a certain periodic orbit, we select a point on it: $X_h\,(t) =$

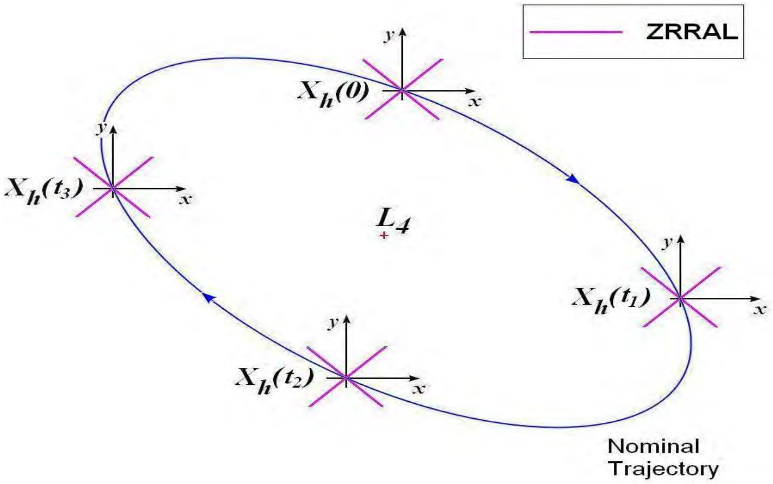
ZRRAL
$X_h(0)$
$X_h(t_1)$
$X_h(t_2)$
$X_h(t_3)$
L_4
y
x
Nominal Trajectory

Figure 4.2 - Illustration of Zero relative radial acceleration lines along a periodic solution

$(\boldsymbol{x_h}(t), \boldsymbol{v_h}(t))^T$. Around this point, we consider a sphere in the configuration space, of radius s and we set the velocity of all the points of the sphere equal to the velocity of the chosen point, $\boldsymbol{v_h}(t)$ (zero relative velocity condition) as shown in Fig. 4.3. Using polar coordinates, the set of points of the sphere will be the following form:

$$\begin{pmatrix} \boldsymbol{x_h}(t) + \boldsymbol{s}(\theta) \\ \boldsymbol{v_h}(t) \end{pmatrix}. \tag{4.4}$$

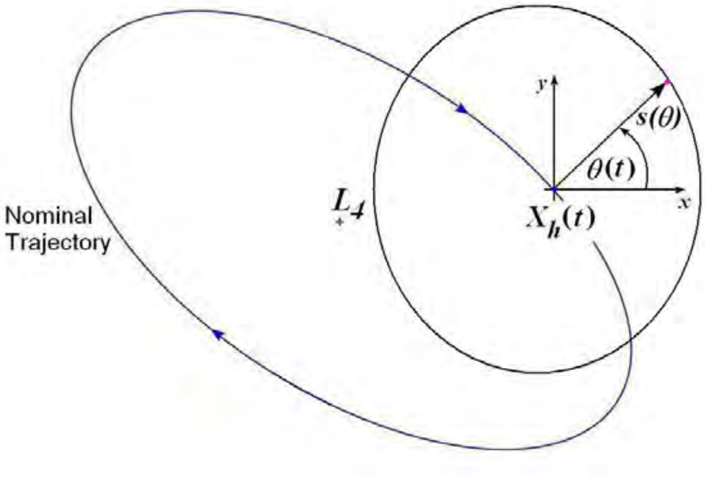
y
x
$s(\theta)$
$\theta(t)$
$X_h(t)$
L_4
Nominal Trajectory

Figure 4.3 - Illustration of a sphere of radius s for each point of the periodic solution $X_h(t)$

Now, writing the equations of the motion (2.47) for X_h as

$$\begin{pmatrix} \dot{\boldsymbol{x}}_{\boldsymbol{h}} \\ \ddot{\boldsymbol{x}}_{\boldsymbol{h}} \end{pmatrix} = \begin{pmatrix} \boldsymbol{f_1}\left(\boldsymbol{x_h}, \boldsymbol{v_h}\right) \\ \boldsymbol{f_2}\left(\boldsymbol{x_h}, \boldsymbol{v_h}\right) \end{pmatrix}, \tag{4.5}$$

the relative acceleration can be evaluated by

$$\boldsymbol{a}\left(t, \theta\right) = \boldsymbol{f_2}\left(\boldsymbol{x_h}\left(t\right), \boldsymbol{v_h}\left(t\right)\right) - \boldsymbol{f_2}\left(\boldsymbol{x_h}\left(t\right) + \boldsymbol{s}\left(\theta\right), \boldsymbol{v_h}\left(t\right)\right), \tag{4.6}$$

whose scalar product with $\boldsymbol{s}\left(\theta\right)$ will be the desired relative radial acceleration for each angle θ. In this manner, we denote by θ^* the angle at which the scalar product between $\boldsymbol{a}\left(t, \theta^*\right)$ and $\boldsymbol{s}\left(\theta^*\right)$ is equal to zero and therefore it will give us the relative position vector $\boldsymbol{r}$ that belongs to ZRRAL as shown in Fig. 4.4.

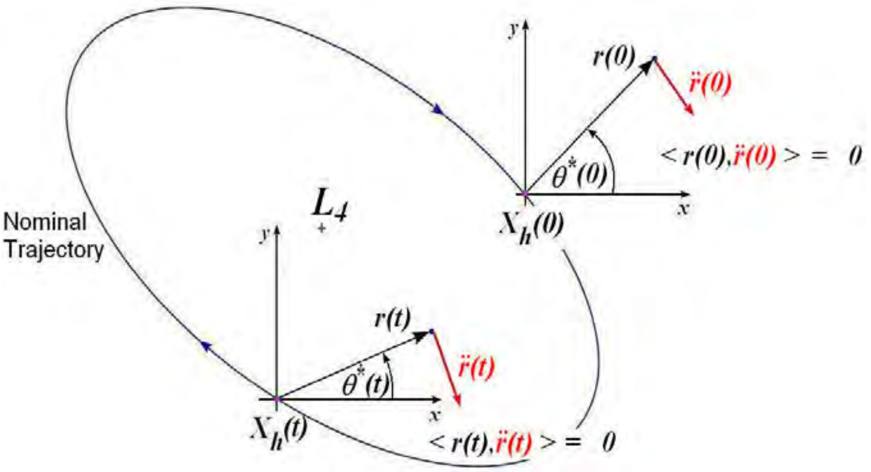

Figure 4.4 - Illustration of the dot product between the relative position and relative acceleration vectors for each point of the periodic solution $X_h\left(t\right)$. The angle $\theta^*\left(t\right)$ defines the direction of the relative position vector $\boldsymbol{r}\left(t\right)$ that belongs to ZRRAL at time t.

4.2 Residual Acceleration and Cost to Maintain a Spacecraft in a Formation

Given a certain nominal trajectory $X_h\left(t\right)$ around L_4, suppose that a spacecraft follows an artificial trajectory around it, i.e. there exists an impulsive thrust (control) applied on it as shown in Fig. 4.5. Denote by $\boldsymbol{r_a}\left(t\right)$ the relative position at time t. If there is no impulsive thrust applied on the spacecraft, then the function $\mathbf{r_a}\left(t\right)$ will satisfy Eq. (4.1). However, if a control is applied on the spacecraft, there is a residual acceleration as a consequence of the maneuvers applied on it (GÓMEZ et al., 2006). In this manner, denoting by $\mathbf{R_a}$ the residual acceleration, it can be computed using Equation (4.1):

$$\boldsymbol{R_a} \;=\; \ddot{\boldsymbol{r}}_{\boldsymbol{a}} - \left(F\boldsymbol{r_a} + J\dot{\boldsymbol{r}}_{\boldsymbol{a}}\right). \tag{4.7}$$

Therefore, the cost, denoted by ΔV, to maintain the spacecraft on an artificial trajectory until a time T is simply:

$$\Delta V \;=\; \int_0^T R_a\left(t\right)dt. \tag{4.8}$$

In this simple manner, we can evaluate the cost of maintaining two or more satellites in formation along a periodic orbit around L_4.

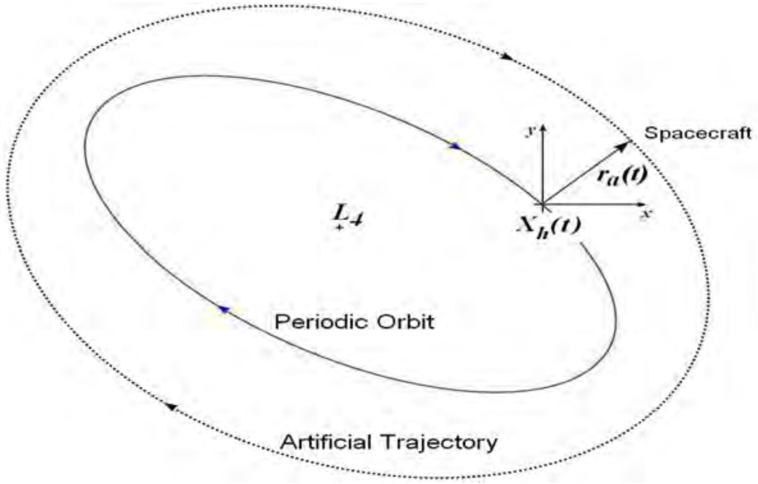

Figure 4.5 - Illustration of a spacecraft following an artificial trajectory $\boldsymbol{r_a}\left(t\right)$ along a periodic trajectory $X_h\left(t\right)$ around L_4.

5 ANALYSIS AND RESULTS

In the first section of this chapter we show the periodic orbits around the equilibrium points where the spacecraft will be placed. In the second section we present the initial parameters, change in velocities, total cost and the time of flight of each transfer orbit to the Lagrangian points L_4 and L_5 using the four methods described in Chapter 3. In all the transfer orbits we started from an Earth circular parking orbit of radius $r_0 = 6,771$ km (400 km above the Earth's surface). Finally, in the third section we compute the regions of maximum, minimum and zero relative radial acceleration component along a family of periodic orbits around L_4 as well as the cost to maintain a formation flying on these regions or another configurations.

All the numerical simulations in this work were performed using C and the compiler was the Microsoft Visual Studio 9.0. The method used to integrate numerically all the trajectories shown in this chapter was the BulirschStoer algorithm (STOER; BULIRSCH, 1980), (PRESS et al., 1992) obtaining a high-accuracy solutions to the system of ordinary differential equations that describe the motion of the particle in the Earth-Moon rotating frame system with minimal computation effort. We pick a dimensionless step-size $h = 1.0 \times 10^{-4}$ and set a tolerance of 1.0×10^{-9}.

5.1 Long and Short Period Orbits

We have chosen two elliptic orbits of different periods to implement each of the four transfer methods. The first orbit belongs to a long period family and the second one belongs to a short period family. Figure 5.1 show the two elliptic orbits centered at L_4 in the non-dimensional coordinate system x'', y'' defined in Eq. (3.1). The lengths of the semi-major and -minor axes, denoted by a and b, respectively, as well as the coordinates in the system x'', y'' of the velocity vectors $\boldsymbol{v_a}$ and $\boldsymbol{v_b}$ at points $(a, 0)$ and $(0, b)$, respectively, are shown in Table 5.1. Note that by the symmetry of the elliptic orbits, we have that $-\boldsymbol{v_a}$ and $-\boldsymbol{v_b}$ represent the velocity vectors at points $(-a, 0)$ and $(0, -b)$, respectively. Additionally, there exist two elliptic orbits with the same characteristics around L_5 due to the Theorem of image trajectories (MIELE, 1960).

Note that in Table 5.1 we have used the conversion factors between the lengths and velocities given in km and km/s, respectively, and the non-dimensional system described in Sect. 2.1. They have been obtained considering the units of length and time equal to d_{EM} (see Appendix) and $1/\omega = 104.222$ h (see Eq. (2.3), respectively.

Table 5.1 - Lengths a and b of the semi-major and minor axes, respectively, and coordinates in the system x'', y'' of the velocity vectors $\boldsymbol{v_a}$ and $\boldsymbol{v_b}$ at points $(a, 0)$ and $(0, b)$ of the elliptic orbits shown in Fig. 5.1

Family	Period (days)	a (km)	b (km)	$\boldsymbol{v_a}$ (km/s)	$\boldsymbol{v_b}$ (km/s)
Long Period	92	$11,000$	$2,150$	$\begin{pmatrix} 0 \\ -1.7972 \times 10^{-3} \end{pmatrix}$	$\begin{pmatrix} 8.7871 \times 10^{-3} \\ 0 \end{pmatrix}$
Short Period	28	$6,400$	$3,142$	$\begin{pmatrix} 0 \\ -8.0094 \times 10^{-3} \end{pmatrix}$	$\begin{pmatrix} 1.6261 \times 10^{-2} \\ 0 \end{pmatrix}$

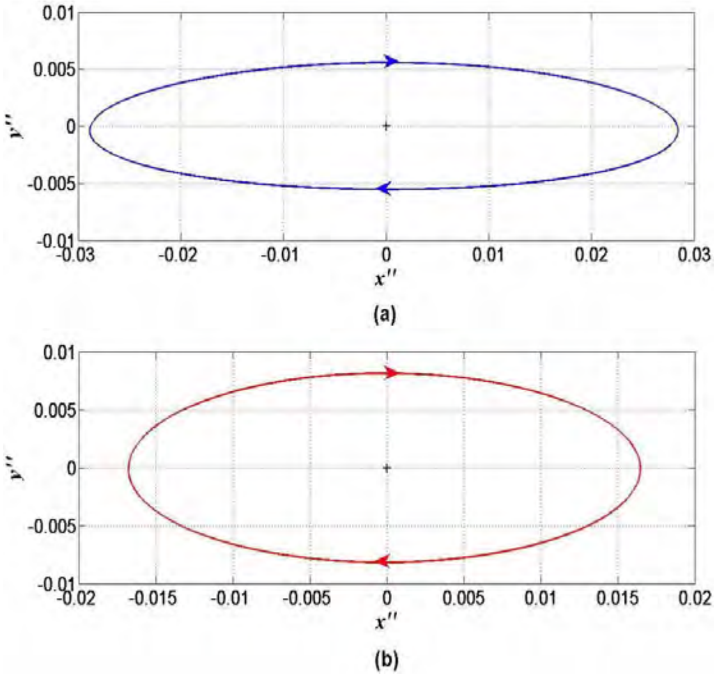

Figure 5.1 - Elliptic Orbits centered at L_4 of (a) 92 and (b) 28 days period. These two orbits have been chosen to implement the transfer orbits methods described in Chapter 3.

5.2 Modified Hohmann Transfer

In this transfer method our goal was to obtain the value of the apocentre d of the elliptic transfer orbit in such a way that this trajectory intersects the elliptic orbits shown in Fig. 5.1 at points $(\pm a, 0)$ or $(0, \pm b)$. As we explained in Sect. 3.2, this can be done by solving Eq. (3.4) or (3.5) by the Newton-Secant method.

Tables 5.2 and 5.3 show the value of d for each elliptic trajectory that reaches the periodic orbits around L_4 and L_5 from an Earth circular parking orbit of radius r_0. Additionally, the phase angle at departure γ_0, tangential change in velocity Δv_1, stabilizing impulsive thrust Δv_2, total cost Δv_T and the time of flight Δt for L_4 and L_5 missions were also computed. Note that the values of these two impulses are similar to the boosts required in the Apollo missions using Hohmann-like transfer which gave $\Delta v_1 = 3.2$ km/s, $\Delta v_2 = 0.8$ km/s, and a time of flight of 3 days (WOODCOCK, 1985). Initial position and velocity coordinates (referred to the non-dimensional rotating frame system) corresponding to departure geometries described in Tables 5.2 and 5.3 are presented in Tables 5.4 and 5.5, respectively.

Figure 5.2 shows the obtained trajectories in the synodic system. In the first and second columns of Fig. 5.2 we can see the trajectories that guide the spacecraft to the long and short period orbits, respectively. It can be noted that there is no difference in the qualitative behaviour of trajectories that reach the long and short period orbits. Additionally, Figure 5.3 shows the moment in which these trajectories intersect the semi-minor axis of the elliptic orbits and it is applied the stabilizing impulsive thrust to place the spacecraft around the equilibrium points. Figure 5.4 shows the trajectories corresponding to Fig. 5.2 in the Earth-centered inertial system $\hat{\boldsymbol{n}}_1, \hat{\boldsymbol{n}}_2$.

Table 5.2 - Apocentre d, phase angle at departure γ_0, change in velocity Δv_1, stabilizing impulsive thrust Δv_2, total cost Δv_T and time of flight Δt for placing a spacecraft into the long and short period orbits around L_4

Period Orbit	d (km)	γ_0 (degrees)	Δv_1 (km/s)	Δv_2 (km/s)	Δv_T (km/s)	Δt (days)
Long	$387,781$	53.43	3.0848	0.8292	3.9140	5.05
Short	$388,768$	53.18	3.0850	0.8248	3.9098	5.07

5.3 Swing-By Maneuver

Considering an Earth circular parking orbit of radius r_0 and as target the two long and short period orbits shown in Fig. 5.1, we have used the swing-by maneuver with the Moon described in Sect. 3.3 to place a spacecraft into each of these periodic or-

Table 5.3 - Apocentre d, phase angle at departure γ_0, change in velocity Δv_1, stabilizing impulsive thrust Δv_2, total cost Δv_T and time of flight Δt for placing a spacecraft into the long and short period orbits around L_5

Period Orbit	d (km)	γ_0 (degrees)	Δv_1 (km/s)	Δv_2 (km/s)	Δv_T (km/s)	Δt (days)
Long	$383,810$	174.43	3.0839	0.8169	3.9008	4.97
Short	$384,725$	174.20	3.0841	0.8124	3.8965	4.99

Table 5.4 - Initial position and velocity coordinates for placing a spacecraft into the long and short period orbits around L_4 (referred to the non-dimensional rotating frame system) corresponding to departure geometries described in Table 5.2

Period Orbit	x_0	y_0	$\dot{x}_0$	$\dot{y}_0$
Long	-0.0016550	-0.0141465	8.4183279	6.2451657
Short	-0.0015934	-0.0141006	8.3911544	6.2819550

Table 5.5 - Initial position and velocity coordinates for placing a spacecraft into the long and short period orbits around L_5 (referred to the non-dimensional rotating frame system) corresponding to departure geometries described in Table 5.3

Period Orbit	x_0	y_0	$\dot{x}_0$	$\dot{y}_0$
Long	-0.0296807	-0.00170967	1.0173072	-10.4315393
Short	-0.0296737	-0.0017800	1.0591935	-10.4275657

bits. As shown in Sect. 3.3.2, once the apocentre d is defined, the only independent variable is the angle λ_0 at which the geocentric departure orbit intersects the lunar sphere of influence (see Fig. 3.5) which is determined solving Eq. (3.4) or (3.5) by the Newton-Secant method. In this manner, finding the value of angle λ_0, the trajectory is integrated in such a way that it intersects the semi-major or -minor axis of the elliptic orbits around the equilibrium points. At that instant, the numerical algorithm stops and changes the coordinates of the velocity, applying the stabilizing impulsive thrust $\boldsymbol{\Delta v_2}$, so that the new trajectory describes the periodic orbits shown in Fig.

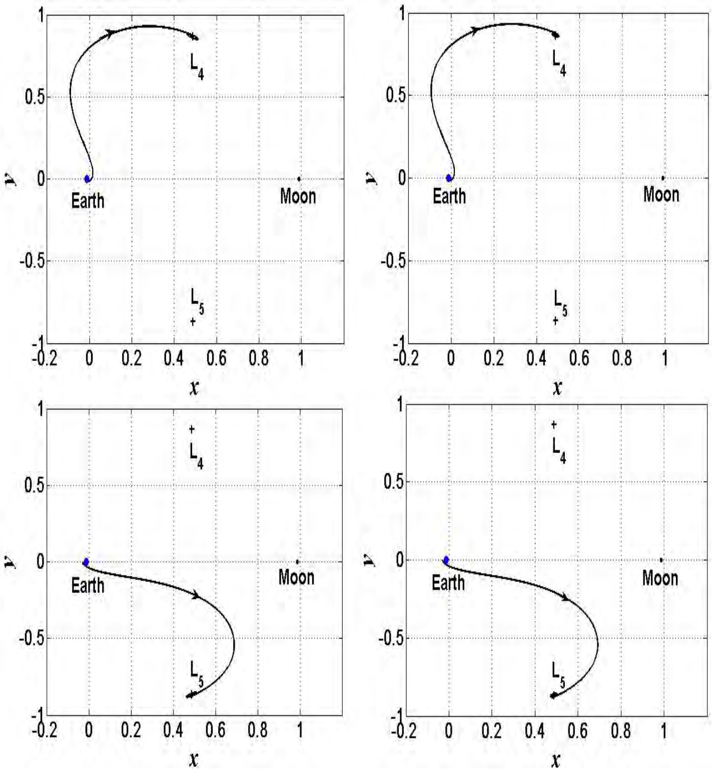

Figure 5.2 - Hohmann transfer orbit to reach the long (first column) and short (second column) period orbits in the synodic system.

5.1. Additionally, since the spacecraft intersects the lunar sphere of influence close to apogee of the geocentric departure trajectory (see Fig. 3.11), the magnitude of the velocity $\boldsymbol{v_1}$, when the spacecraft enters the lunar sphere of influence, is less than the Moon's velocity $\boldsymbol{v_M}$ with respect to the Earth's center, therefore the spacecraft must cross the Moon's sphere of influence in a point above the line that connects the center of the Earth and the Moon as shown in Fig. 3.6. Otherwise, the spacecraft will not approach the Moon following a hyperbolic trajectory with respect to the Moon-centered reference frame system. Thus λ_0 was defined between 0° and 90°.

Now, using the distance d_{EM} and the radius R_S of the lunar sphere of influence, we have considered three different values for the apocentre d. Table 5.6 shows the interval for λ_0 that contains the trajectories that intersect the interior region of the elliptic orbits shown in Fig. 5.1. The trajectories integrated with λ_0 that does not lie in the intervals shown in Table 5.6, they do not cross the elliptic orbits or hit the Moon. It is important to specify that we are only interested in trajectories that make just one swing-by maneuver with to Moon to reach the elliptic orbits around the equilibrium points.

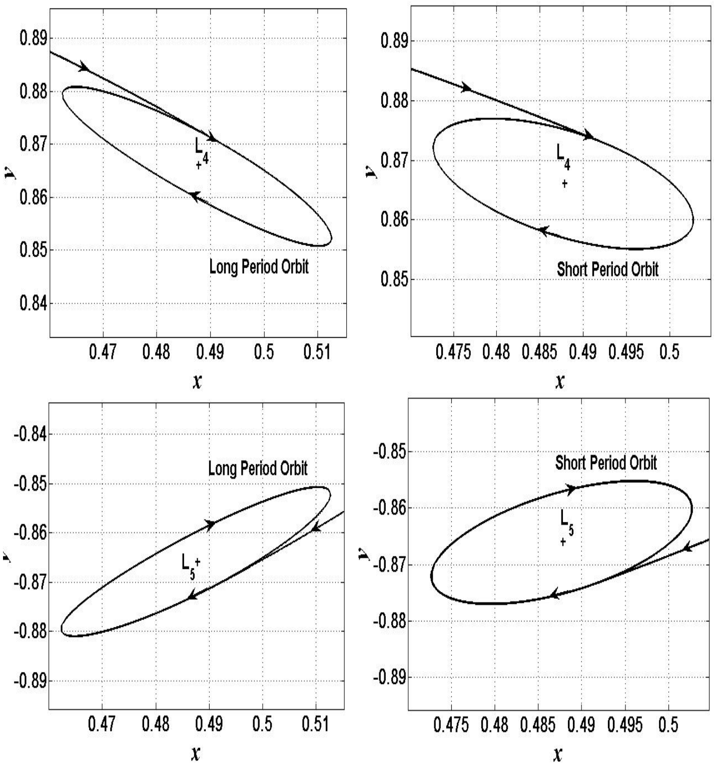

Figure 5.3 - Trajectories corresponding to Fig. 5.2 intersecting the semi-minor axis of the elliptic orbits. At that moment it is applied the stabilizing impulsive thrust to place the spacecraft around the equilibrium points.

In this manner, Tables 5.7 and 5.8 show the value of λ_0 for each trajectory that intersects the semi-major or -minor axis of the elliptic orbits around L_4 and L_5, respectively. Additionally, the phase angle at departure γ_0, the parameters that describe the geometry of the swing-by maneuver (see Fig. 3.7) as well as the change in velocity Δv and energy $\Delta\varepsilon$ after the swing-by maneuver is completed and computed in Eqs. (3.40) and (3.52) are also shown in Tables 5.7 and 5.8. It is interesting to note that there exits an inverse relation between the magnitude of the periselene radius r_p and the change in velocity Δv and energy $\Delta\varepsilon$. The spacecraft can obtain more energy (and therefore more velocity) whether it passes close enough of the Moon's surface.

Similarly, Tables 5.9 and 5.10 show the magnitudes of the first tangential impulse Δv_1 applied to inject the spacecraft into the trajectory, the stabilizing impulsive thrust Δv_2 to place it into the elliptic orbits around L_4 and L_5, respectively, as well as the total cost Δv_T and the time of flight Δt of each transfer orbit. Initial position and velocity coordinates (referred to the non-dimensional rotating frame system) corresponding to departure geometries described in Tables 5.9 and 5.10 are

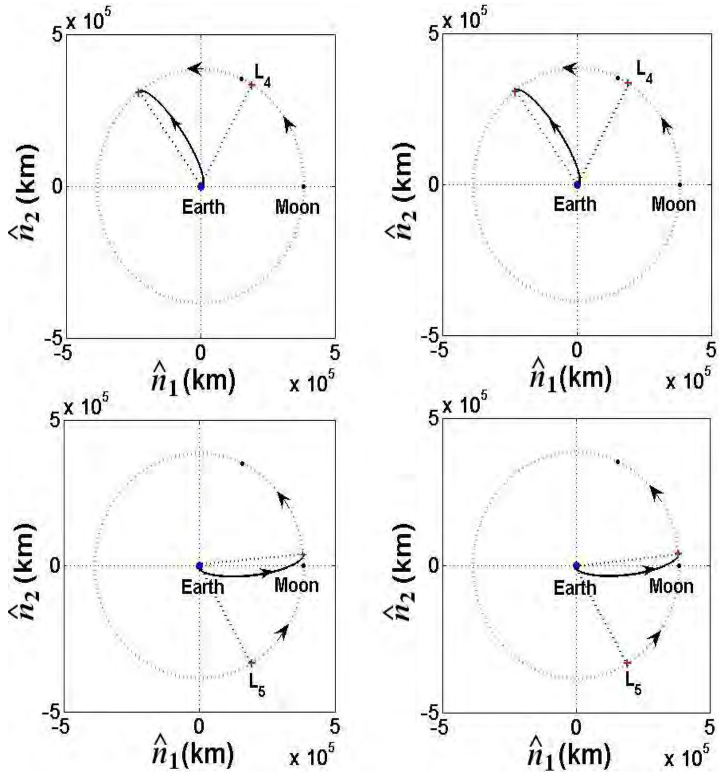

Figure 5.4 - Trajectories corresponding to Fig. 5.2 in the Earth-centered inertial system $\hat{\boldsymbol{n}}_1, \hat{\boldsymbol{n}}_2$.

presented in Tables 5.11 and 5.12, respectively.

From Tables 5.9 and 5.10 it is noted that the total cost of transfer a spacecraft from an Earth circular parking orbit of radius r_0 until it reaches the elliptic orbits around L_4 and L_5 is less whether the apocentre d is equal to $d_{EM} - R_S/2$ and d_{EM}, respectively. Additionally, the trajectories obtained to achieve L_4 are more sensitive whether the apocentre d is equal to $d_{EM} - R_S/2$ as shown in Table 5.6. In this case, the length of the interval is 5° instead of 1° as we can see in the other trajectories. Now, if we want to achieve L_5, we obtain trajectories less sensitive, the length of the interval is 2° when the apocentre d is equal to $d_{EM} + R_S/2$, as shown in Table 5.6. These results are important because in a real space mission, to intercept the lunar sphere of influence at a specific point, the mission planners must look at the motion of the Earth and Moon and plan their launch windows accordingly. The L_4 mission, for example, not only spends less fuel when the apocentre is minimum but the trajectory is more sensitive regarding L_5 mission.

The trajectories corresponding to Tables 5.7 and 5.8 are shown in Figs. 5.5 and 5.6 in the synodic system, respectively. As we can see the spacecraft is injected into the lunar trajectory and as the spacecraft approaches the Moon, it is slung around the Moon and leave with a different geocentric velocity direction and larger magnitude, all of this without requiring more Δv. Thus, the spacecraft leaves the Moon on an elliptic orbit until to intersect the semi-major or -minor axis of the elliptic orbits around L_4 and L_5 such that an impulsive thrust is applied to place it around the target point. Figures 5.7 and 5.8, that correspond to Figs. 5.5 and 5.6, respectively, show the moment when the second burn is applied. Note that Figures 5.5-5.8 only show the trajectories that reach the long period orbit because the initial conditions to guide the spacecraft to the short period orbit are practically equal as we can see in Tables 5.7 and 5.8. Finally, Figures 5.9 and 5.10 show the trajectories corresponding to Figs. 5.5 and 5.6 in the Earth-centered inertial system $\hat{\boldsymbol{n}}_{\mathbf{1}}, \hat{\boldsymbol{n}}_{\mathbf{2}}$, respectively.

Table 5.6 - Values of the apocentre d and interval for λ_0 that contains the trajectories that intersect either the long or short period orbits shown in Fig. 5.1

Center of the Elliptic Orbits	d (km)	λ_0 (degrees)
L_4	$d_{EM} - \frac{R_S}{2}$	$[10, 15]$ $[46, 47]$
L_4	d_{EM}	$[30, 31]$
L_4	$d_{EM} + \frac{R_S}{2}$	$[10, 11]$ $[16, 17]$
L_5	d_{EM}	$[7, 8]$ $[27, 28]$ $[45, 46]$
L_5	$d_{EM} + \frac{R_S}{2}$	$[8, 10]$

5.4 G Trajectories

Assuming an Earth circular parking orbit of radius r_0 and as target the elliptic orbits shown in Fig. 5.1, we have applied the first procedure described in Sect. 3.4. Using the Newton-Secant method, we have found the values for ϑ in Eq.(3.63) that solve Eq. 3.4 and will provide the most appropriated Trajectories G to reach the elliptic orbits around L_4 and L_5 separately. The search algorithm considered a set of

Table 5.7 - Apocentre d, angle λ_0, phase angle at departure γ_0, parameters that described the geometry of the swing-by, and change in velocity and energy experimented by the spacecraft after the swing-by maneuver is completed, of each trajectory for placing a spacecraft into the long and short period orbits around L_4

Period Orbit	d (km)	λ_0 (degrees)	γ_0 (degrees)	ψ (degrees)	r_p (km)	Δv (km/s)	$\Delta\varepsilon$ (km^2/s^2)
Long	$d_{EM} - \frac{R_S}{2}$	10.8	136.9	38.2	$48,075$	0.2412	0.1521
Long	$d_{EM} - \frac{R_S}{2}$	46.6	123.6	30.4	$27,336$	0.4269	0.2201
Long	d_{EM}	30.4	133.1	50.7	$22,068$	0.4426	0.3489
Long	$d_{EM} + \frac{R_S}{2}$	10.5	139.2	51.2	$36,297$	0.2570	0.2039
Long	$d_{EM} + \frac{R_S}{2}$	16.0	137.9	52.5	$30,600$	0.3033	0.2450
Short	$d_{EM} - \frac{R_S}{2}$	12.6	136.4	38.2	$46,703$	0.2488	0.1570
Short	$d_{EM} - \frac{R_S}{2}$	48.2	122.7	29.0	$27,305$	0.4282	0.2112
Short	d_{EM}	30.3	133.1	50.7	$22,178$	0.4408	0.3473
Short	$d_{EM} + \frac{R_S}{2}$	10.3	138.6	46.5	$36,541$	0.2553	0.2024
Short	$d_{EM} + \frac{R_S}{2}$	16.1	137.9	52.5	$30,464$	0.3046	0.2462

initial conditions as defined in Eqs. (3.59)-(3.61), but with the v_0 obtained from the small variations in ϑ in Eq. (3.63). From each initial condition, the search algorithm integrates a trajectory in the direction of the Moon in such a way that it enters the lunar sphere of influence and passes by either the Moon's trailing side to reach a vicinity of L_4 or the Moon's leading side to reach a vicinity of L_5, selecting finally the trajectory with the lowest Δv_T that intersects the spacecrafts into the semi-major axis of the elliptical target orbits. Tables 5.13 and 5.14 show the values of the term ϑ, initial impulsive thrust Δv_1, stabilizing impulsive thrust Δv_2, total cost Δv_T, time of flight Δt spent of these missions, as well as the angle Φ between the transfer trajectories periselenium vector, $\boldsymbol{r_p}$, and the x axis of the synodic frame that unites the Earth to the Moon for those trajectories with the lowest Δv_T. Note that the difference between the first impulsive thrust made for L_4 and L_5 mission is very small (≈ 0.5 m/s). This shows how sensitive is the behaviour of the G trajectories

Table 5.8 - Apocentre d, angle λ_0, phase angle at departure γ_0, parameters that described the geometry of the swing-by, and change in velocity and energy experimented by the spacecraft after the swing-by maneuver is completed, of each trajectory for placing a spacecraft into the long and short period orbits around L_5

Period Orbit	d (km)	λ_0 (degrees)	γ_0 (degrees)	ψ (degrees)	r_p (km)	Δv (km/s)	$\Delta\varepsilon$ (km^2/s^2)
Long	d_{EM}	7.7	137.1	47.4	$35,540$	0.2868	0.2151
Long	d_{EM}	27.4	134.0	49.8	$24,833$	0.4001	0.3113
Long	d_{EM}	45.7	128.3	59.8	$9,311$	0.8061	0.7098
Long	$d_{EM} + \frac{R_S}{2}$	9.8	139.4	51.0	$37,064$	0.2518	0.1992
Short	d_{EM}	6.8	139.4	45.9	$42,282$	0.2297	0.1681
Short	d_{EM}	27.5	133.9	49.9	$24,723$	0.4016	0.3127
Short	d_{EM}	45.6	128.3	59.8	$9,139$	0.8057	0.7093
Short	$d_{EM} + \frac{R_S}{2}$	10.0	139.3	51.0	$36,852$	0.2532	0.2005

with respect to small variations in the initial velocity in the Earth-Moon system. Initial position and velocity coordinates (referred to the non-dimensional rotating frame system) corresponding to departure parameters described in Tables 5.13 and 5.14 are presented in Tables 5.15 and 5.16, respectively.

Figure 5.11 show the Trajectories G with lowest Δv_T, their energies relative to the Earth as a function of the time and the magnitudes of their velocities in the geocentric and synodic coordinates systems for L_4 (left column) and L_5 (right column) missions, respectively. Again, we have only considered the trajectories to the long period since the qualitative behaviour between the trajectories that reach the long and short period orbits is the same. Regarding the trajectories, a $\Delta\vartheta \approx 0.5$ m/s is sufficient to produce a trajectory that passes by the Moon's trailing side (mission to L_4) and another by the Moon's leading side (mission to L_5). This difference is crucial with respect to the spacecrafts' energy variations relative to the Earth with the swing-by. These energies, shown in dimensionless units, were computed from the osculating Keplerian orbits of the transfer trajectories to L_4 and L_5 Lagrangian points. In other words, from the vis-viva equation and the dynamics of the two-body

Table 5.9 - Impulsive thrust Δv_1, impulsive stabilizing thrust Δv_2, total cost Δv_T and time of flight Δt of each trajectory for placing a spacecraft into the long and short period orbits around L_4

Period Orbit	d (km)	λ_0 (degrees)	Δv_1 (km/s)	Δv_2 (km/s)	Δv_T (km/s)	Δt (days)
Long	$d_{EM} - \frac{R_S}{2}$	10.8	3.0752	0.7133	3.7885	26.0
Long	$d_{EM} - \frac{R_S}{2}$	46.6	3.0752	0.6960	3.7712	27.0
Long	d_{EM}	30.4	3.0840	0.8257	3.9097	29.0
Long	$d_{EM} + \frac{R_S}{2}$	10.5	3.0914	0.9167	4.0081	28.0
Long	$d_{EM} + \frac{R_S}{2}$	16.0	3.0914	0.9168	4.0082	53.0
Short	$d_{EM} - \frac{R_S}{2}$	12.6	3.0752	0.7207	3.7959	26.0
Short	$d_{EM} - \frac{R_S}{2}$	48.2	3.0752	0.7210	3.7962	27.0
Short	d_{EM}	30.3	3.0840	0.8212	3.9052	29.0
Short	$d_{EM} + \frac{R_S}{2}$	10.3	3.0914	0.9124	4.0038	28.0
Short	$d_{EM} + \frac{R_S}{2}$	16.1	3.0914	0.9125	4.0039	53.0

Earth-particle problem (SCHAUB; JUNKINS, 2003). Still with reference to the second row of Fig. 5.11, note that the variation of the energy relative to the Earth for L_4 transfer trajectory is positive, since $\Phi = 209.8°$, which corresponds to a periselenium behind the Moon relative to the Earth, in synodic frame, as described in Fig.3.15. Additionally, after the swing-by maneuver, the energy of the spacecraft is positive; therefore, its trajectory can escape from the Earth-Moon system. In the case of L_5 mission, the change in energy of the transfer trajectory relative to the Earth is negative and its magnitude is much smaller than the change computed for the transfer trajectory of L_4 mission. This is because the change in energy is proportional to $\sin \Phi$ (BROUCKE, 1988). For L_5 transfer trajectory, $\Phi = 179°$, and for L_4 transfer trajectory, $\Phi = 209.8°$; which implies in the smaller variation of the energy for L_5 trajectory and in the bigger variation for the trajectory of L_4 mission.

In the third row of Fig. 5.11, we can see the magnitude of the velocities of the

Table 5.10 - Impulsive thrust Δv_1, impulsive stabilizing thrust Δv_2, total cost Δv_T and time of flight Δt of each trajectory for placing a spacecraft into the long and short period orbits around L_5

Period Orbit	d (km)	λ_0 (degrees)	Δv_1 (km/s)	Δv_2 (km/s)	Δv_T (km/s)	Δt (days)
Long	d_{EM}	7.7	3.0840	0.8260	3.9100	9.0
Long	d_{EM}	27.4	3.0840	0.8257	3.9097	35.0
Long	d_{EM}	45.7	3.0840	0.8256	3.9096	63.0
Long	$d_{EM} + \frac{R_S}{2}$	9.8	3.0914	0.9167	4.0081	34.0
Short	d_{EM}	6.8	3.0840	0.8227	3.9097	9.0
Short	d_{EM}	27.5	3.0840	0.8213	3.9053	35.0
Short	d_{EM}	45.6	3.0840	0.8200	3.9040	63.0
Short	$d_{EM} + \frac{R_S}{2}$	10.0	3.0914	0.9124	4.0038	34.0

spacecraft in the geocentric and synodic frame. Note that, in the case of L_4 transfer trajectory, it is observed an increment in the velocity of the spacecraft relative to the Earth after the swing-by maneuver, whereas for the L_5 transfer trajectory is observed a decrease in velocity as expected. However, the magnitude of the velocities for each trajectory in the synodic frame varies very little after the swing-by. This can explain, in a simple way, why the change in velocity Δv_2 required to place the spacecraft into the periodic orbits around L_4 and L_5 is practically the same. They need to be practically stopped in this frame.

Figures 5.12(a) and 5.12(b) show the instant when the spacecraft intersects the semi-major axis of the long period orbits around L_4 and L_5, respectively, and a second thrust is made such that the spacecraft can be placed around L_4 and L_5, respectively.

Missions with multiple objectives can also be exploited considering the Trajectories G and their inherent instability, for example, using only a launcher to deliver spacecrafts to L_4 and L_5. In this scenery, two spacecrafts follow coupled as far as the apogee of a G Trajectory, in general, it is located between $540,000$ and $600,000$ km from the Earth. In the apogee, the spacecrafts are separated. So one of them

Table 5.11 - Initial position and velocity coordinates for placing a spacecraft into the long and short period orbits around L_4 (referred to the non-dimensional rotating frame system) corresponding to departure geometries described in Table 5.9

Period Orbit	d (km)	λ_0 (degrees)	x_0	y_0	$\dot{x}_0$	$\dot{y}_0$
Long	$d_{EM} - \frac{R_S}{2}$	10.8	-0.0250109	-0.0120353	7.1556091	-7.6466507
Long	$d_{EM} - \frac{R_S}{2}$	46.6	-0.0218972	-0.0146713	8.7227976	-5.7954129
Long	d_{EM}	30.4	-0.0241850	-0.0128612	7.6529217	-7.1614775
Long	$d_{EM} + \frac{R_S}{2}$	10.5	-0.0254835	-0.0115095	6.8533019	-7.9396266
Long	$d_{EM} + \frac{R_S}{2}$	16.0	-0.0252190	-0.0118091	7.0316668	-7.7820999
Short	$d_{EM} - \frac{R_S}{2}$	12.6	-0.0249054	-0.0121471	7.2220654	-7.5839158
Short	$d_{EM} - \frac{R_S}{2}$	48.2	-0.0216655	-0.0148226	8.8127519	-5.6576862
Short	d_{EM}	30.3	-0.0241850	-0.0128612	7.6529217	-7.1614775
Short	$d_{EM} + \frac{R_S}{2}$	10.3	-0.0253623	-0.0116485	6.9360682	-7.8674250
Short	$d_{EM} + \frac{R_S}{2}$	16.1	-0.0252190	-0.0118091	7.0316668	-7.7820999

follows its way to one of the previously chosen point, L_5, for instance, while the other one receives a small Δv that will put it in direction to L_4 after a swing-by with the Moon. This is possible due to the instability of the Trajectories G and the small magnitudes of the spacecrafts' velocities (of the order of 0.150 km/s) when they reach the apogee of a G Trajectory prior the passage through the lunar sphere of influence.

We present a study about this sort of mission considering the same G Trajectory shown in Fig. 5.12 (first row, right column). That is, considering to send a spacecraft to L_5 directly. However, now, it will guide two spacecrafts with equal masses up to its apogee. In this case, the apogee is located $557,029.68$ km from the Earth. It is reached in 8.74 days after the departure from Low Earth Orbit (LEO) and with velocity of 0.145 km/s. After the separation, the first spacecraft follows its way to L_5, and the second one receives a small $\Delta v = 0.027$ km/s to change its velocity

Table 5.12 - Initial position and velocity coordinates for placing a spacecraft into the long and short period orbits around L_5 (referred to the non-dimensional rotating frame system) corresponding to departure geometries described in Table 5.10

Period Orbit	d (km)	λ_0 (degrees)	x_0 (km/s)	y_0 (km/s)	$\dot{x}_0$ (km/s)	$\dot{y}$ (days)
Long	d_{EM}	7.7	-0.0250528	-0.0119904	7.1347202	-7.6778733
Long	d_{EM}	27.4	-0.0243855	-0.0126706	7.5394900	-7.2808009
Long	d_{EM}	45.7	-0.0230666	-0.0138232	8.2253389	-6.4959812
Long	$d_{EM} + \frac{R_S}{2}$	9.8	-0.0255236	-0.0114629	6.8255456	-7.9635007
Short	d_{EM}	6.8	-0.0255236	-0.0114629	6.8208456	-7.9580171
Short	d_{EM}	27.5	-0.0243634	-0.0126920	7.5521859	-7.2676309
Short	d_{EM}	45.6	-0.0230666	-0.0138232	8.2253389	-6.4959812
Short	$d_{EM} + \frac{R_S}{2}$	10.0	-0.0255036	-0.0114862	6.8394342	-7.951576

vector, because it must pass by the Moon 2.5 hours after the first one to guarantee a swing-by with energy increment. Figure 5.13 shows the G Trajectory up to the apogee and the trajectories followed by each spacecraft after the separation in a geocentric coordinate system. Note that only $\Delta v_1 = 3.1124$ km/s is applied to put the spacecrafts (coupled) into the G Trajectory. To insert the first spacecraft around L_5 is required a $\Delta v_2 = 1.1370$ km/s, and a $\Delta v_2 = 1.1412$ km/s to insert the second around L_4 (plus $\Delta v = 0.027$ km/s to change its velocity vector at the apogee).

In this way, G Trajectories open the possibility of planning missions with multiple objectives and reduction in launch costs. In addition to the mission that we have just described, there are other possibilities, for example, the use of the same launcher to send spacecrafts to the Lagrangian equilibrium points and the Moon, or back to the Earth (MELO et al., 2007), (MELO et al., 2009). These types of missions are not possible starting from conventional transfers as Patched-conic or Hohmann-like (minimum energy ellipse).

In real missions, in which the Sun's gravitational field, the solar radiation pressure and other perturbations act on the spacecrafts continuously, the application of

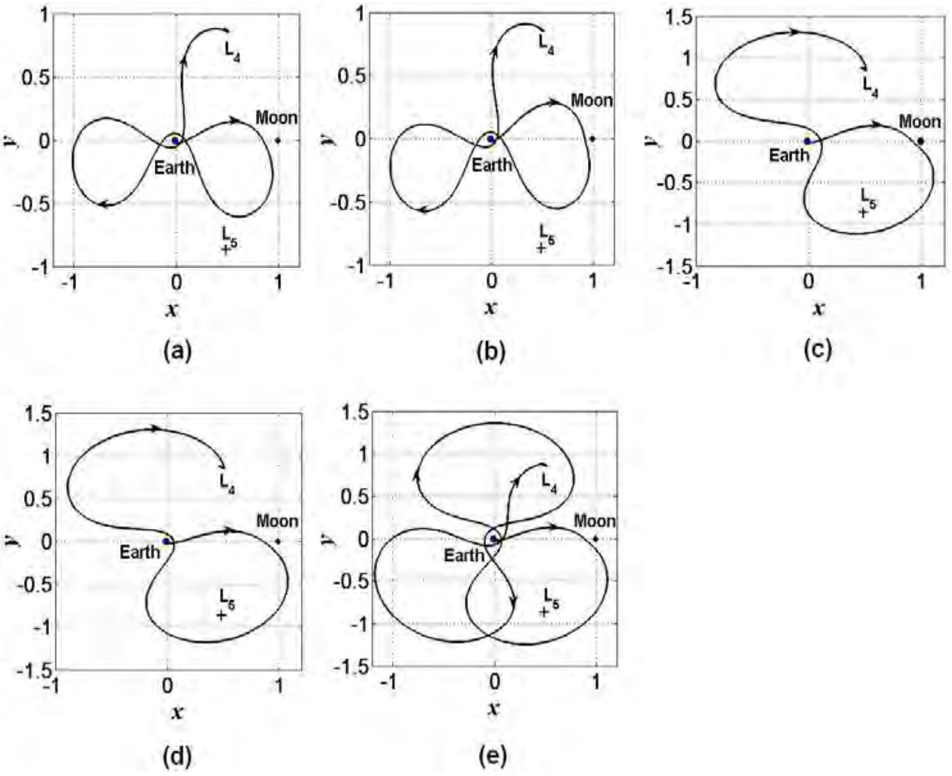

Figure 5.5 - Swing-By maneuver to reach the long period orbit around L_4 in the synodic system. The apocentre of the geocentric departure orbit and the angle at which it intersects the lunar sphere of influence are: (a) $d = d_{EM} - R_S/2$, $\lambda_0 = 10.8°$, (b) $d = d_{EM} - R_S/2$, $\lambda_0 = 40.6°$, (c) $d = d_{EM}$, $\lambda_0 = 30.4°$, (d) $d = d_{EM} + R_S/2$, $\lambda_0 = 10.5°$, and (e) $d = d_{EM} + R_S/2$, $\lambda_0 = 16.0°$.

small Δv in the apogee of the G Trajectories must be considered to correct these trajectories in order to minimize the fuel consumption.

5.5 Targeting Chaotic Orbits to the equilibrium points L_4 and L_5 through recurrence

Using Eqs. (3.65)-(3.67) and the electric propulsion parameters given in Table 3.1 (F = 120 mN, I_{sp} = 1600 s), the final spacecraft mass m_f, consumed propellant mass $\Delta m = m_0 - m_f$, transfer time Δt_1 and number of spacecraft orbits $\mathcal{N}$ are computed for different initial mass values m_0 an the results are shown in Table 5.17.

Notice that a small spacecraft with 300 kg or 400 kg of total mass could be transferred to a higher orbit of radius $r_f = 59,669$ km in five months approximately. This transfer time is compatible with a real mission. Additionally, if the initial mass m_0 is between these values, the final spacecraft mass will be between 200 kg and 300 kg, this quantity of mass is enough to use chemical propulsion. Remember that the

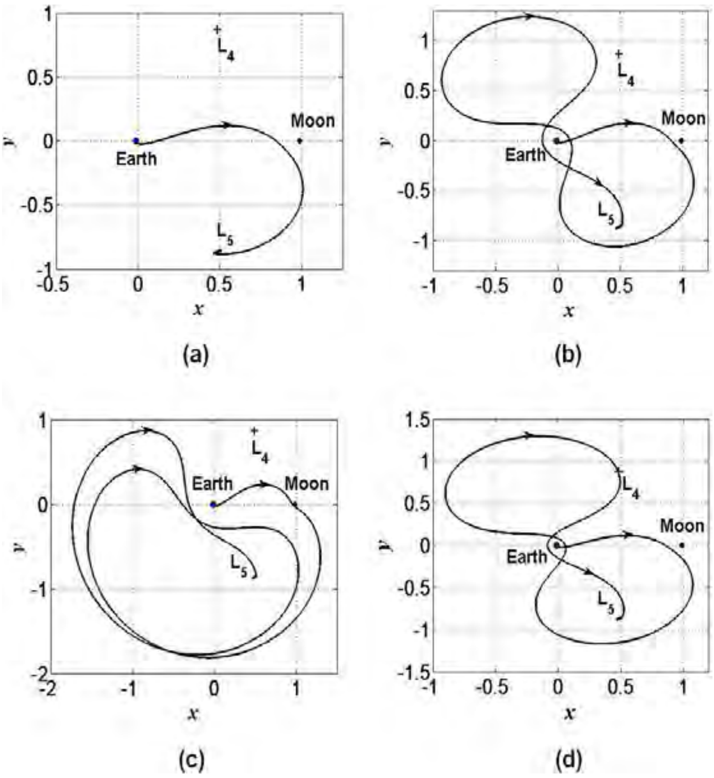

Figure 5.6 - Swing-By maneuver to reach the long period orbit around L_5 in the synodic system. The apocentre of the geocentric departure orbit and the angle at which it intersects the lunar sphere of influence are: (a) $d = d_{EM}$, $\lambda_0 = 7.7°$, (b) $d = d_{EM}$, $\lambda_0 = 27.4°$, (c) $d = d_{EM}$, $\lambda_0 = 45.7°$, (d) $d = d_{EM} + R_S/2$, $\lambda_0 = 9.8°$.

spacecraft uses a hybrid propulsion system, where the first part of the mission was made using electric propulsion, but once the spacecraft has reached the altitude of $59,669$ km, a chemical propulsion is used to inject the spacecraft into the chaotic region (see Fig. 3.16).

Now to find the recurrent loops in the Poincaré section of the chaotic trajectory shown in Fig. 3.19 we have fixed $\epsilon = 0.05$ and applied the algorithm described in Fig. 3.21 in orbit $z_i = (x_i, \dot{x}_i)$ (see Eq. (3.71)). Three recurrent loops were found, which were removed achieving a 31 iterate pseudo-orbit and requiring a maximum perturbation of 0.2705 km/s as shown in Table 5.18. The chaotic trajectory shown in Fig. 3.17 and its corresponding controlled chaotic trajectory, plotted in the synodic system x, y are shown in Fig. 5.14.

Thus, starting from circular Earth orbit $59,669$ km above the Earth's center, a first impulsive thrusts is applied to inject the spacecraft into the chaotic region with $C = 3.17948$. The chaotic transfer requires an initial change in velocity of $\Delta v_1 = 0.7444$

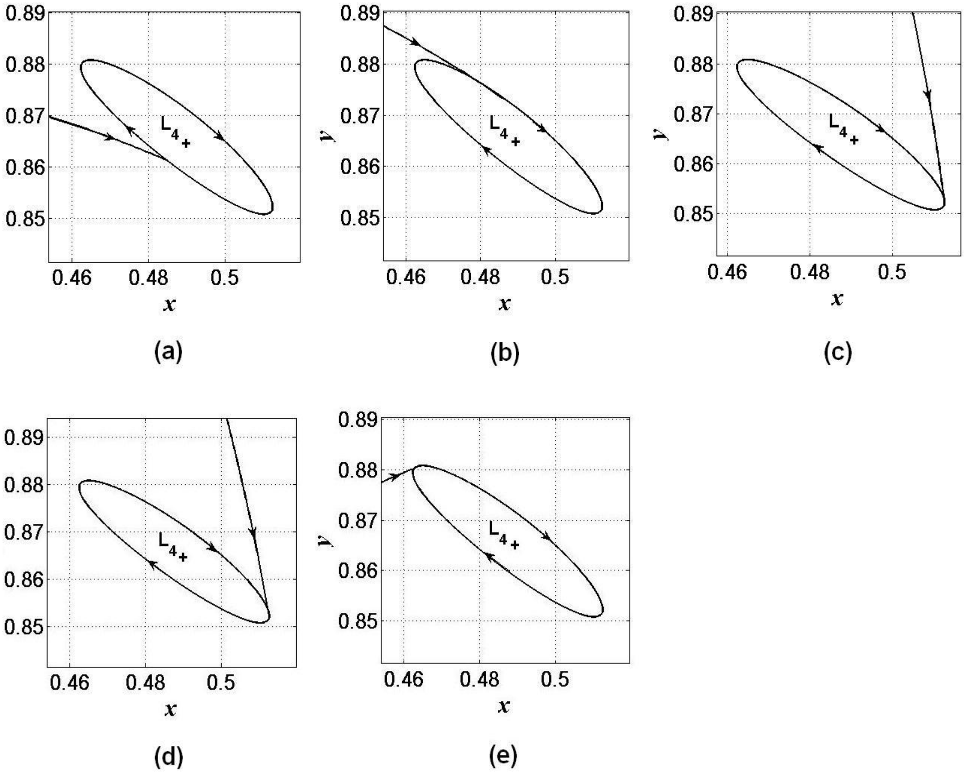

Figure 5.7 - Trajectories corresponding to Fig. 5.5 intersecting the semi-minor axis of the elliptic orbit. At that moment it is applied the stabilizing impulsive thrust to place the spacecraft around the equilibrium points.

Table 5.13 - Term ϑ, impulsive thrust Δv_1, stabilizing impulsive thrust Δv_2, total cost Δv_T, time of flight Δt and angle Φ of each trajectory for placing a spacecraft into the long and short period orbits around L_4

Period Orbit	ϑ (km/s)	Δv_1 (km/s)	Δv_2 (km/s)	Δv_T (km/s)	Δt (days)	ψ (degrees)
Long	1.418837×10^{-2}	3.1129	1.1412	4.2541	18.2	209.8
Short	1.418636×10^{-2}	3.1129	1.1352	4.2481	18.2	209.8

km/s. Additionally, six perturbations are made to reduce the flight time. The total thrust required for controlling the chaotic trajectory is $(\sum \Delta u_1 + \sum \Delta u_2) = 0.5075$ km/s. The overall thrust requirement for this chaotic orbit transfer is

$$\Delta v_1 + \sum \Delta u_1 + \sum \Delta u_2 \;\; = \;\; 1.2519 \;\frac{\mathrm{km}}{\mathrm{s}}. \qquad (5.1)$$

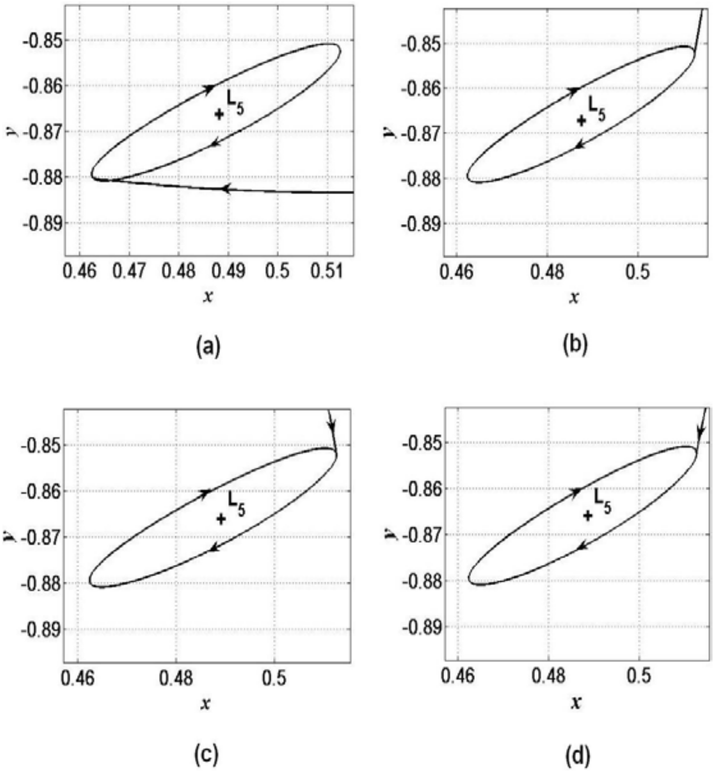

(a) (b) (c) (d)

Figure 5.8 - Trajectories corresponding to Fig. 5.6 intersecting the semi-minor axis of the elliptic orbit. At that moment it is applied the stabilizing impulsive thrust to place the spacecraft around the equilibrium points.

Table 5.14 - Term ϑ, impulsive thrust Δv_1, stabilizing impulsive thrust Δv_2, total cost Δv_T, time of flight Δt and angle Φ of each trajectory for placing a spacecraft into the long and short period orbits around L_5

Period Orbit	ϑ (km/s)	Δv_1 (km/s)	Δv_2 (km/s)	Δv_T (km/s)	Δt (days)	ψ (degrees)
Long	1.372652×10^{-2}	3.1124	1.1370	4.2494	18.7	179.0
Short	1.372543×10^{-2}	3.1124	1.1350	4.2474	18.6	179.0

Using the resulting trajectory, the spacecraft reaches the Moon after 311 days, which is approximately 40% of the transfer time obtained by E. M. Bollt and James D. Meiss (BOLLT; MEISS, 1995b).

The final position of the chaotic trajectory in the phase space $(x, y, \dot{x}, \dot{y})$ is

$$(x_N, y_N, \dot{x}_N, \dot{y}_N) = (0.981417, 0, -0.303013, -1.859802)\,. \tag{5.2}$$

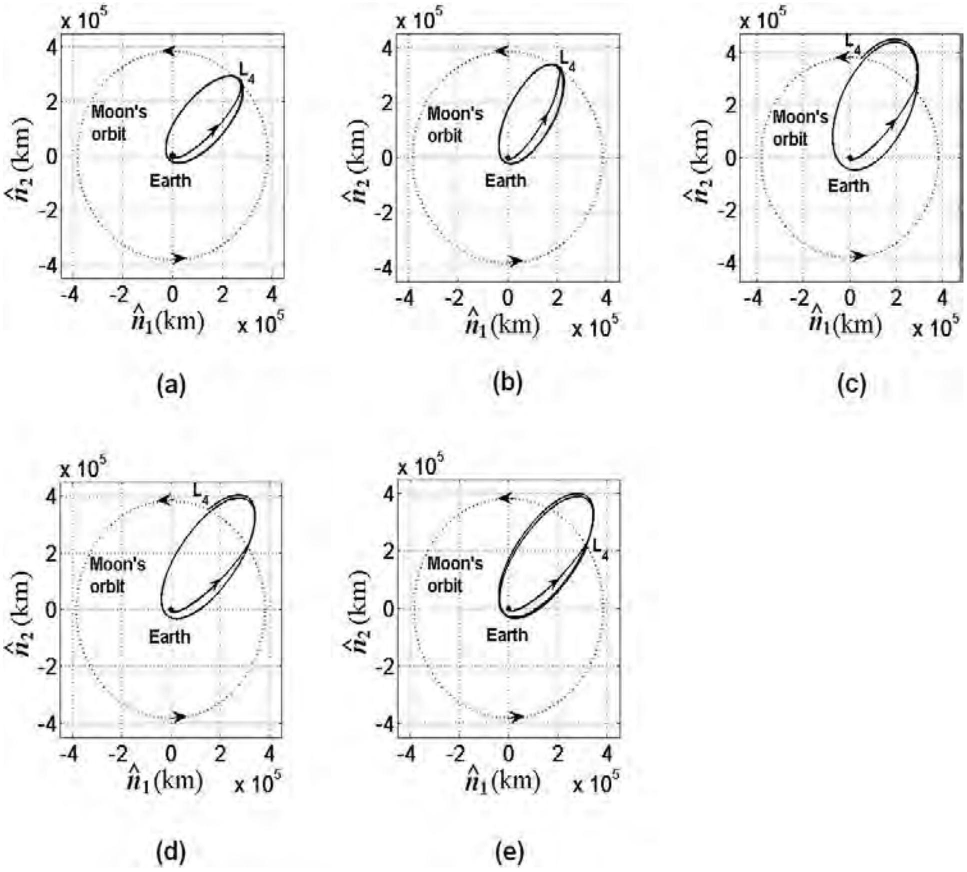

Figure 5.9 - Trajectories corresponding to Fig. 5.5 in the Earth-centered inertial system $\hat{\boldsymbol{n}}_{\boldsymbol{1}}, \hat{\boldsymbol{n}}_{\boldsymbol{2}}$.

Table 5.15 - Initial position and velocity coordinates for placing a spacecraft into the long and short period orbits around L_4 (referred to the non-dimensional rotating frame system) corresponding to departure geometries described in Table 5.13

Period Orbit	x	y	$\dot{x}_0$	$\dot{y}_0$
Long	0.0054646	0.0	0.0	10.5093303
Short	0.0054646	0.0	0.0	10.5093303

In this manner, a change in velocity $\Delta \boldsymbol{u_N}$ is necessary for arriving at equilibrium points as shown in Sect. 3.5.4. The change in velocity is parallel to the velocity component $\dot{y}_N$ as shown in Fig. 3.25. Therefore, applying Eq. (3.83) in the final position (5.2), Tables 5.19 and 5.20 show the magnitude of the the required boost Δu_N, the correction term ς and the time of flight Δt_2 since the change in velocity is applied until to reach the periodic orbits around L_4 and L_5, respectively.

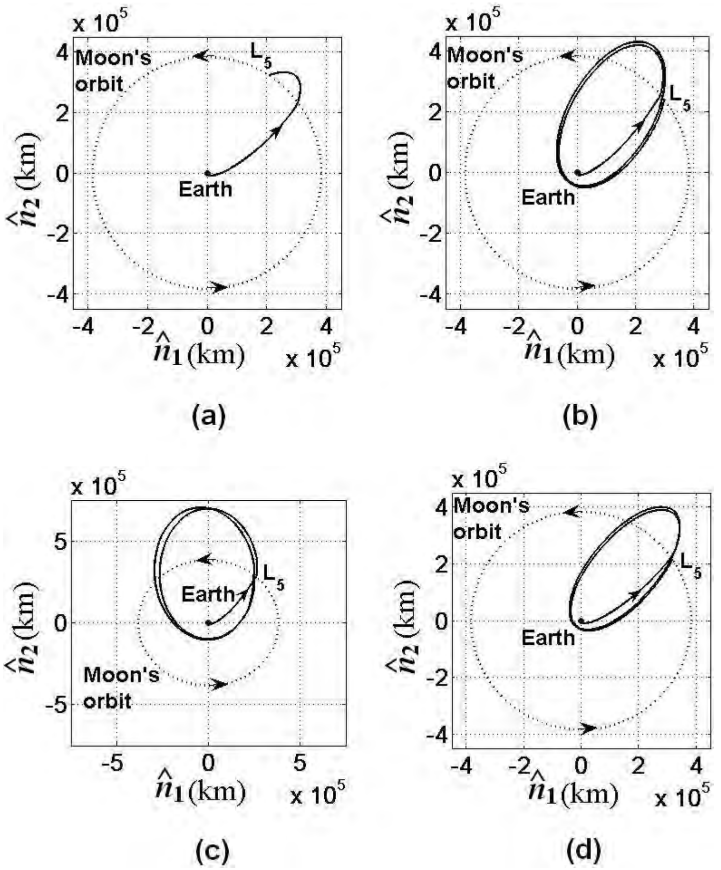

Figure 5.10 - Trajectories corresponding to Fig. 5.6 in the Earth-centered inertial system $\hat{\boldsymbol{n}}_1, \hat{\boldsymbol{n}}_2$.

Table 5.16 - Initial position and velocity coordinates for placing a spacecraft into the long and short period orbits around L_5 (referred to the non-dimensional rotating frame system) corresponding to departure geometries described in Table 5.14

Period Orbit	x	y	$\dot{x}_0$	$\dot{y}_0$
Long	0.0054646	0.0	0.0	10.5088423
Short	0.0054646	0.0	0.0	10.5088423

When the spacecraft arrives near the Lagrangian point, an stabilizing impulsive thrust Δv_2 is required to placed the spacecraft into the elliptic orbits around equilibrium points. The final transfer trajectories as well as the instant when the spacecraft intersects the semi-major axis of the long period orbits around L_4 (left column) and L_5 (right column) are shown in Fig. 5.15. Thus, the stabilizing impulsive thrust Δv_2, the total cost Δv_T and the transfer time $\Delta t = \Delta t_1 + \Delta t_2$ since the first impulse is

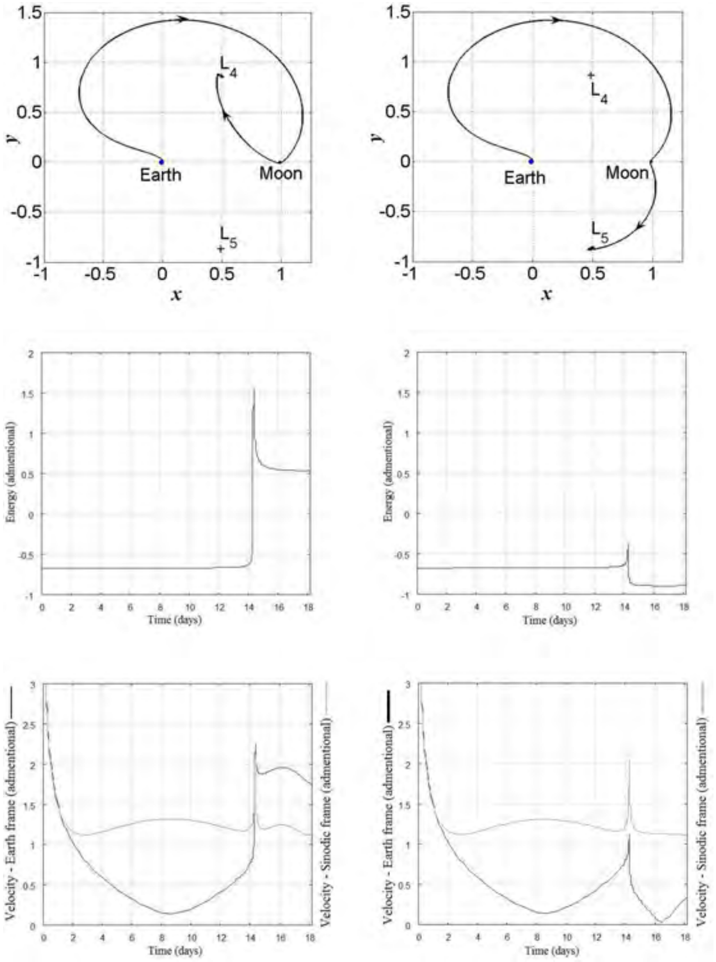

Figure 5.11 - Spacecrafts' transfer trajectories, energy variations relative to the Earth as a function of the time and velocities in the geocentric and synodic coordinates systems also as a function of the time for L_4 mission (left column) and for L_5 mission (right column).

applied until to reach the elliptic orbits around L_4 and L_5 are shown in Tables 5.21 and 5.22, respectively.

Finally, suppose that a small spacecraft with 300 kg of total mass will be transferred from a LEO with an altitude of 400 km to the Lagrangian point L_4. Using the strategy proposed in this work, the spacecraft will reach an altitude of $59,669$ km with a final mass $m_f = 216.91$ kg (see Table 5.17). In this first part, the electric propulsion is used and the time of flight will be 126 days. Now, suppose that the specific impulse for the chemical thruster is 300 s (a value achievable with this technology). After the use of chemical propulsion to inject the spacecraft into the chaotic region and direct the spacecraft to the long period orbit around L_4, the time of flight for this chaotic transfer will be 342 days. In this manner, assuming a structural mass of

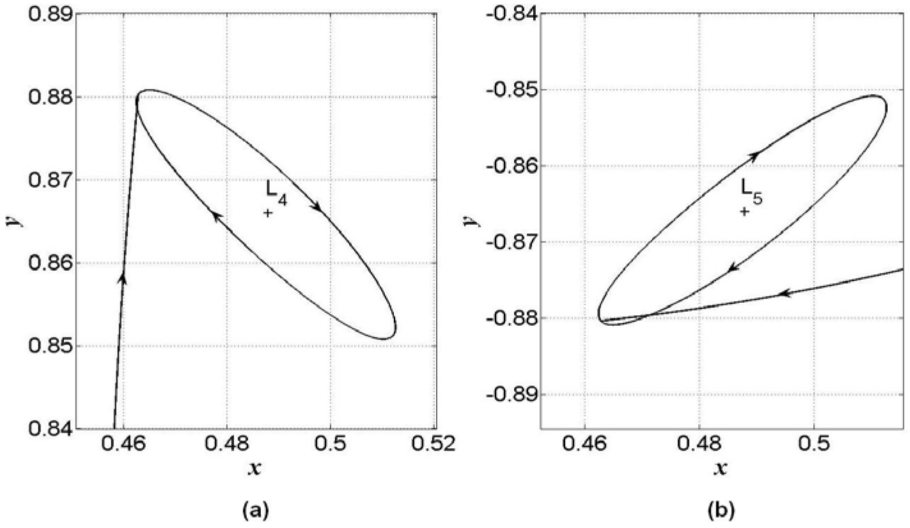

Figure 5.12 - Trajectories corresponding to Fig. 5.11 intersecting the semi-major axis of the elliptic orbit. At that moment it is applied the stabilizing impulsive thrust to place the spacecraft around (a) L_4 and (b) L_5.

25 kg (approx. 15% of the propellant mass), a small spacecraft with 300 kg of total mass and 100 kg of payload could be transferred to the Lagrangian equilibrium point L_4 spending 170 kg of propellant mass and a time of flight of 468 days (1.28 years). In contrast, chemical propulsion requires two boosts of $\Delta v_1 = 4.1$ km/s to place the spacecraft into the chaotic region from a LEO (MELO et al., 2007) and a total change in velocity of $\Delta v_T = 0.7699$ km/s (see Tables 5.21) to direct the spacecraft to the Lagrangian point L_4 through the connected chaotic component between the Earth and Moon. Therefore, the total boost required for this transfer will be 4.8699 km/s. Assuming an spacecraft with the same characteristics described previously, Equations (3.64)-(3.65) show that the maximum payload mass should be 30 kg. In other words, combining electric and chemical propulsion we are able to transfer 70 kg more payload.

5.6 The Zero Relative Acceleration Lines in a Long and Short Period Family

In this section we have determined the existence of the Zero Relative Acceleration Lines (ZRRAL) along periodic orbits around L_4. The existence of the ZRRAL along any nominal trajectory is determined by the sign of the discriminant of the sub-matrix F in Eq. (4.3) which represents, in general, a quadratic form. If the discriminant of F is negative at a certain point of the nominal trajectory, therefore the ZRRAL at this point is represented by an ellipse of radius zero, i.e. there is no region

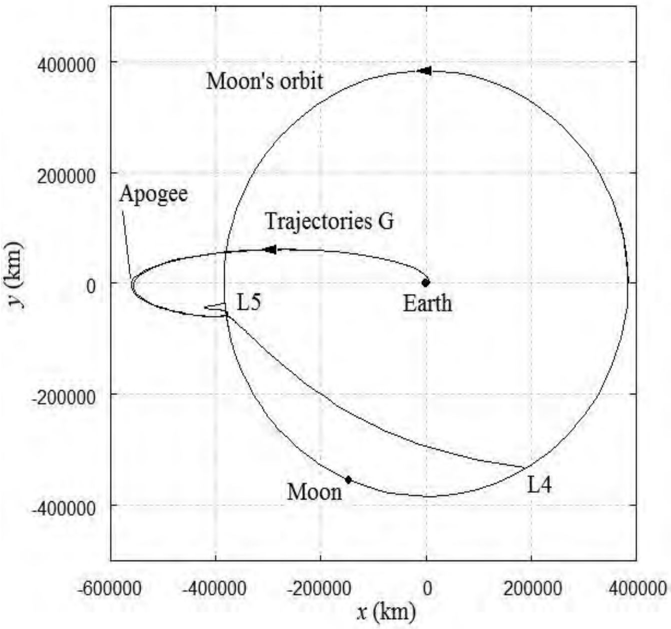

Figure 5.13 - The same initial path of the previously G-trajectory (that appears here in geocentric reference coordinate system) can be used to place a spacecraft into periodic orbits around L_4 or L_5. As so, if an appropriate low thrust is applied in the apogee of this G-trajectory, the spacecraft ends up of in L_4 or in L_5. Both situations are depicted here. Observe in the last row of Fig. 5.11, also in geocentric system, the large difference between the spacecrafts' velocities after the swing-by.

with Zero Relative Radial Acceleration (ZRRA). Otherwise, the ZRRA at this point is represented by two lines (in the planar case).

Firstly, we begin by computing the value of the discriminant of the sub-matrix F associated to the points $X_h(t)$ along the long and short period orbits shown in Figs. 5.1(a) and 5.1(b), respectively. As we can see in Fig. 5.16, the sign of the discriminant in both trajectories are negative for every point $X_h(t)$, this means that there are no regions with ZRRA along these specific periodic orbits.

The previous fact can be verified when we compute numerically the ZRRA at some points on these periodic orbits. Thus considering a sphere of radius s equal to 1 km (see Fig. 4.3), the first row of Figure 5.17 shows the scalar product between the relative acceleration $\boldsymbol{a}(t,\theta)$ and vector $\boldsymbol{s}(\theta)$ as a function of angle θ at three different points $X_h(t)$ along the long period orbit, where $t = 22, 45$ and 68 days. Similarly, the second row of Figure 5.17 shows the scalar product at three different points $X_h(t)$ along the short period orbit, where $t = 7, 14$ and 22 days.

Table 5.17 - Parameters of a low-thrust transfer between two circular Earth orbits of radius $r_0 = 6,771$ km and $r_1 = 59,669$ km, and using electric propulsion with continuous constant acceleration ($F = 160$ mN, $I_sp = 1600$ s)

m_0 (kg)	m_f (kg)	Δm (kg)	Δt_1 (days)	$\mathcal{N}$
200	144.61	55.39	84	519
250	180.76	69.24	105	649
300	216.91	83.09	126	779
350	256.06	93.94	147	909
400	289.22	110.78	168	1039
450	325.37	124.63	189	1169
500	361.52	138.48	210	1268

Table 5.18 - Perturbations Δu_i required for removing the three recurrent loops found between the iterates z_i and z_{i+s} in the chaotic orbit (3.71)

i	$i+s$	m	n	Δu_1 (km/s)	Δu_2 (km/s)
1	577	0	1	0.00741	0.08560
578	669	0	5	0.10353	0.27591
686	696	5	2	0.00234	0.03268

Now, if we make a zoom around the maximum point of each dot product function corresponding to Fig. 5.17, the scalar product function between the relative acceleration and relative position vectors never crosses the horizontal axis for any angle θ at each of these three points $X_h(t)$ as we can see in Fig. 5.18. Therefore, the radial component of the relative acceleration $\boldsymbol{a}(t,\theta)$ is different from zero for any angle θ at each of these three points. In this part it is important to comment that the dot product computed in this work is dimensionless because we are using the normalized

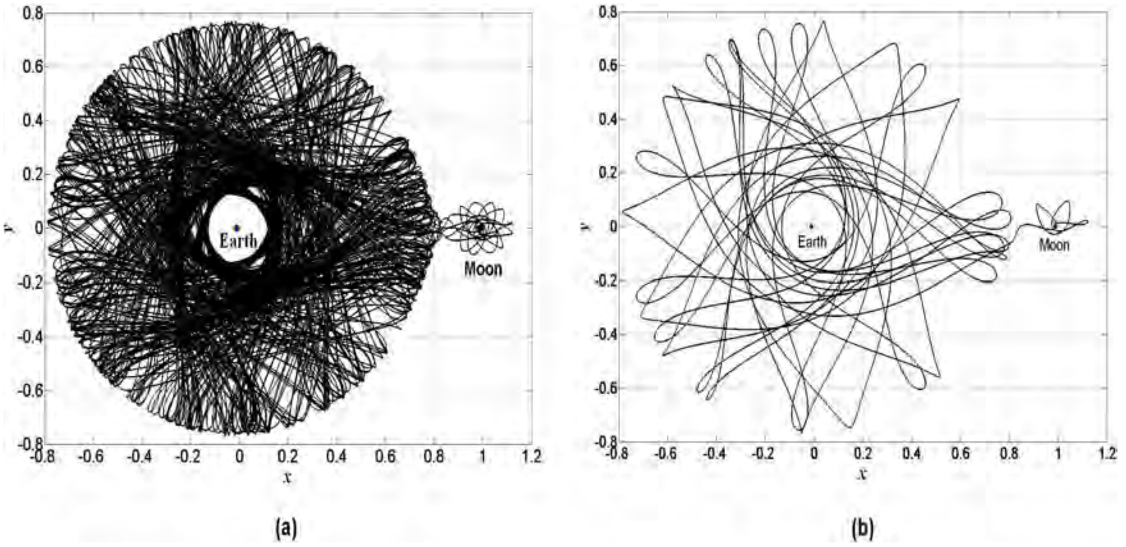

(a)

(b)

Figure 5.14 - (a) Chaotic trajectory and (b) Controlled chaotic trajectory to the Moon starting from a circular parking orbit 59, 669 km above the Earth's center (time required for transfer: 311 days).

Table 5.19 - Required boost Δu_N, correction term ς and time of flight Δt_2 since the change in velocity is applied until to reach the periodic orbits around L_4

Period Orbit	ς (km/s)	Δu_N (km/s)	Δt_2 (days)
Long	1.04076×10^{-2}	0.06222	30.9
Short	1.04267×10^{-2}	0.06224	30.9

system. If we want to obtain the scalar product in units of time and length, i.e. meters and second, we have to multiply the previous results by a factor of 1.0469×10^6 m/s^2. In any the case, the qualitative behavior of the scalar product function shown in Fig. 5.17 will remain the same. Additionally, in Fig. 5.17 we can see that the scalar product function is periodic (period equal to 180°) and has two maxima and two minima. Thus, the radial component of the relative acceleration $\boldsymbol{a}(t, \theta)$ has also two maxima and two minima at the same previous optimal values of θ. In Fig. 5.19 we show the angle θ for each point $X_h(t)$ where the relative radial acceleration has a maximum and minimum value along the long (first row) and short (second row) period orbits shown in Fig. 5.1.

In this manner, from this first case, we can affirm that there is no regions with ZRRA

Table 5.20 - Required boost Δu_N, correction term ς and time of flight Δt_2 since the change in velocity is applied until to reach the periodic orbits around L_5

Period	ς	Δu_N	Δt_2
Orbit	(km/s)	(km/s)	(days)
Long	2.54958×10^{-2}	0.07731	58.6
Short	2.55234×10^{-2}	0.07733	58.6

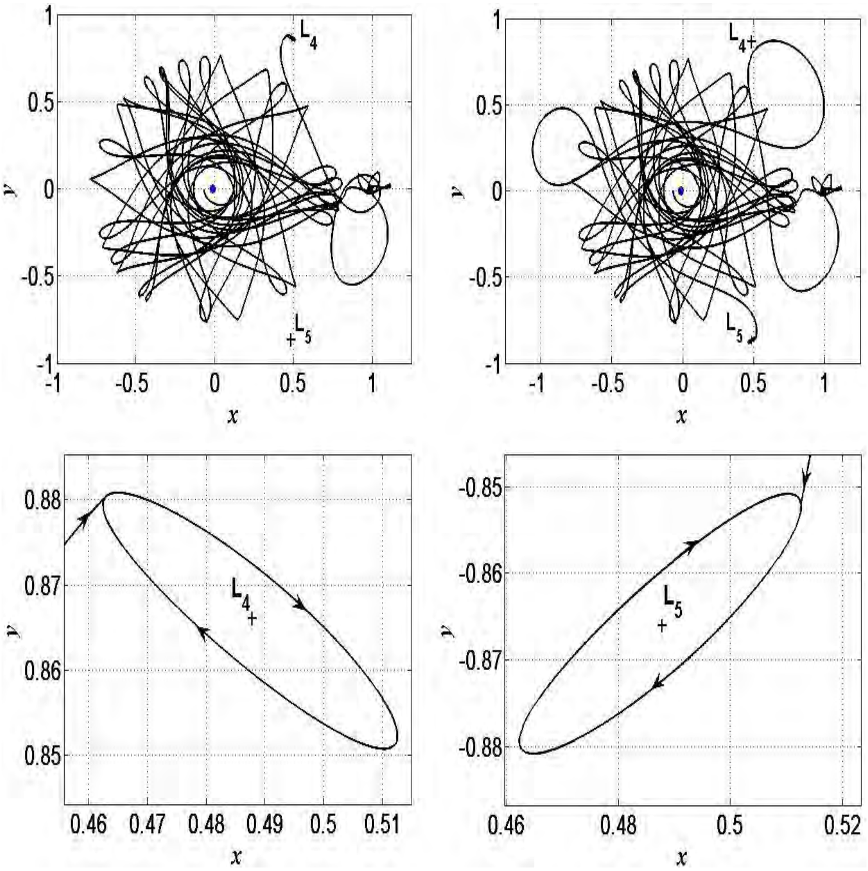

Figure 5.15 - Final trajectory arriving at Lagrangian points L_4 (left column) and L_5 (right column). The time required for L_4 and L_5 transfer is 342 and 370 days, respectively.

along the periodic orbits that are close enough to L_4. The next step, therefore, is to explore the existence of regions with ZRRA along periodic orbits that are farther from L_4. Remember that the transfer methods implemented in this work could also be used to guide the spacecrafts to this kind of orbits.

Table 5.21 - Stabilizing impulsive thrust Δv_2, total cost Δv_T and transfer time $\Delta t = \Delta t_1 + \Delta_2$ since the first impulse is applied until to reach the elliptic orbits around L_4

Period Orbit	Δv_2 (km/s)	Δv_T (km/s)	Δt (days)
Long	0.2002	1.5143	342
Short	0.1948	1.5089	342

Table 5.22 - Stabilizing impulsive thrust Δv_2, total cost Δv_T and transfer time $\Delta t = \Delta t_1 + \Delta_2$ since the first impulse is applied until to reach the elliptic orbits around L_5

Period Orbit	Δv_2 (km/s)	Δv_T (km/s)	Δt (days)
Long	0.3150	1.6442	370
Short	0.3113	1.6405	370

Figure 5.20 shows two periodic orbits around L_4, which belong to the long (92 days) and short (21 days) period families, respectively, in the non-dimensional coordinate system x'', y''. Both are much farther from L_4 with respect to the periodic orbits shown in Fig. 5.1.

Similarly, Figures 5.21(a) and 5.21(b) show the value of the discriminant of the sub-matrix F associated to the points $X_h(t)$ along the long and short period orbits shown in Fig. 5.20. Unlike the previous case, the sign of the discriminant in both trajectories are negative and positive, this means that although there does no exits regions with ZRRA at certain points along the periodic orbits, there does exist a set of points along these periodic orbits where the radial component of the relative acceleration is equal to zero. This fact can be seen if we compute numerically the ZRRA at three different points $X_h(t)$ along the previous periodic orbits, considering a sphere of radius s equal to 1 km as shown in Fig. 5.22.

The qualitative behaviour of the scalar product function is practically the same for all the values of t where there appear two maxima and two minima, respectively.

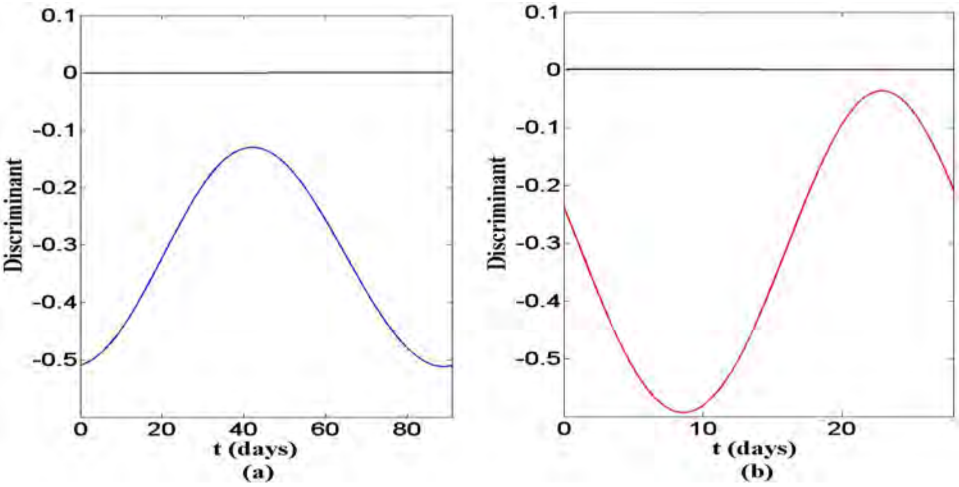

Figure 5.16 - Discriminant of the sub-matrix F associated to the points $X_h(t)$ along the (a) long and (b) short period orbits shown in Fig. 5.1

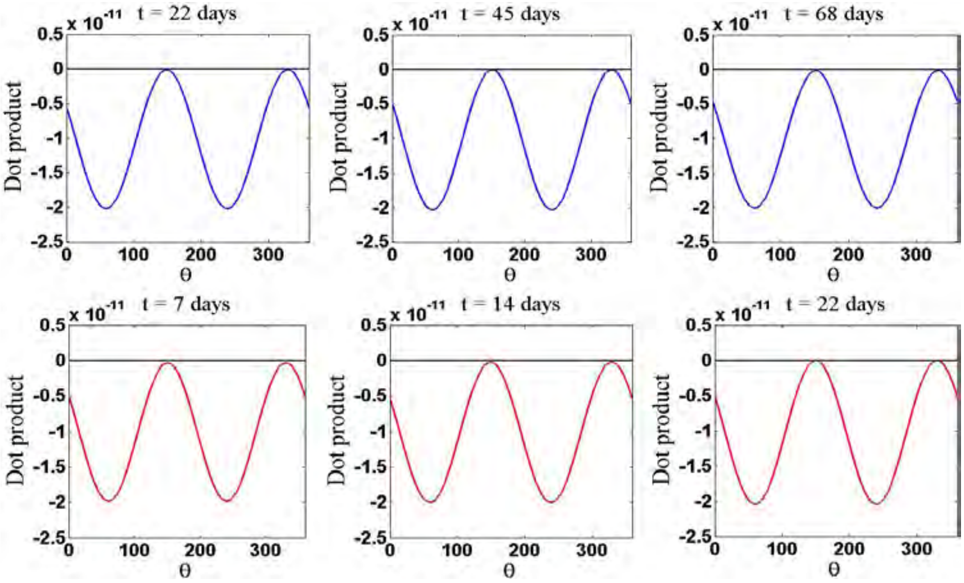

Figure 5.17 - Scalar product between the relative acceleration $\boldsymbol{a}\,(t,\theta)$ and vector $\boldsymbol{s}\,(\theta)$ as a function of angle θ at three different points $X_h\,(t)$ along the long (first row) and short (second row) period orbits shown in Fig. 5.1

However, there is a set of points in these trajectories where the radial component of the function $\boldsymbol{a}\,(t,\theta)$ is zero with vertex at $\boldsymbol{x_h}\,(t)$ for two different values of θ which we have denoted by θ^* and θ^{**}, where $\theta^* \leq \theta^{**}$ (since the scalar product function is periodic with respect to θ, the other two zeros represent the same situation). Therefore, in principle, a set of aligned spacecrafts placed in one of them will keep fixed their mutual distances. Thus, Figures 5.23(a) and 5.23(b) show the function θ associated to point $X_h\,(t)$ such that the relative radial acceleration is maximum for

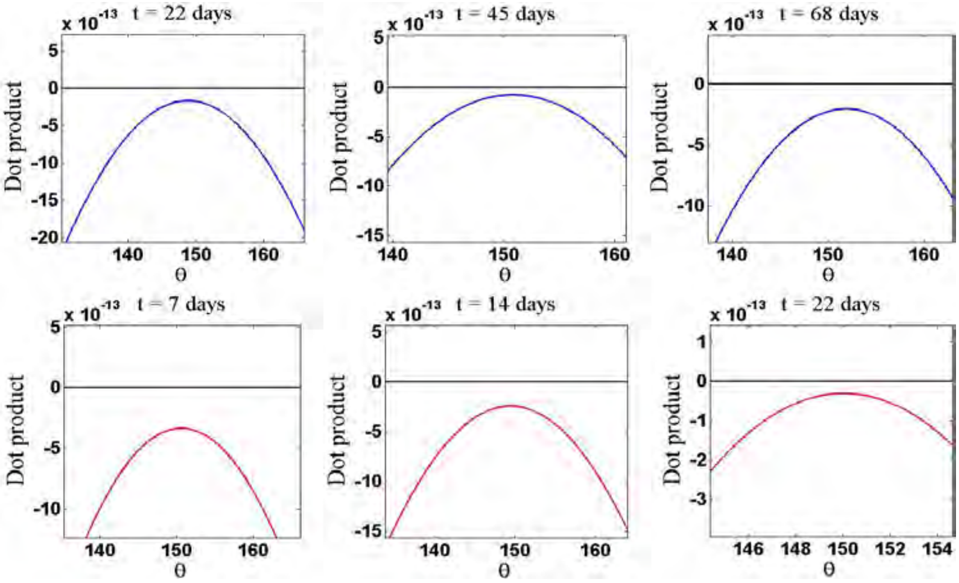

Figure 5.18 - Scalar product between the relative acceleration $\boldsymbol{a}(t, \theta)$ and vector $\boldsymbol{s}(\theta)$ as a function of angle θ at three different points $X_h(t)$ along the long (first row) and short (second row) period orbits shown in Fig. 5.1

all values of t along the long and short period orbits shown in Fig. 5.20, respectively. Similarly, Figure 5.24 shows the function θ for the values where the relative radial acceleration is minimum or zero for the long (first row) and short (second row) period orbits. As we can see in Fig. 5.24, when we only compute the values of θ where the scalar product function has a minimum, the function θ is smooth. But, when we compute the points where the scalar product function has a minimum or a zero, there are two points where this function is not smooth. This fact will produce a higher cost to maintain fixed the constellation as we will show later.

Now, Figures 5.25(a) and 5.25(b) show a family of long (92 days) and short (28 days) period around L_4. Similarly, we compute the discriminant of the sub-matrix F along each periodic orbit as shown in Fig. 5.26. This result supports a fact that was shown in the previous section. If the periodic orbit is close enough to L_4, there do not exit ZRRAL. However, if the periodic orbit is far enough from L_4, it begins to appear a set of points where there exist the ZRRA regions, in a such way that, this set is larger whether the periodic orbit is farther from L_4. Note that the size of this set has a limit in both family of periodic orbits.

It was computed the value of θ for every point $X_h(t)$ along each orbit that belongs to the long and short period family where the radial component acceleration is maximum, minimum or zero (in the cases where the discriminant is positive). Figures

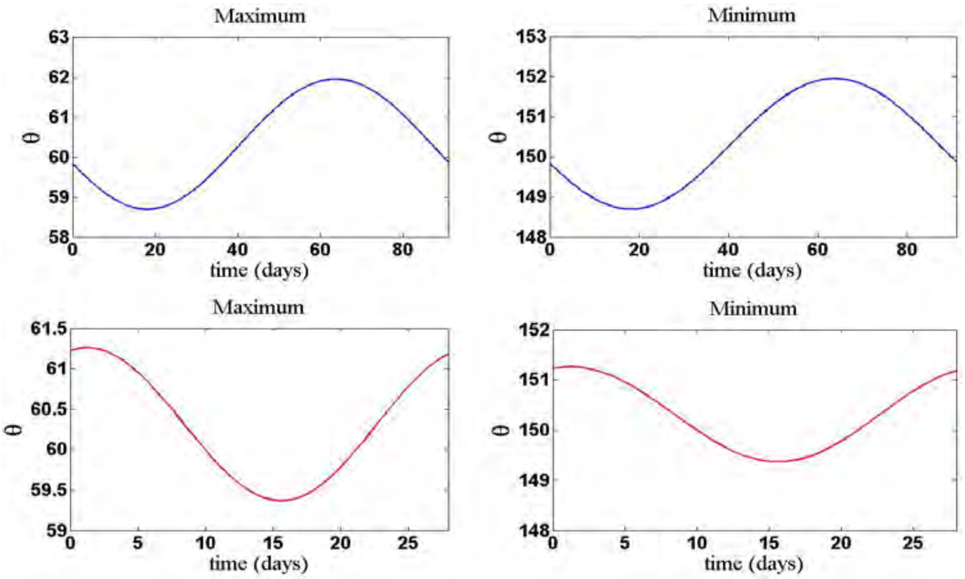

Figure 5.19 - Angle θ for each point $X_h(t)$ where the relative radial acceleration has a maximum and minimum value along the long (first row) and short (second row) period orbits shown in Fig. 5.1

5.27(a) and 5.27(b) show the value of θ such that the radial acceleration component is maximum for the long and short period family, respectively. Note that the range of function θ is bigger whether the periodic orbit is farther from L_4.

In the same manner, the periodic orbits that are far enough from L_4 the function θ has a minimum and two zeros. Figure 5.28 shows the value of θ such that the radial acceleration component is minimum or zero (denoted by θ^* and θ^{**}) for the long (first row) and short (second row) period families, respectively. Similarly, note that the range of function θ is also larger if the periodic orbit is farther from L_4 and the function θ is not smooth.

5.7 Cost to Maintain a Spacecraft on the regions of Zero, Minimum and Maximum Relative Radial Accelerations

We begin by supposing a spacecraft placed in an artificial trajectory around the periodic orbits shown in Fig. 5.1. Considering a radius s, in the configuration space (see Fig. 4.3), equal to 1 km and 2 km, and a time $T = 1$ year, Tables 5.23 and 5.24 show respectively the cost of maintaining the spacecraft when the artificial trajectory follows the direction in which the relative radial acceleration component is maximum (see left column in Fig. 5.19) and minimum (see right column in Fig. 5.19). It is interesting to note the costs of Table 5.24 are twice the costs of Table

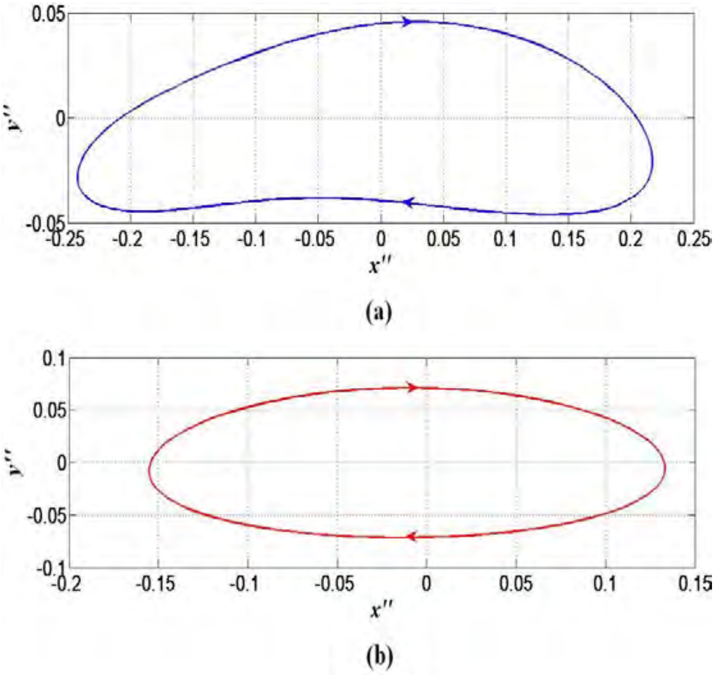

Figure 5.20 - (a) Long and (b) short period orbits around L_4.

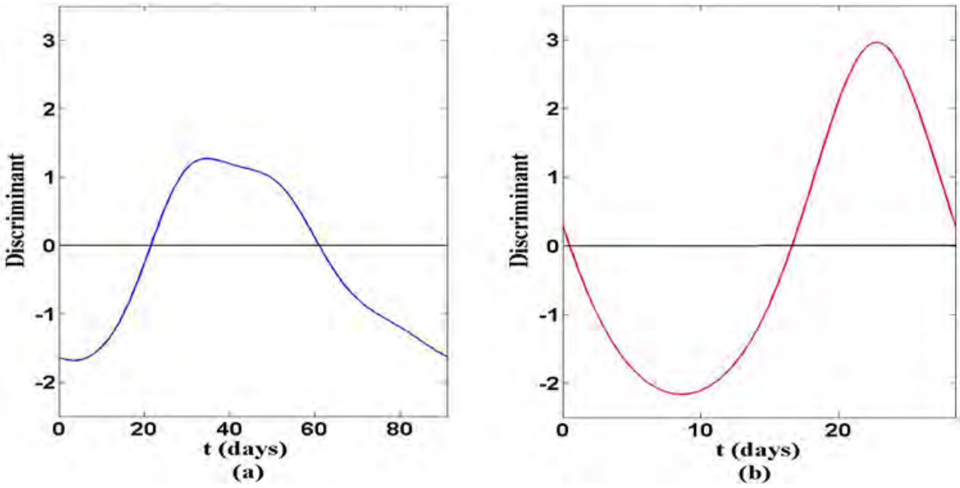

Figure 5.21 - Discriminant of the sub-matrix F associated to the points along the (a) long and (b) short period orbits shown in Fig. 5.20

5.23, i.e. there exists a linear relation with respect to the distance from $X_h(t)$. Additionally, the costs between the long and short period orbits are almost equal.

Now, we suppose a spacecraft placed in an artificial trajectory around the periodic orbits shown in Fig. 5.20. Similarly, considering a radius s equal to 1 km and 2 km, and a time $T = 1$ year, Table 5.25 shows the cost of maintaining the spacecraft when

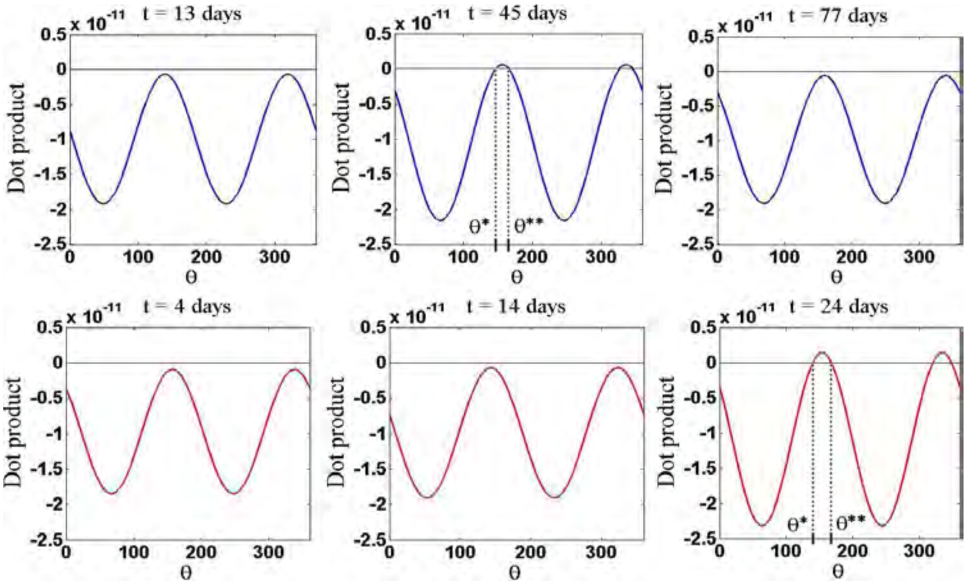

Figure 5.22 - Scalar product between the relative acceleration $\mathbf{a}(t, \theta)$ and vector $\mathbf{s}(\theta)$ as a function of angle θ at three different points $X_h(t)$ along the long (first row) and short (second row) period orbits shown in Fig. 5.20

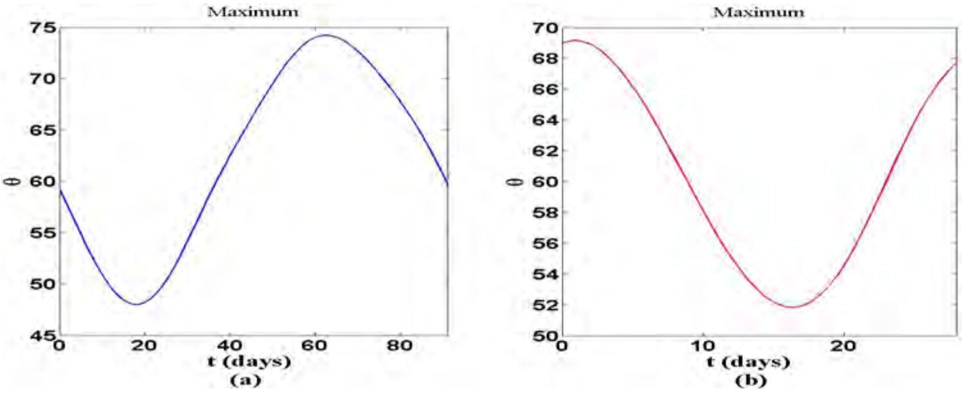

Figure 5.23 - Angle θ for each point $X_h(t)$ where the relative radial acceleration has a maximum value for the (a) long and (b) short period orbits shown in Fig. 5.20

the artificial trajectory follows the direction in which the relative radial acceleration component is maximum (see Fig. 5.23). Similarly, note that the costs of Table 5.25 follows a linear relation with respect to the radius and that, between these two long and short period orbits, the costs are approximately equal.

On the other hand, Tables 5.26 and 5.27 show the cost of maintaining the spacecraft when the artificial trajectory follows the direction in which the relative radial acceleration component is minimum or zero (see Fig. 5.24) considering a radius s

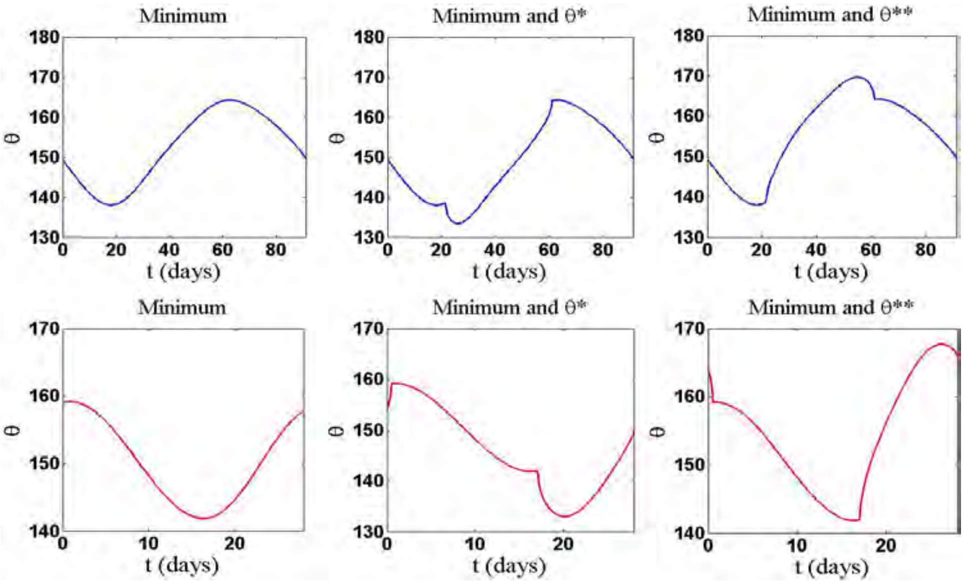

Figure 5.24 - Angle θ for each point $X_h(t)$ where the relative radial acceleration has a minimum or zero value for the long (first row) and short (second row) period orbits shown in Fig. 5.20

Table 5.23 - Cost of maintaining a spacecraft during 1 year considering a radius of 1 km with respect to periodic orbits shown in Fig. 5.1 and the direction in which the relative radial acceleration component is maximum and minimum

Period Orbit	Cost Maximum Radial Acceleration (m/s)	Cost Minimum Radial Acceleration (m/s)
Long	6.5777×10^{-1}	6.0422×10^{-3}
Short	6.2989×10^{-1}	6.1713×10^{-3}

Table 5.24 - Cost of maintaining a spacecraft during 1 year considering a radius of 2 km with respect to periodic orbits shown in Fig. 5.1 and the direction in which the relative radial acceleration component is maximum and minimum

Period Orbit	Cost Maximum Radial Acceleration (m/s)	Cost Minimum Radial Acceleration (m/s)
Long	1.3153	1.2084×10^{-2}
Short	1.2598	1.2343×10^{-2}

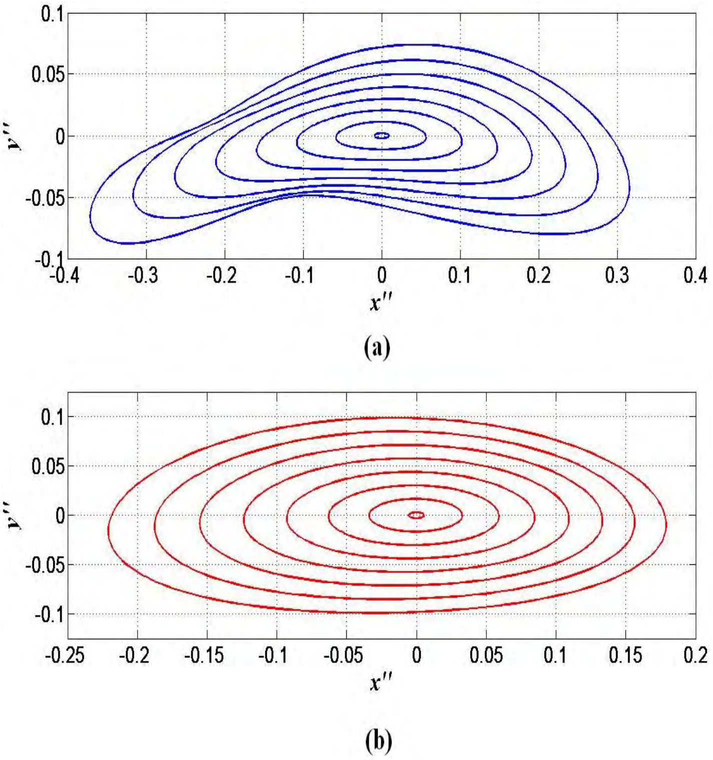

Figure 5.25 - (a) Long and (b) short period families around L_4.

Table 5.25 - Cost of maintaining a spacecraft during 1 year considering a radius of 1 km and 2 km with respect to periodic orbits shown in Fig. 5.20 and the direction in which the relative radial acceleration component is maximum

Period Orbit	Cost Maximum Radial Acceleration $s = 1$ km (m/s)	Cost Maximum Radial Acceleration $s = 2$ km (m/s)
Long	6.6074×10^{-1}	1.3215
Short	6.3015×10^{-1}	1.2603

equal to 1 km and 2 km, respectively. Similarly, there exits a linear relation between the cost and the radius of the artificial trajectory. However, the cost of maintaining the spacecraft, on the direction when the relative radial acceleration is minimum, is much less (almost ten times) than the cost to maintain the spacecraft on the direction when the relative radial acceleration is minimum or zero. This fact can be understood whether we compute the components x and y of the relative position, velocity and acceleration vectors described in Eq. (4.7). For example, Figure 5.29

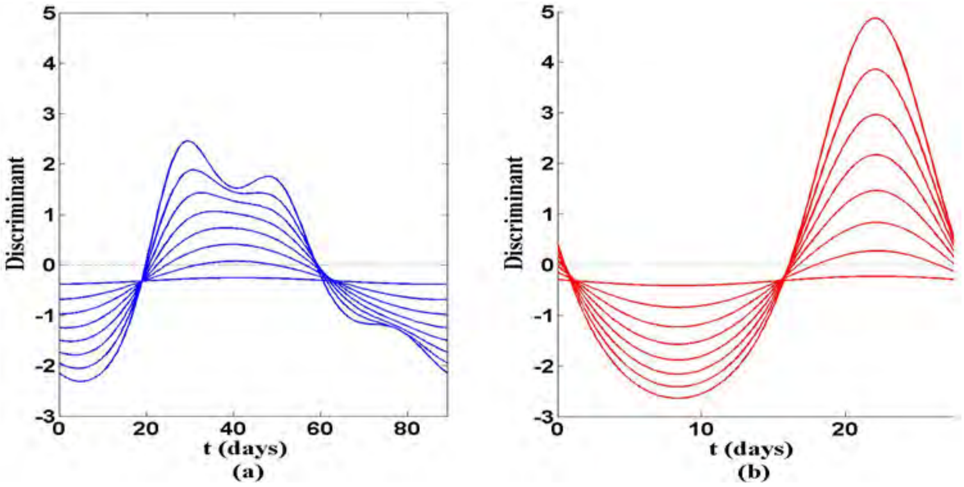

Figure 5.26 - Discriminant of the sub-matrix F associated to the points along the (a) long and (b) short period families shown in Fig. 5.25

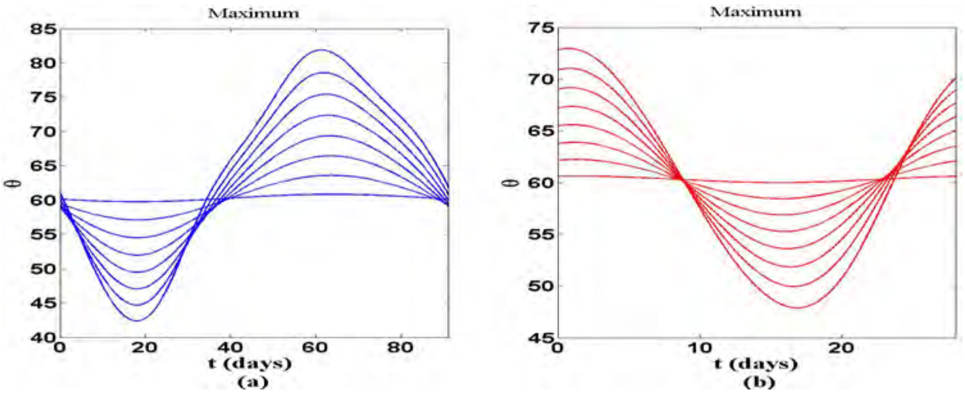

Figure 5.27 - Angle θ for each point $X_h(t)$ where the relative radial acceleration has a maximum value for the (a) long and (b) short period families shown in Fig. 5.25

shows the components x (left column) and y (right column) of the relative position $\boldsymbol{r_a}$ (first row), relative velocity $\dot{\boldsymbol{r}}_{\boldsymbol{a}}$ (second row) and relative acceleration $\ddot{\boldsymbol{r}}_{\boldsymbol{a}}$ (third row) of the artificial trajectory that follows the direction such that the relative radial acceleration component is minimum with respect to the long period orbit shown in Fig. 5.20. Similarly, Figure 5.30 shows the components of these vectors such that the relative radial acceleration component is minimum or zero with respect to the long period orbit shown in Fig. 5.20. Note that in Fig. 5.29 the two components for $\boldsymbol{r_a}, \dot{\boldsymbol{r}}_{\boldsymbol{a}}, \ddot{\boldsymbol{r}}_{\boldsymbol{a}}$, are smooth functions. Nevertheless, in Fig. 5.30 we can see that the components for each vector are not. In fact, the function $\boldsymbol{r_a}$ is not smooth at time t when the regions of ZRRA appear and disappear (see Fig. 5.24). Therefore, we see in the functions $\dot{\boldsymbol{r}}_{\boldsymbol{a}}$ and $\ddot{\boldsymbol{r}}_{\boldsymbol{a}}$ two big jumps at these two instants in such a way that

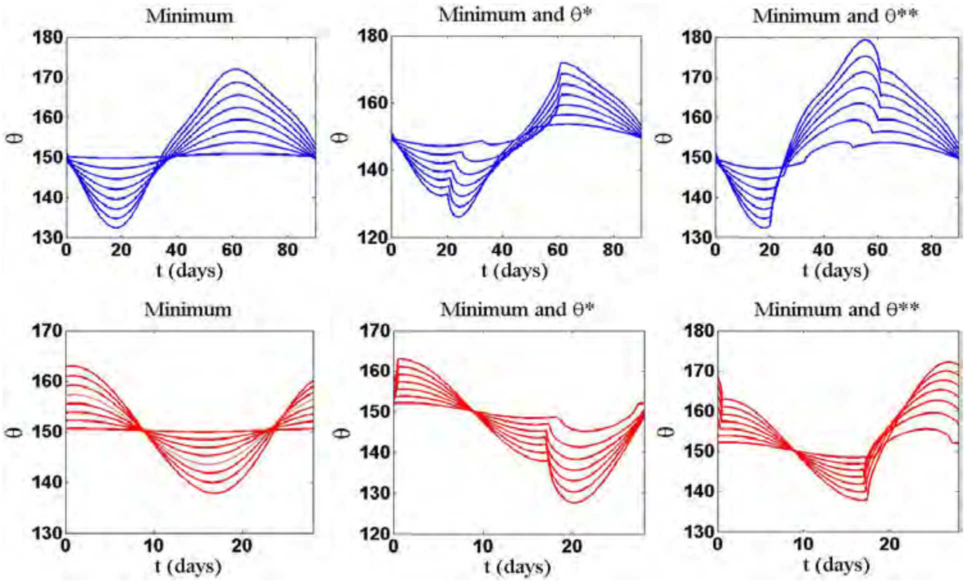

Figure 5.28 - Angle θ for each point $X_h\,(t)$ where the relative radial acceleration has a minimum or zero value for the long (first row) and short (second row) period families shown in Fig. 5.25

the function $\boldsymbol{R_a}$ is bigger in the region where the ZRRA exists as shown in Fig. 5.31. As a consequence, the cost ΔV will be less than if the artificial trajectory follows the direction where the relative radial acceleration is minimum but not zero.

Table 5.26 - Cost of maintaining a spacecraft during 1 year considering a radius of 1 km with respect to periodic orbits shown in Fig. 5.20 and the direction in which the relative radial acceleration component is minimum or zero

Period Orbit	Cost Minimum Radial Acceleration (m/s)	Cost Minimum and Zero (θ^*) Radial Acceleration (m/s)	Cost Minimum and Zero (θ^{**}) Radial Acceleration (m/s)
Long	7.0033×10^{-3}	6.4182×10^{-2}	6.5106×10^{-2}
Short	2.1255×10^{-2}	1.3563×10^{-1}	1.3635×10^{-1}

Finally, suppose that we denote the family of periodic orbits as shown in Fig. 5.32, where Orbit 1 denotes the smallest one and Orbit 8 denotes the largest one. Considering a radius equal to 1 km and a time $T = 1$ year, Tables 5.28 and 5.29 show the cost of maintaining a spacecraft with respect to each orbit of the long and short period family and the direction in which the relative radial acceleration component is maximum, minimum and zero, respectively.

Table 5.27 - Cost of maintaining a spacecraft during 1 year considering a radius of 2 km with respect to periodic orbits shown in Fig. 5.20 and the direction in which the relative radial acceleration component is minimum or zero

Period Orbit	Cost Minimum Radial Acceleration (m/s)	Cost Minimum and Zero (θ^*) Radial Acceleration (m/s)	Cost Minimum and Zero (θ^{**}) Radial Acceleration (m/s)
Long	1.4007×10^{-2}	1.2836×10^{-1}	1.3021×10^{-1}
Short	4.2510×10^{-2}	2.7126×10^{-1}	2.7270×10^{-1}

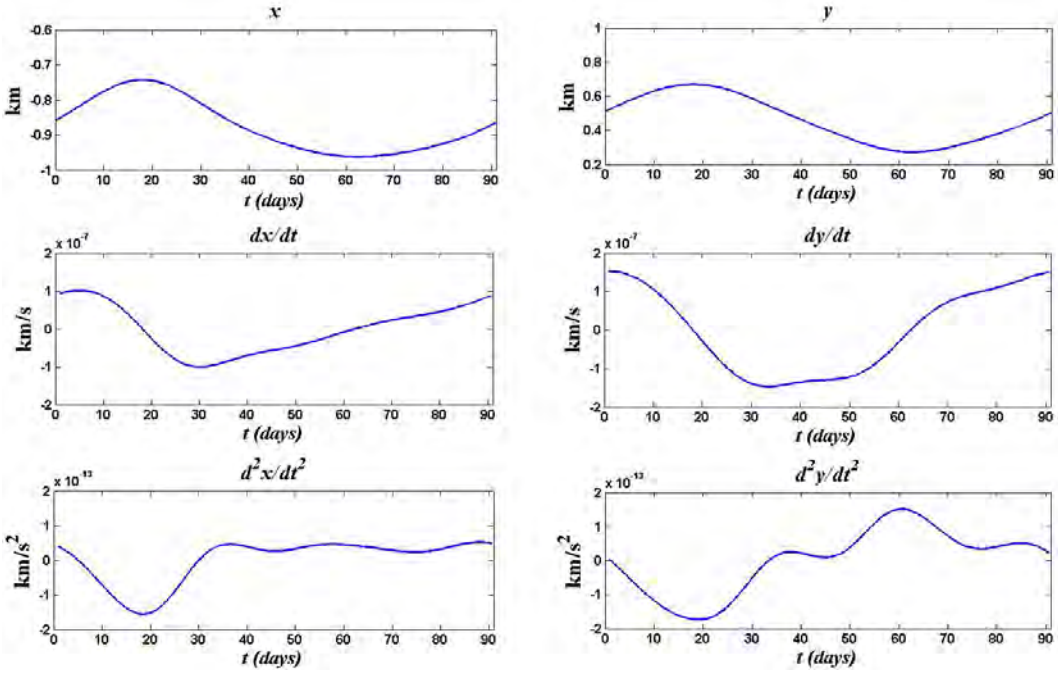

Figure 5.29 - Components x (right column) and y (left column) of relative position $\boldsymbol{r_a}$ (first row), relative velocity $\dot{\boldsymbol{r}}_{\boldsymbol{a}}$ (second row) and relative acceleration $\ddot{\boldsymbol{r}}_{\boldsymbol{a}}$ (third row) of the artificial trajectory that follows the direction such that the relative radial acceleration component is minimum with respect to the long period orbit shown in Fig. 5.20

5.8 Cost to Maintain a Spacecraft on a Fixed Configuration

In the previous section, we studied the cost of configurations that follows the direction in which the relative radial acceleration is maximum, minimum or zero. Now, we study the case when the geometry of the configuration remains constant, i.e. the angle θ is fixed (see Fig. 4.3).

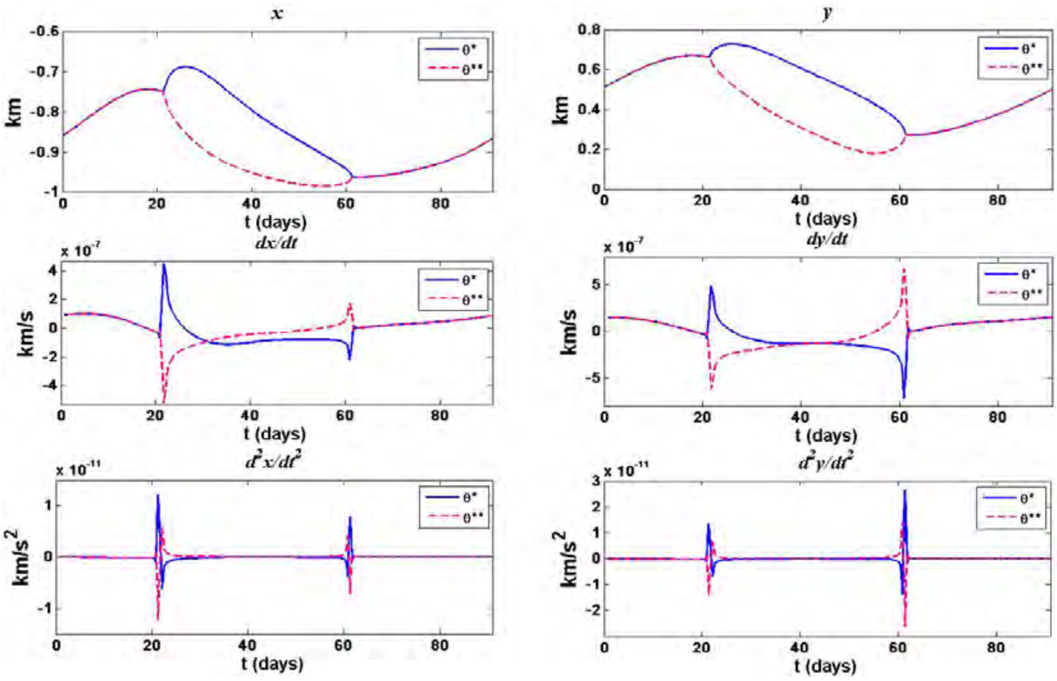

Figure 5.30 - Components x (right column) and y (left column) of relative position $\boldsymbol{r_a}$ (first row), relative velocity $\dot{\boldsymbol{r}}_{\boldsymbol{a}}$ (second row) and relative acceleration $\ddot{\boldsymbol{r}}_{\boldsymbol{a}}$ (third row) of the artificial trajectory that follows the direction such that the relative radial acceleration component is minimum or zero with respect to the long period orbit shown in Fig. 5.20

In this manner, Figures 5.33(a) and 5.33(b) show the cost of maintaining a spacecraft with respect to previous long and short period family, respectively, such that the angle θ is fixed and considering a radius of 1 km. The cost was computed until a time $T = 1$ year.

Note that the cost function in Fig. 5.33 has a period of 180°. Additionally, the function has two maxima at $\theta \approx 60°$ and $240°$, and two minima at $\theta \approx 150°$ and $330°$. These values practically coincide with the direction in which the relative radial acceleration component is maximum and minimum (see Fig. 5.19) for the periodic orbits shown in Fig. 5.1. In fact, the costs compared with these cases are similar.

In this way, we will study a triangular geometry around the periodic orbits shown in Figs. 5.1 and 5.20. In this configuration, we consider a formation flying of three satellites, such that their positions and distances with respect to periodic orbit are fixed and form an equilateral triangle. There are three cases we have analyzed in this formation as shown in Fig. 5.34:

(a) The periodic solution $X_h(t)$ remains in the center of the equilateral trian-

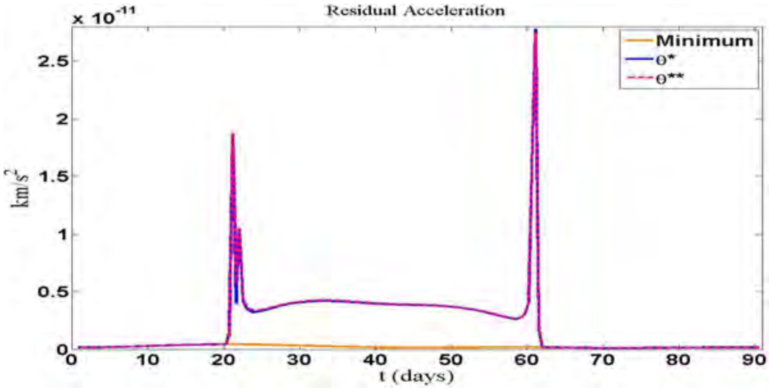

Figure 5.31 - Radial Acceleration of the artificial trajectory that follows the direction such that the relative radial acceleration component is minimum or zero with respect to the long period orbit shown in Fig. 5.20

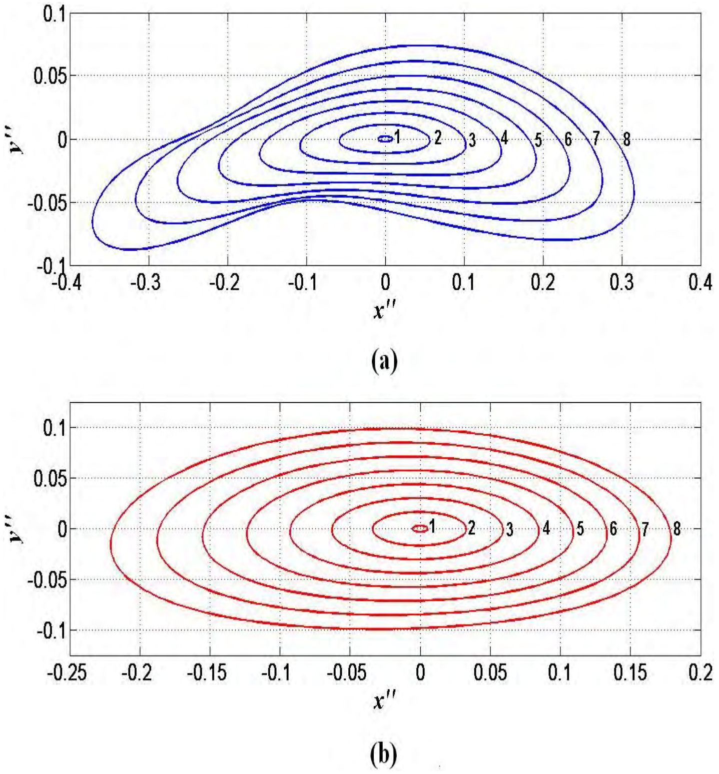

Figure 5.32 - Family of periodic orbits shown in Fig. 5.25, where Orbit 1 denotes the smallest one and Orbit 8 denotes the largest one

gle.

(b) The periodic solution $X_h\left(t\right)$ remains in the middle of one of the sides.

(c) One of the satellites remains on the periodic solution $X_h\left(t\right)$.

Table 5.28 - Cost of maintaining for 1 year a spacecraft with respect to long period family shown in Fig. 5.32 and the direction in which the relative radial acceleration component is maximum, minimum and zero

Period Orbit	Cost Maximum Radial Acceleration (m/s)	Cost Minimum Radial Acceleration (m/s)	Cost Minimum and Zero (θ^*) Radial Acceleration (m/s)	Cost Minimum and Zero (θ^{**}) Radial Acceleration (m/s)
1	6.5750×10^{-1}	6.0286×10^{-3}		
2	6.5792×10^{-1}	6.0881×10^{-3}	1.5004×10^{-2}	1.5062×10^{-2}
3	6.5850×10^{-1}	6.2313×10^{-3}	3.3591×10^{-2}	3.3850×10^{-2}
4	6.5925×10^{-1}	6.4562×10^{-3}	4.5180×10^{-2}	4.5567×10^{-2}
5	6.6014×10^{-1}	6.7676×10^{-3}	5.5834×10^{-2}	5.6401×10^{-2}
6	6.6116×10^{-1}	7.1855×10^{-3}	7.3302×10^{-2}	7.4046×10^{-2}
7	6.6230×10^{-1}	7.7586×10^{-3}	8.3866×10^{-2}	8.4787×10^{-2}
8	6.6360×10^{-1}	8.6312×10^{-3}	8.7558×10^{-2}	8.8503×10^{-2}

In these three cases, the orientation of the formation is defined by the angle θ which denotes the direction of the relative position of satellite 1. Once the angle θ is fixed, the other angles that define the relative positions of satellites 2 and 3 are easily computed by basic geometry. The cost to maintain the formation flying is simply the sum of the costs of maintaining each satellite in the fixed position. Figures 5.35(a) and 5.35(b) show the cost function of the triangular formation along the long and short period orbits around L_4 shown in Fig. 5.1, respectively, for $0° \leq \theta \leq 180°$ (the cost function has a period of 180°) and a time $T = 1$ year. The length of the side of the equilateral triangle is equal to 2 km. As we can see in Fig. 5.35, for the long and short period orbits, the minimum cost is obtained when the formation flying follows the configuration (c) whether the angle $\theta = 90°$ and $\theta = 150°$. However, we can note that the cost of configuration (b) is almost the same whether the angle $\theta = 60°$. Therefore, it can be said that the minimum cost is obtained when the formation flying follows the configuration (b) and (c) and one of the satellites is placing along the direction of angle $\theta = 150°$.

Table 5.29 - Cost of maintaining for one year a spacecraft with respect to short period family shown in Fig. 5.32 and the direction in which the relative radial acceleration component is maximum, minimum and zero

Period Orbit	Cost Maximum Radial Acceleration (m/s)	Cost Minimum Radial Acceleration (m/s)	Cost Minimum and Zero (θ^*) Radial Acceleration (m/s)	Cost Minimum and Zero (θ^{**}) Radial Acceleration (m/s)
1	6.4023×10^{-1}	5.9153×10^{-3}		
2	6.4013×10^{-1}	7.4009×10^{-3}	6.4286×10^{-2}	6.4920×10^{-2}
3	6.4025×10^{-1}	1.0242×10^{-2}	9.1027×10^{-2}	9.1375×10^{-2}
4	6.4054×10^{-1}	1.3850×10^{-2}	9.9301×10^{-2}	1.0013×10^{-1}
5	6.4092×10^{-1}	1.7736×10^{-2}	1.2289×10^{-1}	1.2372×10^{-1}
6	6.4137×10^{-1}	2.1740×10^{-2}	1.3883×10^{-1}	1.3987×10^{-1}
7	6.4189×10^{-1}	2.5826×10^{-2}	1.4365×10^{-1}	1.4685×10^{-1}
8	6.4255×10^{-1}	2.9996×10^{-2}	1.8064×10^{-1}	1.8140×10^{-1}

Finally, Figures 5.36(a) and 5.36(b) show the cost function of the triangular formation along the long and short period orbits around L_4 shown in Fig. 5.20. The results show that the minimum cost is obtained when the formation flying follows the configuration (c) whether the angle $\theta = 103°$ and $\theta = 143°$ for the long and short period orbits, respectively. Additionally, it is interesting to see that the configuration (c) is not only the case which we obtain the minimum cost but also the maximum cost.

5.9 Dynamical Behaviour of Different Kinds of Solutions

In this last section we analyze the dynamical behaviour of the different kinds of solutions with initial conditions along a sphere centered at the point $X_h(0)$. The goal is to study the initial conditions for a spacecraft with respect to the periodic orbit $X_h(t)$ such that the separation between the spacecraft and the periodic solution is optimal.

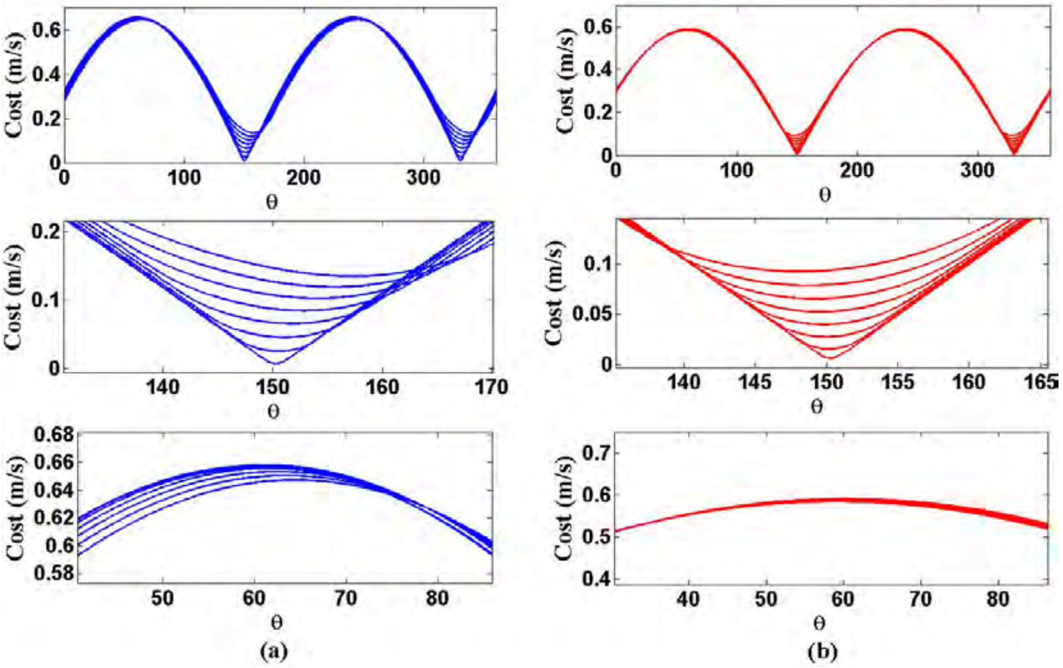

Figure 5.33 - Cost of maintaining a spacecraft during 1 year with respect to the long (a) and short (b) period family shown in Fig. 5.25 fixing the angle θ and considering a radius of 1 km

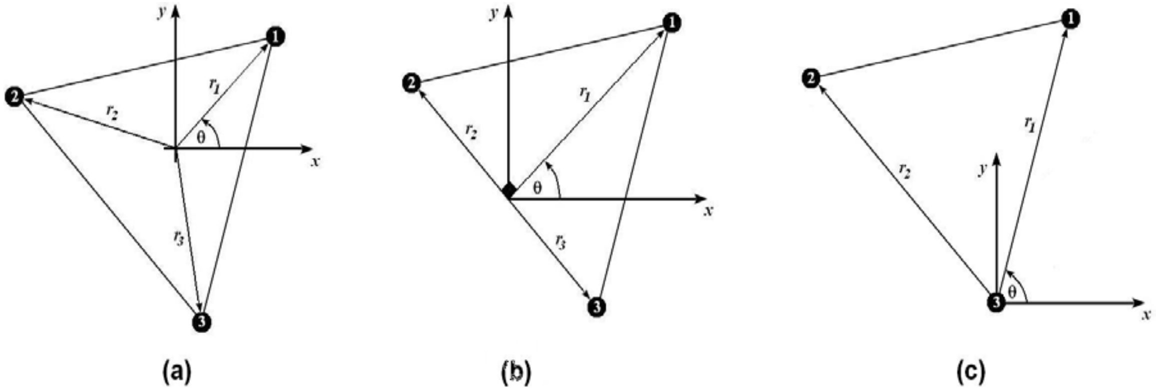

Figure 5.34 - Formation flying of three satellites such that their positions and distances with respect to periodic orbit are fixed and form an equilateral triangle

Firstly, suppose a spacecraft around a periodic orbit of L_4 where the initial relative position is defined by the magnitude of the radius r and the value of the angle θ. This sphere is centered at $X_h(0)$ as shown in Fig. 5.37. In this case, we are interested in to determine the initial conditions $(r(0), \theta(0))$ in such a way that the deviation of the spacecrafts from the initial conditions over the time must be minimum. Using

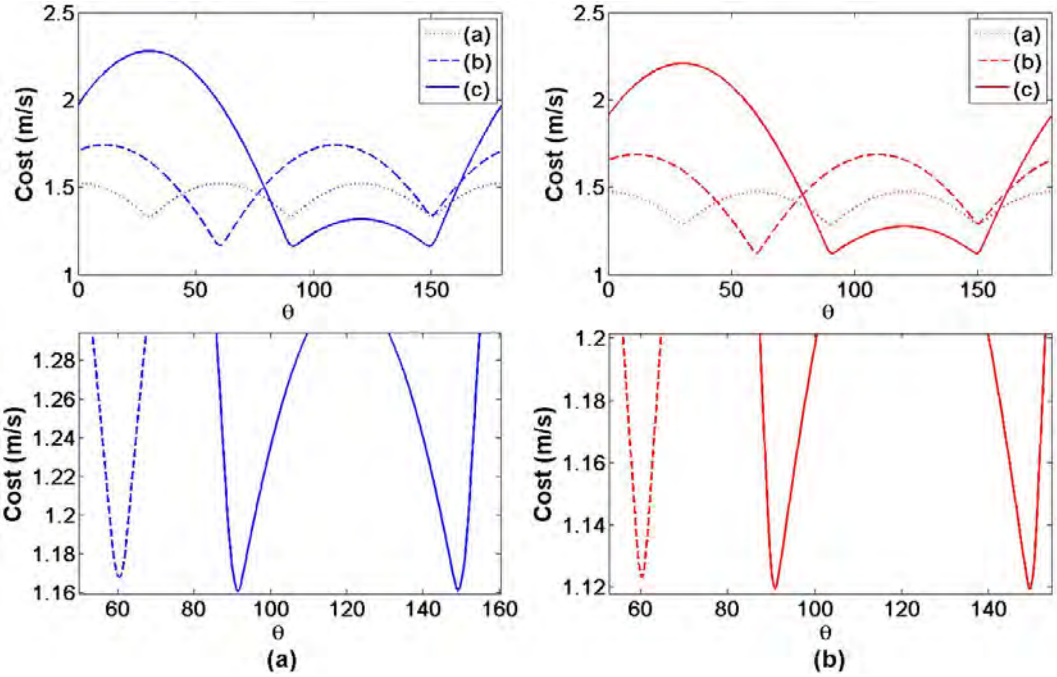

Figure 5.35 - Cost of maintaining during 1 year a Formation flying of three satellites considering configurations (a), (b) and (c) around the long and short period orbits shown in Fig. 5.1

polar coordinates, the set of initial conditions will be the form:

$$(\boldsymbol{x_h}(0) + \boldsymbol{r}(0), \boldsymbol{v_h}(0)).$$

Figures 5.38 and 5.39 show the maximum separation (in km) for different values of $(r(0), \theta(0))$ computed in nine points $X_h(0)$ along the long and short period orbits shown in Fig. 5.1, respectively. For each solution with initial condition $(r(0), \theta(0))$ the maximum magnitude during 2 years of the vector $\Delta X(t) = (X(t) - X_h(t))$ is computed. These results show that, given a solution close enough to these periodic orbits, the maximum separation obtained is less than 10 km whether the angle $\theta(0) \approx 150°$. On the other hand, the maximum separation is greater than 40 km whether $\theta(0) \approx 60°$. This fact practically does not depend on the initial point $X_h(0)$ taken along the periodic orbits and the maximum separation function has a period of 180° as shown in Figs. 5.38 and 5.39. Note that this fact coincides with the cost of maintaining a spacecraft along the minimum and maximum relative radial acceleration.

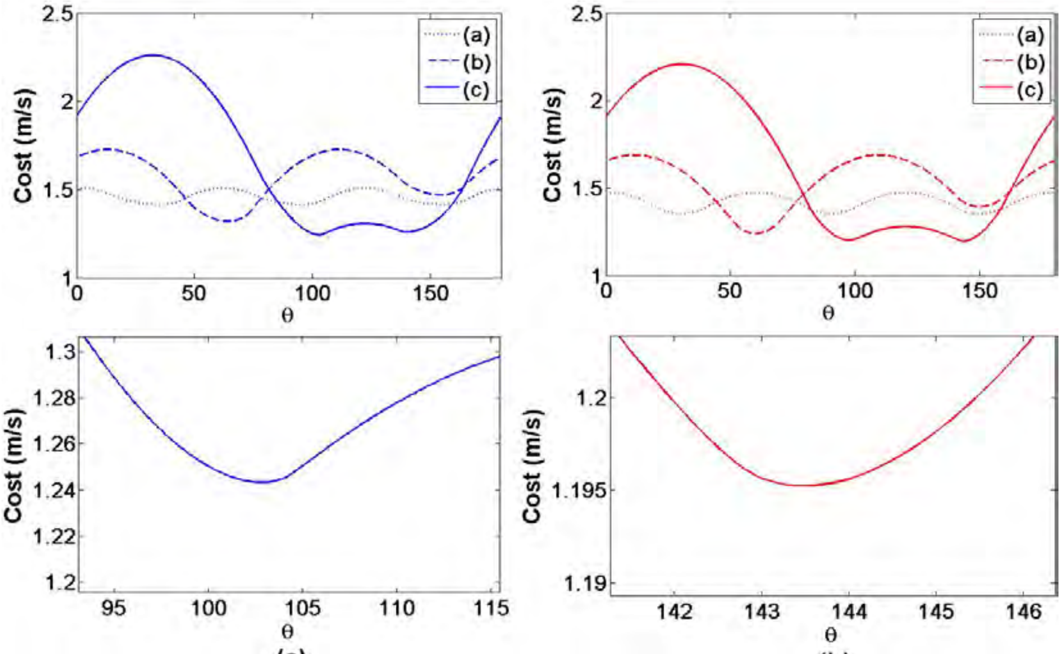

(a) (b)

Figure 5.36 - Cost of maintaining during 1 year a Formation flying of three satellites considering configurations (a), (b) and (c) around the long and short period orbits shown in Fig. 5.20

Now, given an initial condition $(r\,(0)\,,\theta\,(0))$, we want to study the dynamical behaviour of the distance function, denoted by $d\,(X_h\,(t)\,,X\,(t))$, between the spacecraft and the periodic orbits around L_4 at each time t. First, Figure 5.40 shows the value of the maximum separation during 2 years for $0° \leq \theta\,(0) \leq 360°$ and $r\,(0) = 1$, 2 km along the long period orbit shown in Fig. 5.1. Similarly, Figure 5.41 shows the value of the maximum separation during two years along the short period orbit shown in Fig. 5.1. We have integrated these two initial conditions and, as it could be seen previously, the best and worst cases occur when $\theta\,(0) = 150°$ and $\theta\,(0) = 60°$, respectively. Therefore, the distance function will be computed when $\theta\,(0) = 150°$ and $\theta\,(0) = 60°$ to compare the difference between the quantitative behaviour of $d\,(X_h\,(t)\,,X\,(t))$.

For the first case, we have taken four relative initial vectors $\boldsymbol{r_1}\,(0)\,,\boldsymbol{r_2}\,(0)\,,\boldsymbol{r_3}\,(0)\,,$ and $\boldsymbol{r_4}\,(0)$ along the direction of $\theta\,(0) = 150°$ associated to the initial condition $X_h\,(0)$ of the periodic orbit around L_4 (see Fig. 5.37). The vectors have been distributed symmetrically with respect to $X_h\,(0)$: $\boldsymbol{r_1}\,(0)$ and $\boldsymbol{r_3}\,(0)$ being at an initial distance of 1 km from $X_h\,(0)$ and, $\boldsymbol{r_2}\,(0)$ and $\boldsymbol{r_4}\,(0)$ being at an initial distance of 2 km. We have integrated these trajectories during three years and the results are shown in the first row of Fig. 5.42. As can bee seen, the maximum deviation from the starting

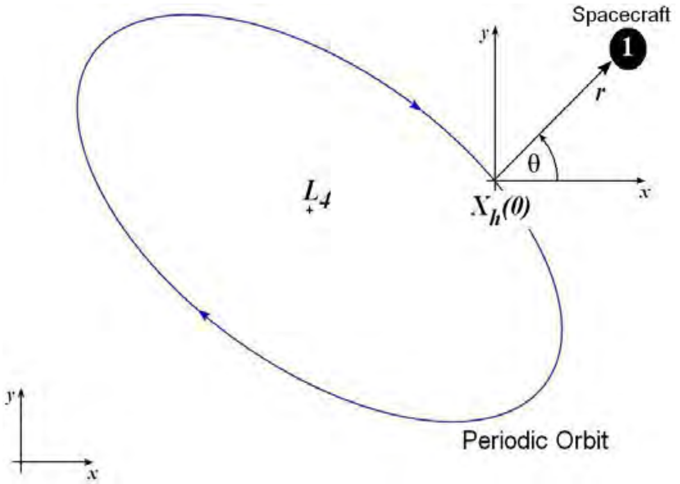

Figure 5.37 - Illustration of the relative position of a spacecraft around a periodic orbit of L_4

separations is less than 1.5 km for the orbits with initial vectors $\boldsymbol{r_i}(0)$. The distance function $d(X_h(t), X_i(t))$ is a periodic function with period equal to 460 days. Additionally, there is no difference between the qualitative and quantitative behaviour of the distance function for the trajectories starting at the same distance from $X_h(0)$: $d(X_h(t), X_1(t)) \approx d(X_h(t), X_3(t))$ and $d(X_h(t), X_2(t)) \approx d(X_h(t), X_4(t))$.

Now, for the second case, we take four relative initial vectors $\boldsymbol{q_1}(0)$, $\boldsymbol{q_2}(0)$, $\boldsymbol{q_3}(0)$, and $\boldsymbol{q_4}(0)$ along the the direction of $\theta(0) = 60°$ corresponding also to the initial condition $X_h(0)$ of the periodic orbit around L_4, distributed in a similar fashion to the previous case. In the second row of Fig. 5.42 we show the results for the distance function $d(X_h(t), X_i(t))$. Now, although the qualitative behavior is also periodic (period equal to 460 days) and there is no difference between the qualitative and quantitative behaviour of the distance function for the trajectories starting at the same distance from $X_h(0)$, the deviations from the periodic orbit are larger (they are increased by a factor of 40) than the ones obtained for the $\boldsymbol{r_i}(0)$ initial vectors taken along the direction of $\theta(0) = 150°$.

Finally, the same study is made along the long and short period orbits shown in Fig. 5.20. The purpose is also to analyze the dynamical behaviour of the distance function for periodic orbits that are far enough from L_4. In Fig. 5.43 it can be seen that the best position to minimize the deviation is along the direction of $\theta(0) = 149°$ associated to the initial condition of the long period orbit. In the same way, the position that maximize the deviation is along the direction of $\theta(0) = 59°$. Practically, the difference with respect to the previous results is only 1°. Similarly, Figure 5.44

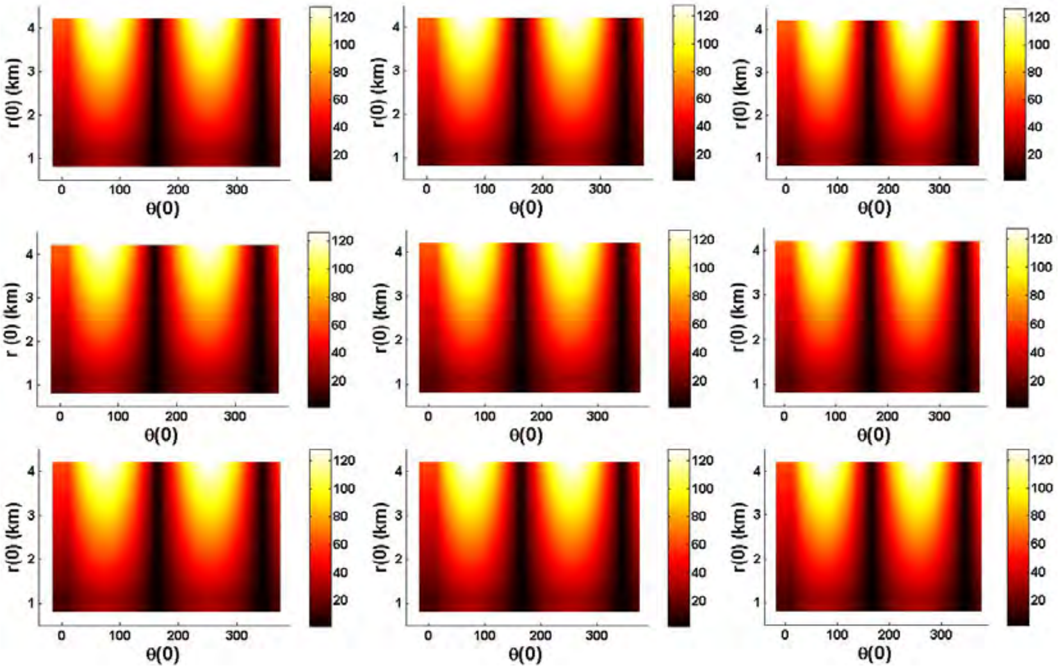

Figure 5.38 - Maximum separation (in km) during 2 years for different values of $r\,(0)$ and $\theta\,(0)$ computed in nine points $X_h\,(0)$ along the long period orbit shown in Figure 5.1

shows that the position to minimize and maximize the deviation is along the direction of $\theta\,(0) = 157°$ and $\theta\,(0) = 67°$, respectively, associated to the initial condition of the short period orbit. In this case, the difference with respect to the previous results is 7°.

Similarly, we take four relative initial vectors along the the direction of minimum and maximum deviation corresponding also to the initial condition $X_h\,(0)$ of the periodic orbit around L_4, distributed in a similar fashion to the previous cases. The results are shown in Fig. 5.45. In the first row we can see that the distance function is periodic (period equal to 460 days for the long period orbit and 545 for the short period orbit) and that the maximum deviation from the starting separations is less than 2 km. Now, in the second row it can be seen that the distance functions are periodic (period equal to 460 days for the long period orbit and 545 for the short period orbit) and the deviations from the periodic orbit are also increased by a factor of 40. Additionally, there is no difference between the qualitative and quantitative behaviour of the distance function for the trajectories starting at the same distance from $X_h\,(0)$.

As final point, it can be seen in Figs. 5.42 and 5.45 that there exits a linear behaviour

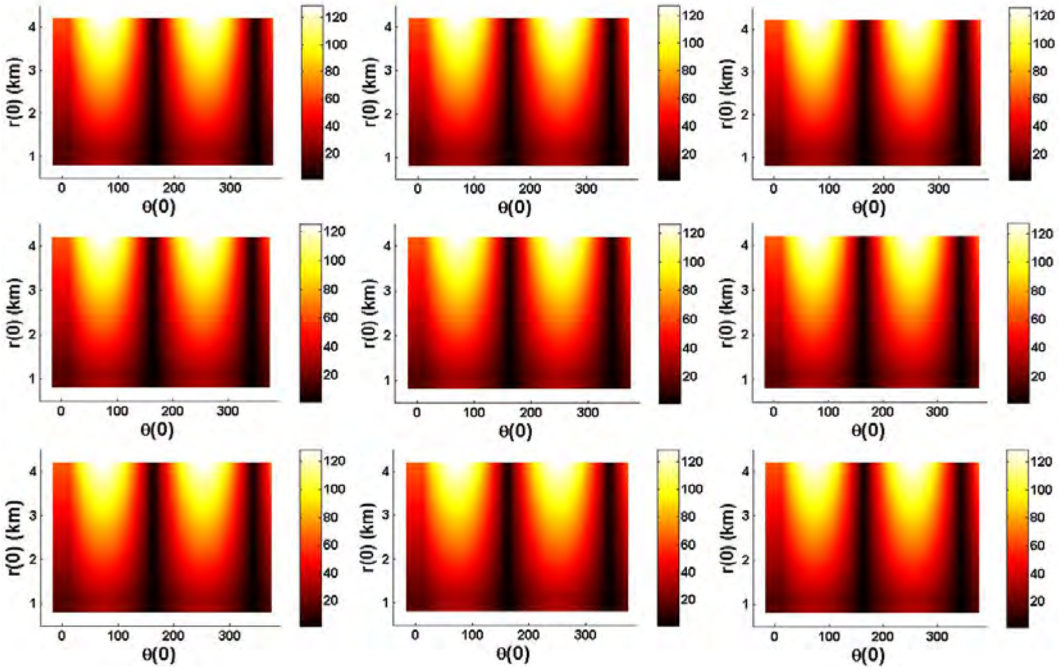

Figure 5.39 - Maximum separation (in km) during 2 years for different values of $r\,(0)$ and $\theta\,(0)$ computed in nine points $X_h\,(0)$ along the short period orbit shown in Figure 5.1

between the distance functions for the trajectories starting at 1 km and 2 km from $X_h\,(0)$, i.e, the deviation for the trajectories starting at 1 km is half for the trajectories starting at 2 km from $X_h\,(0)$. Remember that this linear behaviuour was also noted in the case of the cost of maintaining a spacecraft along the direction of zero, minimum and maximum relative radial acceleration. Therefore, there is no difference in the qualitative behaviour of the distance function for the trajectories starting at 1 km and 2 km from $X_h\,(0)$, and the spacecrafts that start at those points probably remains aligned during the time span. To verify this fact, we compute the difference between the angles θ_1 and θ_2 at each instant t for the all previous trajectories starting at 1 km and 2 km from $X_h\,(0)$ as shown in Fig. 5.46. In Figs. 5.47(a) and 5.47(b) we can see the results associated to the initial condition of the long and short period orbits shown in Fig. 5.1, respectively. Similarly, Figs. 5.48(a) and 5.48(b) shows the results associated to the initial condition of the long and short period orbits shown in Fig. 5.20, respectively. As we can note, the difference of the angles θ_1 and θ_2 at each instant t is practically zero, consequently, the spacecrafts remain aligned along the periodic orbits around L_4, but their distances from the solution $X_h\,(t)$ oscillate periodically as illustrated in Fig. 5.49.

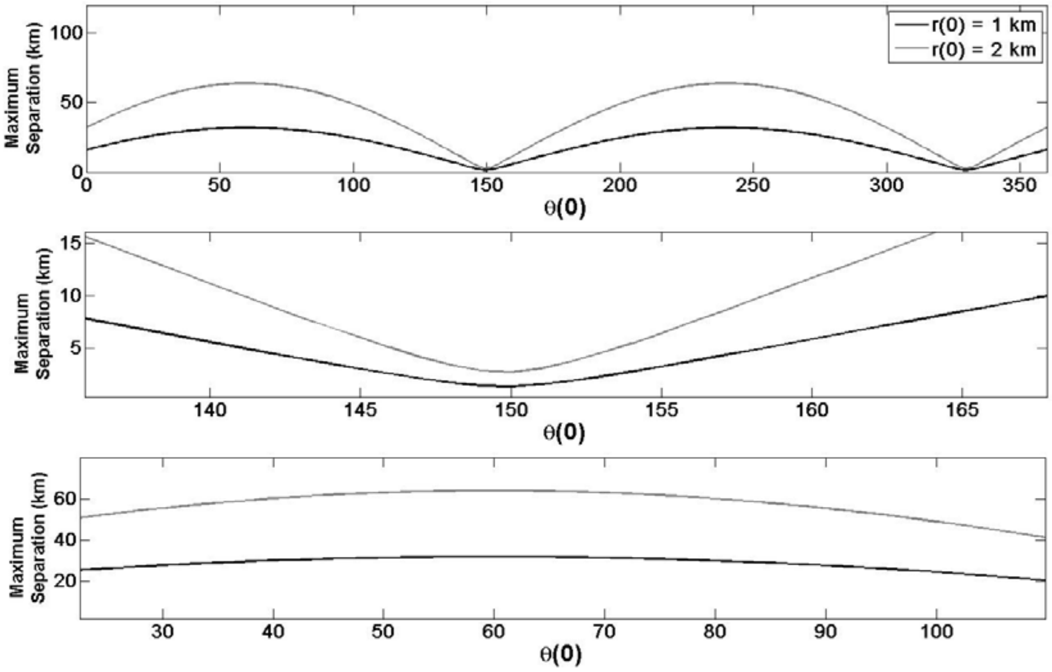

Figure 5.40 - Maximum separation (in km) during 2 years for $0^\circ \leq \theta(0) \leq 360^\circ$ and $r(0) = 1$, 2 km along the long period orbit shown in Fig. 5.1

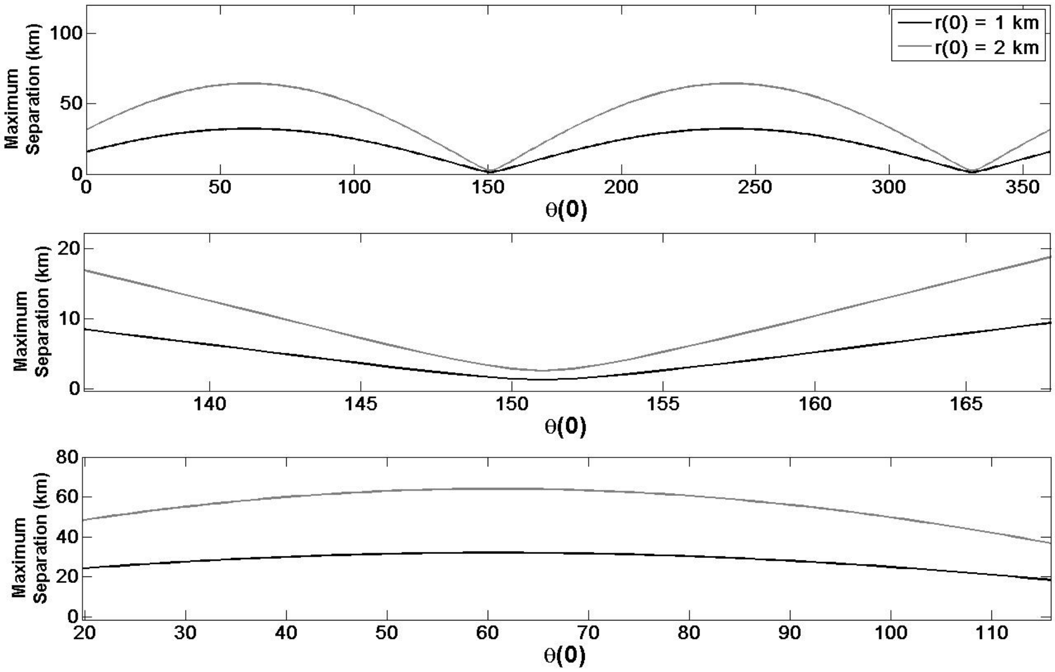

Figure 5.41 - Maximum separation (in km) during 2 years for $0^\circ \leq \theta(0) \leq 360^\circ$ and $r(0) = 1$, 2 km along the short period orbit shown in Fig. 5.1

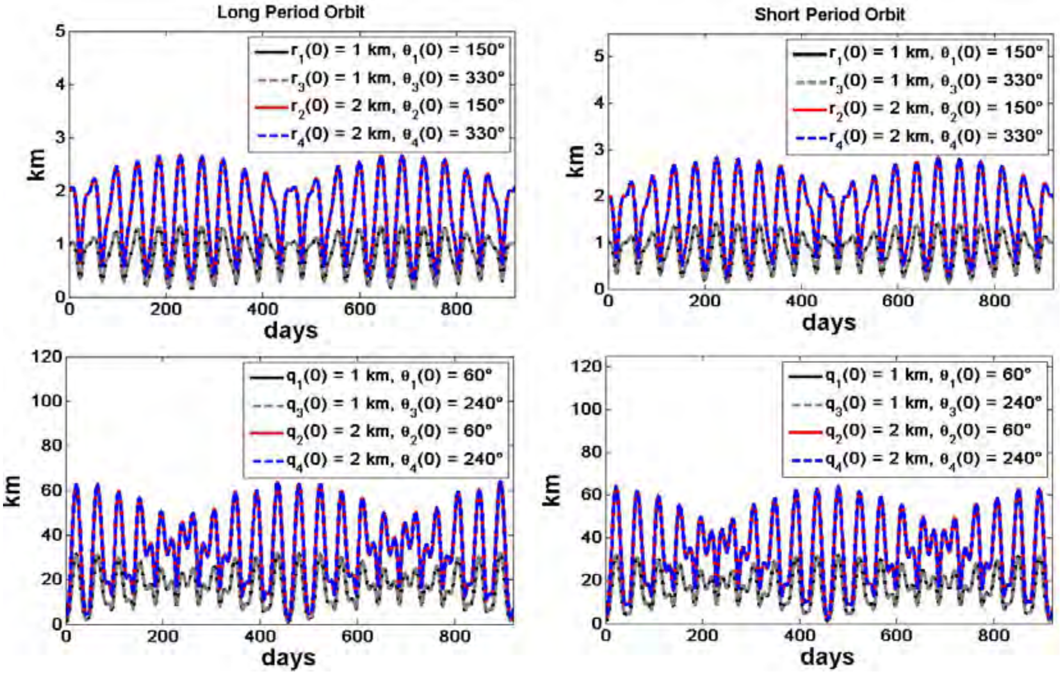

Figure 5.42 - Distance function $d\left(X_h\left(t\right), X_i\left(t\right)\right)$, between the trajectories of $\boldsymbol{r_1}$, $\boldsymbol{r_2}$, $\boldsymbol{r_3}$, $\boldsymbol{r_4}$ (first row), and $\boldsymbol{q_1}$, $\boldsymbol{q_2}$, $\boldsymbol{q_3}$, $\boldsymbol{q_4}$ (second row), and the long and short period orbits shown in Figure 5.1

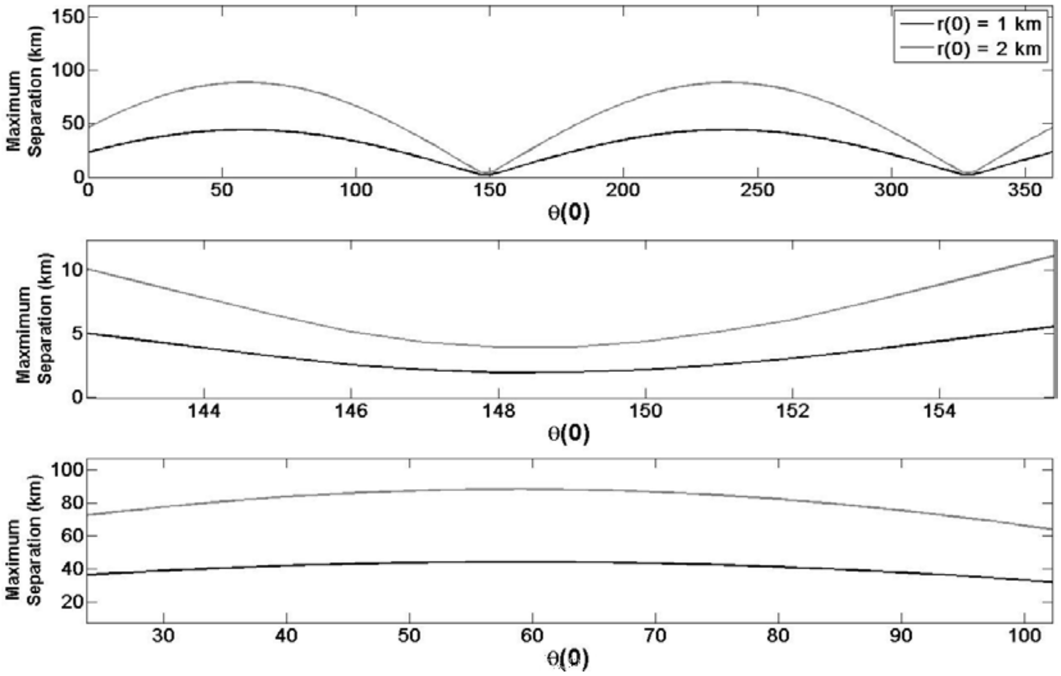

Figure 5.43 - Maximum separation (in km) during two years for $0° \leq \theta\left(0\right) \leq 360°$ and $r\left(0\right) = 1$, 2 km along the long period orbit shown in Figure 5.20

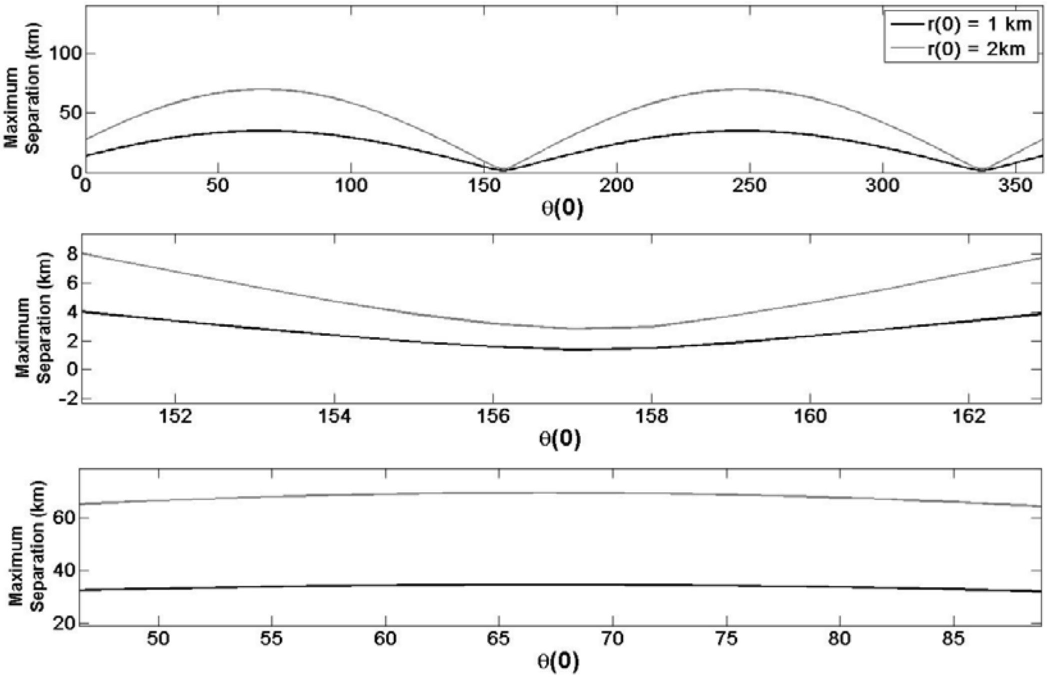

Figure 5.44 - Maximum separation (in km) during two years for $0^\circ \leq \theta(0) \leq 360^\circ$ and $r(0) = 1$, 2 km along the short period orbit shown in Figure 5.20

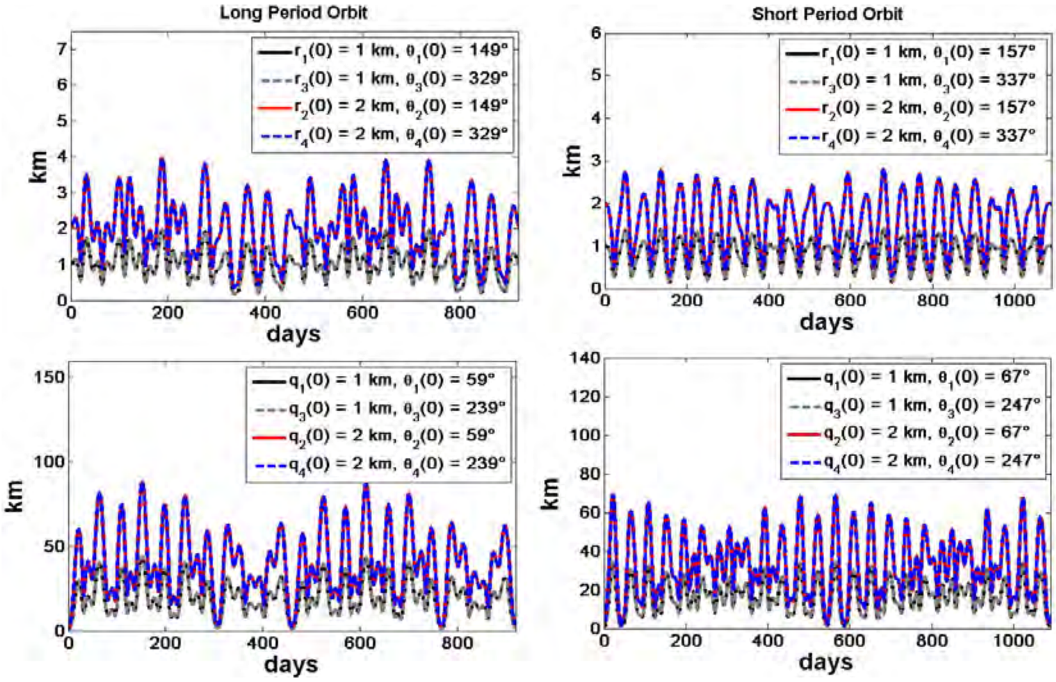

Figure 5.45 - Distance function $d(X_h(t), X_i(t))$, between the trajectories of $\boldsymbol{r_1}$, $\boldsymbol{r_2}$, $\boldsymbol{r_3}$, $\boldsymbol{r_4}$ (first row), and $\boldsymbol{q_1}$, $\boldsymbol{q_2}$, $\boldsymbol{q_3}$, $\boldsymbol{q_4}$ (second row), and the long and short period orbits shown in Figure 5.20

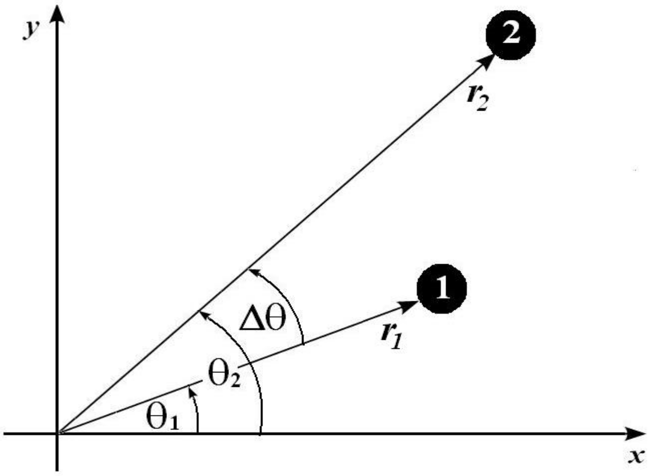

Figure 5.46 - Difference between the angles θ_1 and θ_2 for trajectories starting at 1 km and 2 km from $X_h\,(0)$

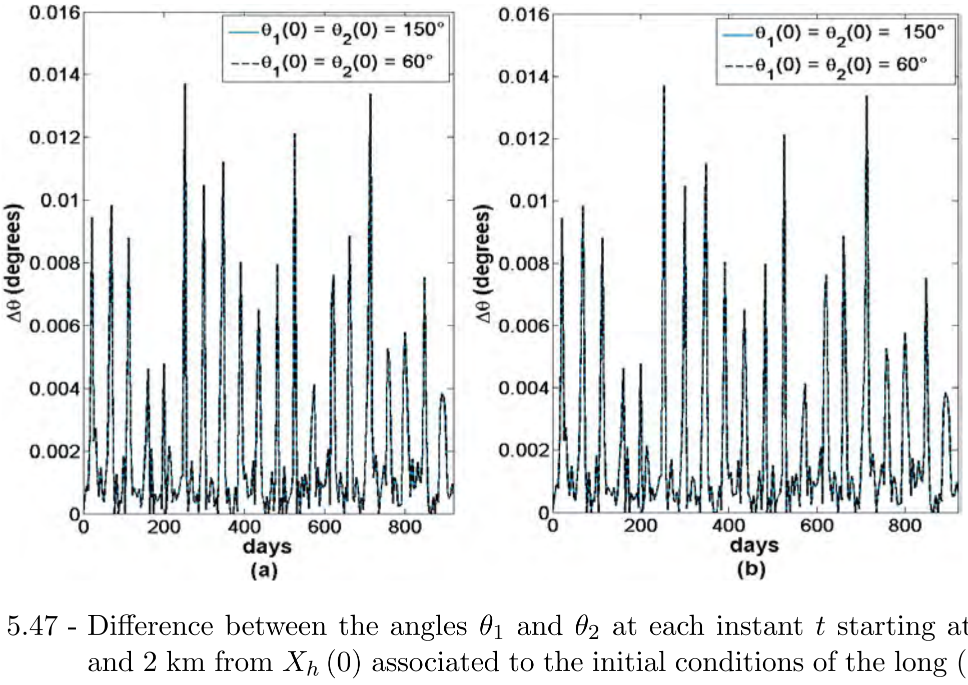

Figure 5.47 - Difference between the angles θ_1 and θ_2 at each instant t starting at 1 km and 2 km from $X_h\,(0)$ associated to the initial conditions of the long (a) and short (b) period orbits shown in Fig. 5.1

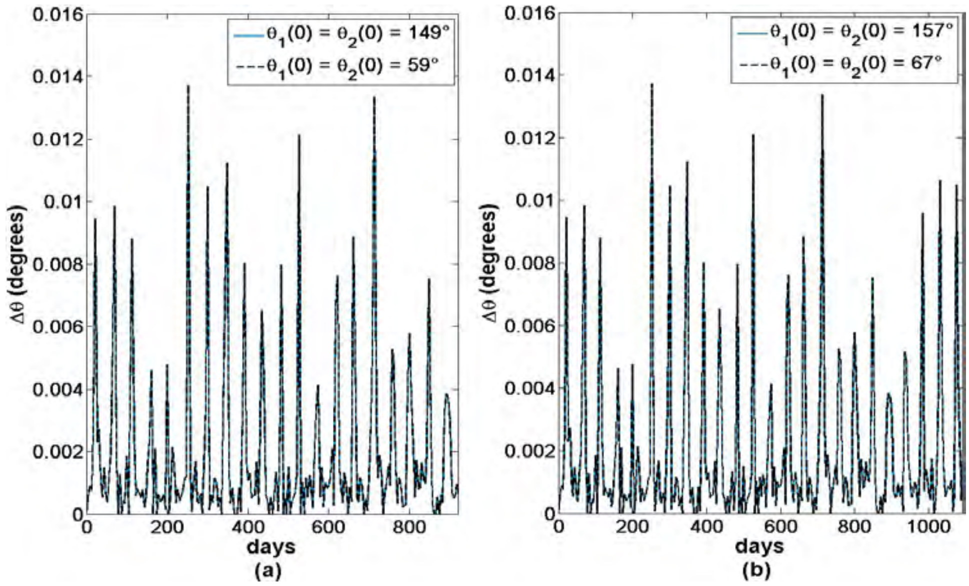

Figure 5.48 - Difference between the angles θ_1 and θ_2 at each instant t starting at 1 km and 2 km from $X_h(0)$ associated to the initial conditions of the long (a) and short (b) period orbits shown in Fig. 5.20

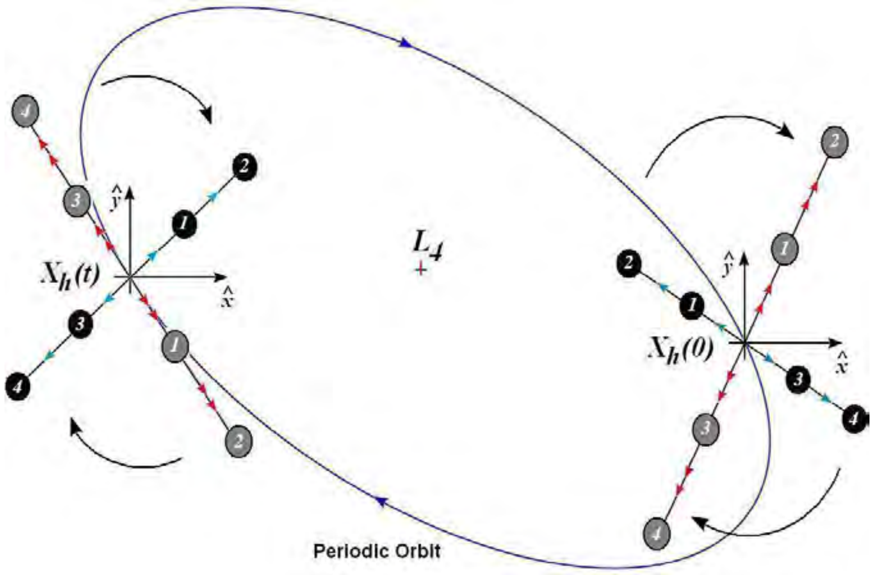
L4
Xh(t)
ŷ
x̂
Xh(0)
ŷ
x̂
1
2
3
4
1
2
3
4
1
2
3
4
1
2
3
4
Periodic Orbit

Figure 5.49 - Illustration of a constellation of satellites remaining aligned along the periodic orbits around L_4

6 CONCLUSIONS

In this work minimum energy transfers orbits have been computed for L_4 and L_5 missions in the Earth-Moon system. The model that was used is the Circular Restricted Three Body Problem. In the first step, the lunar gravity was neglected and the transfer orbit followed an elliptic trajectory given by the Hohmann transfer such that the independent variable was the apocentre of the orbit. In this approach, we obtained trajectories that reach the equilateral equilibrium points spending practically the same amount of fuel ($\Delta v_T = 3.91$ km/s) than is required to place a spacecraft around the Moon. In the second approximation, we used the Moon's gravity to gain enough energy such that the trajectory intersect the elliptic orbits around L_4 and L_5. In this second step, the independent variables were the apocentre of the elliptic transfer orbit and the angle at which the departure trajectory intersects the lunar sphere of influence. Once the spacecraft left the Moon's sphere of influence, the spacecraft experimented a change in the arrival velocity and energy with respect to the Earth such that the new geocentric trajectory reached the periodic orbits around L_4 or L_5. It was shown for the L_4 mission that using the Moon's gravity we could reach the target spending 3% less total fuel than the Hohmann transfer. Additionally, the stability of certain trajectories for the L_4 mission was greater than all trajectories for L_5 mission. However, the transfer time was less for the L_5 mission (about 9 days).

Similarly, another two new alternative methods to transfer spacecrafts from an Earth circular parking orbit in the direction of the equilateral equilibrium points have also been implemented.

The first alternative combined trajectories derived from the G Family and swing-by maneuvers such that the spacecrafts were able to reach the Moon's sphere of influence and, using the lunar gravity, arrive at L_4 and L_5. Once the altitude of the initial parking orbit and the value of the semi-major and -minor axes of the elliptic orbits around L_4 and L_5 were defined, a small perturbation in the initial impulsive thrust and in the spacecrafts' velocities at the apogee of the G Trajectories had to be determined numerically to place the spacecraft exactly into these stable orbits.

The simulations showed that a spacecraft needs to perform a swing-by with the Moon's trailing side to reach L_4 and by the Moon's leading side to reach L_5. In the case of L_4 mission, there is an increase in the energy of the spacecraft relative the Earth after the swing-by maneuver in such a way the energy becomes positive. This fact implies that whether our goal is to arrive at L_4, one possibility is to put the spacecraft in a trajectory, derived from the G Family, that escape the Earth-Moon system. On the other hand, L_5 mission showed a decrease in the energy of the spacecraft after the swing-by and remaining negative along the trajectory. Now, it was interesting to note that the variation of the energy of the spacecraft for L_5 mission is much smaller compared to L_4 mission but enough to reach L_5. Additionally, the magnitude of the velocities of the spacecrafts in the synodic frame was practically the same along the L_4 and L_5 trajectories.

The G Trajectories approach has the advantage with respect to Hohmann-like transfer orbits that few small spacecrafts could be placed into periodic orbits around L_4 and L_5 (or around the Moon) using the fact that this trajectories pass just a few dozen kilometers from the Moon's surface and that, although the spacecrafts are injected in the trajectory that leads to L_5, a low impulse applied in the apogee could place one of them into another Trajectory G that leads to L_4. The fuel spent in this case would be less than a Hohmann-like transfer.

The second alternative studied in this work combined the chaotic and swing-by transfers in such a way that the spacecraft was able to reach the Moon and use the lunar gravity field to arrive at L_4 or L_5. However, there are two problems with this kind of transfer: cost and time of flight. Firstly, the chaotic region is located at $59,669$ km above the Earth's center. Hohmann transfer could be used to reach this altitude. On the other hand, an additional boost is necessary to inject the spacecraft into the chaotic region. If all of these boosts were applied using chemical propulsion, the cost of the maneuver would not be economically viable. For example, a small spacecraft with total mass of 300 kg could only transfer a maximum payload mass of 30 kg. In this case, the maneuver presented in this work combined electric and chemical propulsion such that the transfer orbit, between a LEO with an altitude of 400 km and a circular orbit of radius $59,669$ km around the Earth, was made using electric propulsion where the thrust was constant and tangential. Once the spacecraft reached the higher orbit, the chemical propulsion was used to inject it into the chaotic region. The result was a smaller fuel requirement that allowed the transfer of a larger payload (100 kg if the total were 300 kg).

Once the cost of the mission was reduced, the transfer time represented another challenge. For this kind of transfer, the time of flight is very long because the chaotic trajectory has some recurrent loops and therefore the transport between the connected chaotic component could be 25 years. Nevertheless, these loops can be removed applying low impulsive thrusts along the stable and unstable manifolds of the trajectory projected in the Poincaré section. The result was a considerable reduction of transfer time from 25 years to 1.3 years approximately. In this manner, once that the spacecraft reached the Moon, it was necessary only two more low impulsive thrusts to arrive at Lagrangian points. The swing-by transfer required a boost of ~ 0.077 km/s and a correction maneuver of ~ 0.3 km/s to place it into the elliptic orbits around L_4 and L_5 points. This shows that the chaotic transfer is an interesting alternative to transfer a spacecraft without requiring large rocket thrusts.

It is important to note that for the four techniques implemented, the period of the two periodic orbits around L_4 and L_5 did not affected practically the magnitude of the stabilizing impulsive thrust required to place the spacecraft into the periodic orbits.

Finally, once the spacecrafts are placed in a periodic orbit around the equilibrium points we have that the Zero Relative Radial Acceleration Lines (ZRRAL) determine the relative position, represented by an angle θ, of a satellite with respect to a nominal trajectory, such that the radial component of the relative acceleration is null. This fact implies that once the satellite is placed in this region, the separation from the nominal trajectory would be shorter than if the relative acceleration of the satellite had radial component. In principle, the cost to maintain it along the nominal trajectory would be minimum.

In the case of periodic orbits close enough to L_4, the ZRRAL do not exist. For these orbits, the relative position of the satellite has values for the angle θ such that its relative acceleration has either maximum or minimum radial component. On the other hand, the ZRRAL only exist when the periodic orbit is far enough to L_4. However, for these orbits, the ZRRAL do not exist for every point of the periodic orbit. Therefore, in these cases, the relative position of the satellite has values for the angle θ such that its relative acceleration has maximum, minimum or zero radial component.

The cost to maintain a satellite following an artificial trajectory was determined by the integral of the Residual Acceleration. In the case of periodic orbits around L_4, it was shown that the cost is less when relative position of the satellite points out in the direction such that the radial component of the relative acceleration is minimum although the ZRRAL do exist. Due to the fact that these regions appear and disappear along the periodic orbit, this produces a discontinuity in the components of the relative velocity and acceleration and therefore a higher cost. Similarly, it was computed the cost to maintain a satellite when the relative position was fixed, i.e. the angle θ remained constant along a family of periodic orbits around L_4. The function cost had a maximum at $\theta \approx 60°$ and a minimum at $\theta \approx 150°$.

In this manner, a formation flying of three satellites was studied. The configuration was a triangular geometry, such that the relative position along the periodic orbit was fixed and formed an equilateral triangle. The cost to maintain this configuration was minimum when one of the satellites remained at the periodic orbit.

Note that in the force model defined by the Circular Restricted Three Body Problem, the cost to maintain the satellites in these configurations (ZRRAL, maximum or minimum radial acceleration, fixed angle) was very low. This fact is due to the stability of the periodic orbits around L_4 in such a way that a particle that begins very close to a periodic orbit, their mutual distances will keep practically fixed, so the control applied in the spacecraft must be almost zero.

The dynamical behaviour of the distance function between a constellation of satellites and the periodic orbits around L_4 was also determined. It could be seen that the the maximum separation function does not depend on the initial condition taken along the periodic orbits and that this function has a period of 180°. Similarly, the best position to reduce the maximum separation is about $\theta = 150°$. In the other case, the position that increase the maximum separation is about $\theta = 60°$. Thus, placing satellites along the directions of either minimum or maximum deviation from the starting separations, the distance from the periodic orbit behaved as a periodic function in such a way that the satellites remained aligned. Therefore, if we want to maintain fixed the configuration, a thrust would be necessary only to control the separation. In the case of minimum deviation, since the deviation in some cases was less than 2 km, the cost of maintaining the distance fixed would be very small.

In addition, it is interesting to note that in all the cases studied in this work: relative radial acceleration, cost of maintaining a spacecraft with angle fixed, cost of maintaining a triangular constellation and deviation of the constellation from the starting separations, the minimum and maximum value were obtained whether the spacecrafts were placing approximately along the direction of the major and minor axes of the elliptic orbits around L_4.

REFERENCES

ALFRIEND, K.; GIM, D. W.; VADALI, S. The characterization of formation flight satellite relative motion orbits. In: AAS/AIAA SPACEFLIGHT MECHANICS MEETING, 12., 2002, San Antonio, Texas. **Proceedings of the AAS/AIAA Space Flight Mechanics Meeting**. Springfield, Virginia: American Astronautical Society, 2002. Available from: <`http://searchworks.stanford.edu/view/5163849`>. 1

ALLGOVER, E. L.; GEORG, K. **Introduction to numerical continuation methods**. Collins, Colorado: Colorado State University, 1990. 34

ARAÚJO, N. S. Estudo de transferências orbitais utilizando algortimo genético. In: SEMINÁRIO DE INICIAÇÃO CIENTÍFICA DO INPE (SICINPE), 2011, São José dos Campos. **Anais**. São José dos Campos: INPE, 2011. p. 20. Available from: <`http://urlib.net/8JMKD3MGP7W/3AHEJQ3`>. xv, 6

BATE, R.; MUELLER, D.; WHITE, J. **Fundamentals of astrodynamics**. New York: Dover Publicantions, Inc., 1971. 45

BATTIN, R. H. **An introduction to the mathematics and methods of astrodynamics**. New York: AIAA Education Series, AIAA, 1987. 10, 41, 42

BATTRICK, B. **X-ray evolving-universe spectroscopy**: The xeus mission summary. Paris: ESA Publications Division, 2000. 1

BELBRUNO, E. A.; GOTT, J. R. Where did the moon come from? **Astronautical Journal**, v. 129, n. 3, p. 1724–1745, March. 4

BOLLT, E. M.; MEISS, J. D. Controlling chaotic transport through recurrence. **Physica D**, v. 8, p. 280–294, 1995. 12, 64

_____. Targeting chaotic orbits to the moon through recurrence. **Physics Leters A**, v. 204, p. 373–378, 1995. 12, 13, 58, 61, 94

BOYD, P. T.; MCMILLAN, S. L. W. Chaotic scattering in the gravitational three-body problem. **CHAOS:** An Interdisciplinary Journal of Nonlinear Science, v. 3, n. 4, p. 507–523, 1993. 7

BREAKWELL, J. V.; BROWN, J. The halo family of 3-dimensional periodic orbits in the earth-moon restricted 3-body problem. **Celestial Mechanics**, v. 20, p. 389–404, 1979. 2

BRISTOW, J.; FOLTA, D.; HARTMAN, K. A formation flying technology vision. In: AIAA SPACE 2000 CONFERENCE AND EXPOSITION, 2000, Long Beach, California. **Proceedings of AIAA Space 2000 Conference and Exposition**. Reston, Virginia: American Institute of Aeronautics and Astronautics, 2000. 1

BROUCKE, R. **Reserches d'orbites périodiques dans le problème restrient plan (système Terre-Lune)**. Dissertation — University of Louvain, Louvain, Belgium, 1962. 28

BROUCKE, R. A. Periodic orbits in the restricted three-body problem with earth-moon masses. **Technical Report 32-1168, NASA JPL, California**, 1968. 11, 53

_____. Traveling between the lagrange points and the moon. **Journal of Guidance, Control, and Dynamics**, v. 2, n. 4, p. 257–263, 1979. 9

_____. The celestial mechanics of gravity assist. In: AIAA/AAS ASTRODYNAMICS CONFERENCE, 1988, Minneapolis, Minnesota. **Proceedings of AIAA/AAS Astrodynamics Conference**. Washington, DC: American Institute of Aeronautics and Astronautics, 1988. p. 69–78. 9, 56, 87

BURNS, R.; MCLAUGHLIN, C. A.; LEITNER, J.; MARTIN, M. Techsat 21: formation design, control, and simulation. In: 2000 IEEE AEROSPACE CONFERENCE, 2000, Big Sky, Montana. **Proceedings of IEEE Aerospace Conference**. New York, NY: Institute of Electrical and Electronics Engineers, 2000. p. 19–25. 1

DANBY, J. M. A. **Fundamentals of celestial mechanics**. Virginia: Willmann-Bell, inc., 1962. 2

EULER, L. De motu rectilineo trium corporum se mutuo attrahentium. **Novi Commentarii Academiae Scientiarum Imperialis Petropolitanae**, p. 144–151, 1776. 24

FAQUHAR, R. W. The control and use of libration-point satellites. **NASA Technical Report R-346, Goddard Space Flight Center**, 1970. 2

FILLIPI, G. **Station Keeping at the L4 Libration Point: A Three Dimensional Study**. Masters thesis, Dept. Aeronautics and Astronautics — Air Force Institute of Technology Wright-Patterson AFB, Ohio, USA, 1978. 3

FRIDLUND, C. V. M. Darwin - the infrared space interferometry mission. **ESA Bulletin**, v. 103, p. 20–63, 2000. 1

GAUTSCHI, W. **Numerical analysis**: an introduction. Boston: Birkhauser, 1997. 32

GÓMEZ, G.; JORBA, A.; MASDEMONT, J.; SIMO, C. **Dynamics and mission design near libration points vol 3**. Singapore: World Scientific, 2001. 7

GÓMEZ, G.; KOON, W. S.; MARSDEN, J. E.; MASDEMONT, J.; ROSS, S. D. Invariant manifolds, the spatial three-body problem and space mission design. In: AIAA/AAS ASTRODYNAMICS SPECIALIST MEETING, 2001, Quebec City, Canada. **Proceedings of AIAA/AAS Astrodynamics Specialist Meeting**. Reston, Virginia: American Institute of Aeronautics and Astronautics, 2001. p. 20. Available from: <http://www.gg.caltech.edu/~mwl/publications/papers/invariant.pdf>. 7

GÓMEZ, G.; LLIBRE, J.; MARTINEZ, R.; SIMÓ, C. Study on orbits near the triangular libration points in the perturbed restricted three body problem. **Barcelona, (ESOC Contract 6139/84/D/JS(SC))**, 1987. 2

GÓMEZ, G.; MARCOTE, M.; MASDEMONT, J. J.; MONDELO, J. M. Natural configurations and controlled motions suitable for formation flying. **Advances in the Astronautical Sciences**, v. 123, p. AAS 05–347, 2006. 16, 17, 72, 75

GÓMEZ, G.; MASDEMONT, J. Study of the transfer from the earth to a halo orbit around the equilibrium l1. **Celestial Mechanics and Dynamical Astronomy**, v. 56, p. 541–562, 1993. 4

GREENWOOD, D. T. **Principles of dynamics**. 2. ed. Englewood Cliffs, NJ: Prentice-Hall, 1988. 59

HENON, M. Vertical stability of periodic orbits in the restricted problem. **Astronomy and Astrophysics**, v. 28, p. 415–426, 1973. 2

HOWELL, K. C. Three-dimensional, periodic, halo orbits. **Celestial Mechanics**, v. 32, p. 53–71, 1984. 2

JET PROPULSION LABORATORY. **Terrestrial Planet Finder**. 2012. Available from: <http://exep.jpl.nasa.gov/TPF/tpf_sample.cfm>. Access in: 8 jan. 2013. xv, 1

KAPILA, V.; SPARKS, A. G.; BUFFINGTON, J. M.; YAN, Q. Spacecraft formation flying: dynamics and control. **Journal of Guidance, Control, and Dynamics**, v. 23, p. 561–564, 2000. 1

LAGRANGE, J. L. Essai sur le problème des trois corps. **Pirx de l'Académie Royale des Sciences de Paris**, IX, p. 229–324, 1772. 24

LANG, S. **Undergraduate analysis**. New York: Springer Verlag, 1997. 27, 34

LI, T. Y.; YORKE, J. A. Period three implies chaos. **American Mathematical Monthly**, v. 82, p. 985–992, 1975. 58, 61

MACAU, E. E. N.; GREBOGI, C. Driving trajectories in chaotic systems. **International Journal of Bifurcation and Chaos**, v. 11, p. 1423–1442, 2001. 12, 58

______. Control of chaos and its relevancy to spacecraft steering. **Philosophical Transactions of the Royal Society A**, v. 364, p. 2463–2481, 2006. 12, 58

MACAU, E. E. N.; WINTER, O. C.; VELHO, H. F. The aster mission: Exploring for the first time a triple system asteroid. In: INTERNATIONAL ASTRONAUTICAL CONGRESS, 62., 2011, Cape Town, South Africa. **Paper Number IAC-11,B4,2,7,x10263**. Paris: International Astronautical Federation, 2011. xxiii, 12, 58, 59, 60

MATHEMATICAL ASSOCIATION OF AMERICA. **Math Games**. 2004. Available from: <`http://www.maa.org/editorial/mathgames/mathgames_09_07_04.html`>. Access in: 9 jan. 2013. xv, 5

MCLAUGHLIN, W. I. Walter hohmann's road in space. **Journal of Space Mission Architecture**, v. 2, p. 1–14, 2000. 7

MELO, C. F. de; MACAU, E. E. N.; WINTER, O. C. Strategy for plane change of earth orbits using lunar gravity and trajectories derived of family g. **Celestial Mechanics & Dynamical Astronomy**, v. 103, p. 281–299, 2009. 55, 56, 90

MELO, C. F. de; MACAU, E. E. N.; WINTER, O. C.; NETO, E. V. Numerical study about natural escape and capture routes by the moon via lagrangian points l1 and l2. **Advances in Space Research**, v. 40, p. 83–95, 2007. xv, xvi, 12, 13, 54, 55, 56, 90, 98

MIELE, A. Theorem of image trajectories in the earth-moon space. **International Astronautical Congress, Stockholm**, v. 1, p. 225–232, August 1960. 71, 77

MORRIS, W. H.; SMALE, S. **Differential equations, dynamical systems, and linear algebra**. 1. ed. New York: Academic Press, 1974. 33

NASA. **NASA Space Place**. 2011. Available from: <http://spaceplace.nasa.gov/en/trees-from-space/>. Access in: 9 jan. 2013. xv, 3

_____. **LISA project Office**. 2012. Available from: <http://lisa.nasa.gov/>. Access in: 8 jan. 2013. xv, 2

O'NEILL, G. K. The colonization of space. **Physics Today**, v. 27, n. 9, p. 32–40, 1974. 3

OTT, E. **Chaos in dynamical systems**. New York: Cambridge University Press, 2002. 12, 65

PETERSIEM, M.; ROBERTSON, D. I.; DANZMANN, K.; WELLING, H.; BENDER, P. Lisa interferometer sensitivity to spacecraft motion. **Advances in Space Research**, v. 25, p. 1143–11147, 2000. 1

POINCARÉ, H. Sur le problème des trois corps et les équations de la dynamique. **Acta Mathematica**, v. 13, p. 1–270, 1890. 61, 63

PRADO, A. F. B. A. **Optimal transfer and swing-by orbits in the two and three-body problem**. PhD Dissertation — University of Texas - Austin, Austin, Texas, 1993. 9, 68

PRADO, A. F. B. A. Traveling between the lagrangian points and the earth. **Acta Astronautica**, v. 39, n. 7, p. 483–486, 1996. 11, 68

PRADO, A. F. B. A.; BROUCKE, R. A. Transfer orbits in the earth-moon system using a regularized model. **Journal of Guidance, Control and Dynamics**, v. 19, p. 929–933, 1996. 11

PRESS, W. H.; TEUKOLSKY, S. A.; VETTERLING, W. T.; FLANNERY, B. P. **Numerical recipes in C**: The art of scientific computing. 2. ed. Cambridge: Cambridge University Press, 1992. 77

SABOL, C.; BURNS, R.; MACLAUGLIN, C. A. Satellite formation flying design and evolution. **Journal of Spacecraft and Rockets**, v. 28, p. 270–278, 2001. 1

SALAZAR, F. J. T.; MELO, C. de; MACAU, E. E.; WINTER, O. C. Three-body problem, its lagrangian points and how to exploit them using an alternative transfer to l4 and l5. **Celestial Mechanics and Dynamical Astronomy**, v. 114, p. 201–213, 2012. 56

SCHAUB, H.; JUNKINS, J. L. **Analytical mechanics of space systems**. 1. ed. Blacksburg, Virgnia: AIAA Education Series, 2003. 33, 38, 39, 46, 60, 87

SCHROER, C. G.; OTT, E. Targeting in hamiltoniam systems that have mixed regular/chaotic phase spaces. **Chaos**, v. 7, n. 4, p. 512–519, 1997. 12, 58

SCHUTZ, B. F. Orbital mechanics of space colonies at l4 and l5 of the earth-moon system. In: AEROSPACE SCIENCES MEETING, 15., 1977, Los Angeles, California. **Paper No. 77-33**. Reston, Virginia: American Institute of Aeronautics and Astronautics, 1977. p. 12. 3

SHOLOMITSKY, G. B.; PRILUTSKY, O. F.; RODIN, V. G. Infra-red space interferometer. In: INTERNATIONAL ASTRONAUTICAL FEDERATION CONGRESS, 28., 1977, Praha, Czechoslovakia. **Anais**. Paris: International Astronautical Federation, 1977. 1

STOER, J.; BULIRSCH, R. **Introduction to numerical analysis**. 1. ed. New York: Springer Verlag, 1980. 77

SUKHANOV, A. A. The aster project: Flight to a near-earth asteroid. **Cosmic Research**, v. 48, n. 5, p. 443–450, 2010. 58

SZEBEHELY, V. **Theory of orbits**. New York: Academic Press, 1967. 19, 23, 30

TICKER, R. L.; AZZOLINI, J. D. 2000 survey of distributed spacecraft technologies and architectures for nasa's earth science enterprise in the 2010–2015 timeframe. **NASA Technical Memorandum, NASA/TM2000-209964**, 2000. 1

WERTZ, J. R.; LARSON, W. J. **Space mission and design**. Dordrecht, The Netherlands: Kluwer, 1991. 59

WIKIPEDIA. **Lagrangian point**. 2012. Available from: <`http://en.wikipedia.org/wiki/Lagrangian_point`>. Access in: 9 janeiro 2013. xv, 4

WOODCOCK, G. R. **Missions and operations modes for lunar basing**. Lunar and Planetary Institute, Houston: Mendell, W.W., 1985. 79

YOSHIDA, F.; NAKAMURA, T. Size distribution of faint l4 trojan asteroids. **The Astronomical Journal**, v. 130, n. 6, p. 2900–2911, 2005. 6

YOUNG, J. **EO-1 Extended Mission**. NASA Goddard Space Flight Center, 2012. 28 transparências. Available from: <`http://eo1.gsfc.nasa.gov/new/validationReport/index.html`>. Access in: 16 outubro 2012. 2

APPENDIX: ASTRODYNAMIC CONSTANTS

Table A.1 - Astrodynamic constants

Constant	Symbol	Value
Constant of Gravitation	G	6.673×10^{-20} km^3 kg^{-1} s^{-2}
Earth gravitational constant	μ_E	$398,658.37$ km^3 s^{-2}
Moon gravitational constant	μ_M	$4,902.87$ km^3 kg^{-1} s^{-2}
Earth mass	m_E	5.9742×10^{24} kg
Moon mass	m_M	7.3477×10^{22} kg
Mean Earth radius	r_E	$6,371$ km
Mean Moon radius	r_M	$1,737$ km
Mean Earth-Moon distance	d_{EM}	$384,405$ km
Moon's angular speed	ω_M	2.649×10^{-6} rad s^{-1}

PUBLICAÇÕES TÉCNICO-CIENTÍFICAS EDITADAS PELO INPE

Teses e Dissertações (TDI)

Teses e Dissertações apresentadas nos Cursos de Pós-Graduação do INPE.

Notas Técnico-Científicas (NTC)

Incluem resultados preliminares de pesquisa, descrição de equipamentos, descrição e ou documentação de programas de computador, descrição de sistemas e experimentos, apresentação de testes, dados, atlas, e documentação de projetos de engenharia.

Propostas e Relatórios de Projetos (PRP)

São propostas de projetos técnico-científicos e relatórios de acompanhamento de projetos, atividades e convênios.

Publicações Seriadas

São os seriados técnico-científicos: boletins, periódicos, anuários e anais de eventos (simpósios e congressos). Constam destas publicações o Internacional Standard Serial Number (ISSN), que é um código único e definitivo para identificação de títulos de seriados.

Pré-publicações (PRE)

Todos os artigos publicados em periódicos, anais e como capítulos de livros.

Manuais Técnicos (MAN)

São publicações de caráter técnico que incluem normas, procedimentos, instruções e orientações.

Relatórios de Pesquisa (RPQ)

Reportam resultados ou progressos de pesquisas tanto de natureza técnica quanto científica, cujo nível seja compatível com o de uma publicação em periódico nacional ou internacional.

Publicações Didáticas (PUD)

Incluem apostilas, notas de aula e manuais didáticos.

Programas de Computador (PDC)

São a seqüência de instruções ou códigos, expressos em uma linguagem de programação compilada ou interpretada, a ser executada por um computador para alcançar um determinado objetivo. Aceitam-se tanto programas fonte quanto os executáveis.